

17桁におよぶ地震エネルギーの研究

Investigating Earthquake Radiated Energies
over a Large Size Range

James Mori
Disaster Prevention Research Institute
Kyoto University

March 2002

Table of Contents

Forward	2
Estimates of Radiated Energy for Moderate Shallow Earthquakes in Japan <i>Hideki Kobayashi and James Mori</i>	3
Estimates of Radiated Seismic Energy for Shallow and Intermediate-depth Earthquakes beneath Northeastern Japan <i>AI Kim and James Mori</i>	38
Stress Drops and Radiated Energies of Aftershocks of the 1994 Northridge, California Earthquake <i>James Mori and Rachel Abercrombie</i>	73
List of Papers Presented at Conferences	107

Forward

This report summarizes work that was carried out under this project during 2000 to 2002. In this research I worked with my graduate students in investigating seismic radiated energy for a range of earthquakes in Japan and the US. Recently, such measurements of radiated energy have become important for studies of earthquake source scaling. In the 2 years, we were not able to fully examine the energies over the complete range of earthquake sizes that was planned, but we have obtained new results for a range of shallow and deep earthquakes in Japan. The results of these studies contribute new data for examining the relationship between energy and earthquake size.

I thank the Ministry of Education, Culture, Sports, Science and Technology for support of this research.

この論文は 2000 年から 2002 年にかけて実施された「17 桁の地震エネルギーの研究」プロジェクトのもとで行われた研究をまとめたものである。この中で、私は大学院生たちとともに、日本とアメリカのさまざまな地震についてその放射エネルギーを研究した。最近、こうした放射エネルギーの測定は地震スケーリングの研究のために重要性を増してきている。この 2 年間、当初の計画通りにあらゆる規模の地震のエネルギーを完全に調べることはできなかったものの、日本の浅発地震と深発地震に関する新しい結果を得ることができた。この研究結果はエネルギーと地震規模との関係を調べる上で新しいデータを加えることになろう。

この研究を後援してくれた文部科学省に謝意を表したい。

Estimates of Radiated Energy for Moderate Shallow Earthquakes in Japan

Hideki Kobayashi and James Mori

Disaster Prevention Research Institute, Kyoto University, Kyoto, JAPAN

Abstract

The main purpose of this study is to estimate radiated seismic energies of shallow earthquake and investigate the scaling as a function of earthquake size. We estimated seismic radiated energy for earthquakes with magnitude equal or greater than M4.0 (JMA magnitudes). We analyzed 115 earthquakes that occurred from March 1997 through October 1999, plus the 2000 Tottori Earthquake recorded on K-Net. The method of estimating E_s was modified from Kanamori et al. (1993) and uses the integrated squared velocity seismograms for distances within 200 km. I tested the effect of including SV and SH wave radiation pattern, but, the results were not significantly improved. The most important factor to improve the radiated energy estimate was including station corrections. For calculating of station corrections, sites were separated into hard (stiff) and soft sites by the average S-wave velocity in the upper 30 m ($V_s > 500\text{m/sec}$: Hard sites; $V_s < 500\text{m/sec}$: Soft sites). Station corrections were calculated relative to energy estimates using only the stiff sites. The results for the all of the earthquakes with depths less than 50 km appear to show a fairly constant ratio of radiated energy to seismic moment at about 9.10×10^{-5} . For the shallowest events with depths less than 15 km there appears to be a slight trend of increasing ratio of energy to moment as a function of seismic moment. These observations for the shallowest earthquakes are consistent with recent observations in southern California, where larger earthquakes proportionally radiate more energy. However, for the entire data set, and particularly for the deeper events, these results for earthquakes in Japan appear to be different from southern California, and show a fairly constant ratio of energy to seismic moment.

Introduction

Estimates of the energy radiated by seismic waves in an earthquake are relatively uncommon, compared to numerous estimate of moment and stress drop. This is rather surprising since energy is a fundamental parameter that is useful for understanding the physics of the earthquake source.

The first estimates of radiated seismic energy were done by Gutenberg and Richter (1956). In this

relation, radiated energy is function of magnitude. The amount of energy (E_S in ergs) is estimated from the surface magnitude, M_s , and body-wave magnitude, m_b .

$$\log E_S = 1.5M_s + 11.8. \quad (1.1)$$

$$\log E_S = 2.4m_b + 5.8. \quad (1.2)$$

More recently several studies have used modern broadband data to estimate the radiated energy. Kanamori et al. (1993) calculated radiated energy in southern California using TERRAScope data. Abercrombie (1995) discussed source parameters recorded at Cajon Pass borehole in southern California. She analyzed radiated energy for event with magnitudes from $M-1$ to $M5$. Mayeda and Walter (1996) estimated E_S by analyzing the frequency-dependent decay of amplitudes in the S coda. Jost et al. (1998) analyzed recordings from the KTB (German Continental Deep Drilling Program) 9km drilling and looked at $M-2$ to 0 events that were well recorded in the deep borehole. Mori et al. (2001) discussed source parameters and radiated energies of the 1994 Northridge Aftershocks. Singh and Ordaz (1994) looked at radiated energies for moderate to large earthquakes from the Mexican Subduction Zone.

There have also been several studies at radiated energy using teleseismic data. Kikuchi and Fukao (1988) estimated radiated energy from far-field long-period P waves for 35 large earthquakes. Choy and Boatwright (1995) estimated radiated energies for shallow earthquakes with magnitudes > 5.8 that occurred between 1986 and 1991. These two studies, concluded that the Gutenberg and Richter M_S overestimated the energy estimate. These teleseismic studies tend to give lower estimates of energy compared to the results from local data. For the teleseismic estimates, it is more difficult to accurately estimate the level of high frequency radiation. These studies are done using only P waves, so good estimates of the P wave attenuation and the energy partition between P and S are necessary.

One of the main purposes of almost all these studies is to investigate the scaling of radiated energy with earthquake size. Usually earthquake moment is used to characterize the earthquake size. For simple stress drop models, one expects that the ratio of E_S to M_0 will be a constant. Departures from this constant ratio may imply interesting consequences for the physics of earthquakes and for differences between small and large earthquakes. The studies by Kanamori et al. (1993), Abercrombie (1995), Mori et al. (2001) show results that suggest that the ratio of E_S to M_0 increases with earthquake moment, while the results of Singh and Ordaz (1994) and McGarr (1999) indicate that the ratio is constant.

In recent years there has been a large increase in high-quality data recorded in Japan. One example is the K-Net strong motion network operated by the National Research Institute for Earthquake Science and Disaster Prevention (NIED), Ministry of Education, Science, Sports and Culture (Fig.1).

K-NET STATION MAP



Fig. 1. The K-Net strong motion network operated by the National Research Institute for Earthquake Science and Disaster Prevention (NIED), Ministry of Education, Science, Sports and Culture. There are more than 1000 K-Net stations in Japan providing good coverage of broad band data for moderate to large earthquakes.

There are more than 1000 K-Net stations in Japan providing good coverage of broad band data for moderate to large earthquakes. We have used these data to estimate radiated energies for 115 earthquakes in Japan. The main purpose of this study is to investigate the scaling of radiated energy as a function of earthquake size for shallow earthquakes in Japan. This scaling is a currently a controversial issue and the data from Japan will be an important contribution to debate. Whether or not the ratio of E_s to M_0 increases with earthquake size has important implications for the mechanisms of earthquake ruptures and the differences between small and large earthquakes.

Method for Estimating Energy

For this study, we follow the method of Boatwright (1980) for estimating E_s , where E_s is proportional to the integral of the squared ground velocity. Including the radiation pattern and geometrical spreading to scale E_s , he studied the fractional energy flux of P-wave and S-waves, through a sphere around the source. E_s is calculated by the sum of the radial, transverse and vertical components of squared ground velocity integrated over the surface of the sphere.

In this study, we use the equations of Kanamori et al.(1993). These assume that all the radiated energy is contained in the S wave since the ratio of E_d/E_β is about 4%. We use S waves and consider a station at distance (Δ) from a point source and a sphere at a short distance r around the source. Let v be the velocity of ground motion observed at a station. The particle-motion velocity on the focal sphere, v_0 , is

$$v = v_0 C_f q(r) / q(r_0), \quad (2.1)$$

where C_f is the free-surface amplification factor, and r is the focal distance to the station (i.e., $r^2 = \Delta^2 + h^2$, Δ : epicentral distance, h : depth). The function $q(r)$ is an attenuation function for seismic waves. The attenuation function $q(r)$ is

$$q(r) = cr^{-n}\exp(-kr). \quad (2.2)$$

We use the constants $c = 0.49710$, $n = 1.0322$, $k = 0.0035\text{km}^{-1}$ which gives an attenuation relation similar to Fukushima and Tanaka (1990).

The S-wave energy radiating from the focal sphere can be expressed as

$$E_\beta = \rho_o \beta_o \int_{S_o} \int \Sigma v_o^2 dt dS \quad (2.3)$$

Fig. 2. Focal sphere model

(After Kanamori *et al.*, 1993)

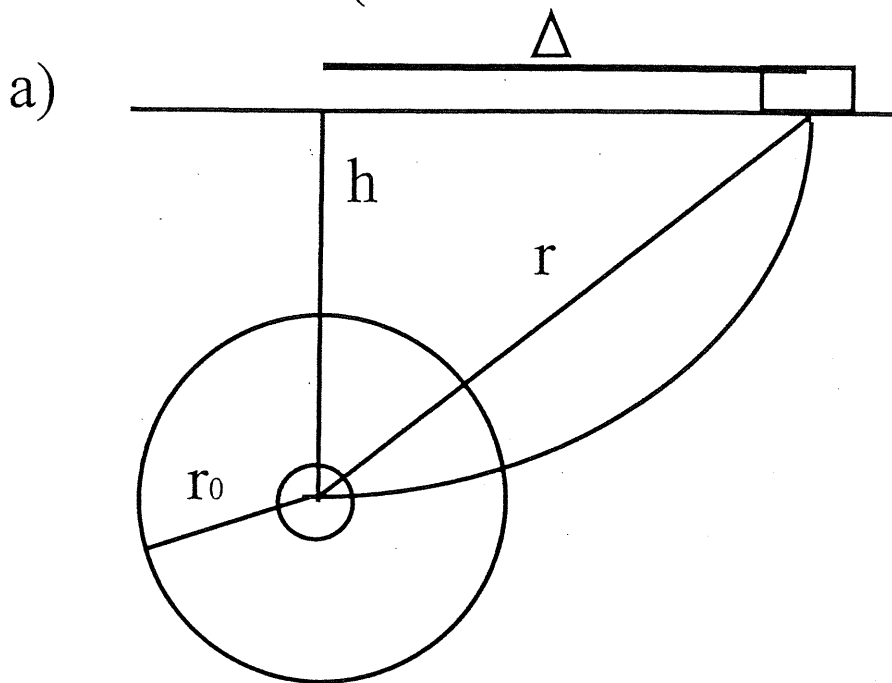


Fig. 2. (a) Ray geometry for a short distances. Only direct S-wave is included. (d : epicentral distance, km; Δ : hypocentral distance, km; h : depth, km; r_0 : radius of focal sphere, km).

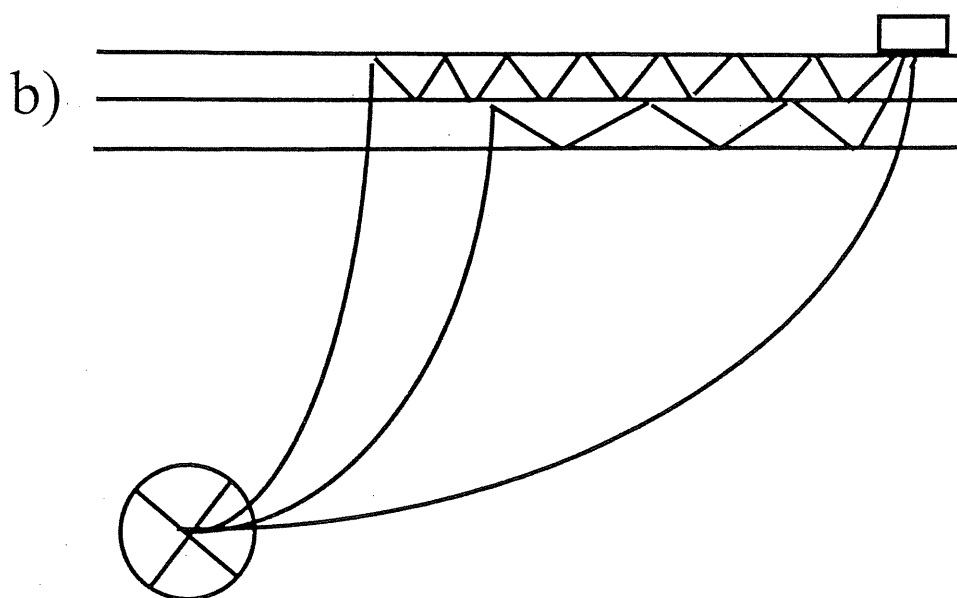


Fig. 2. (b) Ray geometry for large distances. Ray geometry is very complex which includes direct S-wave, scattered waves and reflected waves.

Where ρ_0 and β_0 are the density and S-wave velocity of the medium at the focal sphere, respectively.

The surface integral is taken over the focal sphere. The integration with time is to be taken over the S-wave train.

Substituting equation (2.1) into equation (2.3),

$$E_\beta = C_f^{-2} [q(r_o)/q(r)]^2 \rho_o \beta_o \int_{S_o} \int \Sigma v^2 dt \quad dS \quad (2.4)$$

If the radiation pattern is ignored, v^2 does not depend on azimuth, and equation (2.4) can be reduced to

$$E_\beta = 4\pi r_o^2 C_f^{-2} [r_o q(r_o)/q(r)]^2 \rho_o \beta_o \int \Sigma v^2 dt \quad (2.5)$$

For a double-couple source The average of the squared radiation pattern is

$$\overline{R^2} = \frac{1}{4\pi r_o^2} \int_{S_o} \Sigma R^2 dS = \frac{4}{15} \quad \text{and} \quad \frac{2}{-15} \quad (2.6)$$

for P and S waves, respectively. Using this in equation (2.4) gives

$$E_\beta = 2.36 \times 10^7 r_o^2 [r_o q(r_o)/r q(r)]^2 \int \Sigma v_s^2 dt \quad (2.7)$$

using the following numerical values: $\rho_o = 2.5 \text{ g/cm}^3$, $\beta_o = 3 \text{ km/sec}$, $r_o = 8 \text{ km}$. And we assume

$C_f = 2$ where r is in meters, $\int \Sigma v_s^2 dt$ is in $\{\text{m}^2/\text{sec}$, and E_β is in joules. With estimates of the

integral squared velocity $\int \Sigma v_s^2 dt$, we use equation (2.7) to make estimates of radiated seismic energy.

Data

In this study we used K-Net data recorded at the 905 sites shown in Fig. 1. The average stations spacing is about 25 km. The sensors are accelerometers and the systems have a good frequency response from about 0.01 to 30 Hz. The dynamic range of the recorders is 108 dB with a resolution of 15 mGal. These data are sampled at 100 Hz.

We analyzed 184 earthquakes that occurred from March 1997 through October 1999, plus the 2000 Tottori earthquake. During this time period we used all the events of M4.0 or greater (JMA magnitudes) that were well recorded on the K-Net stations. The distribution and source parameters

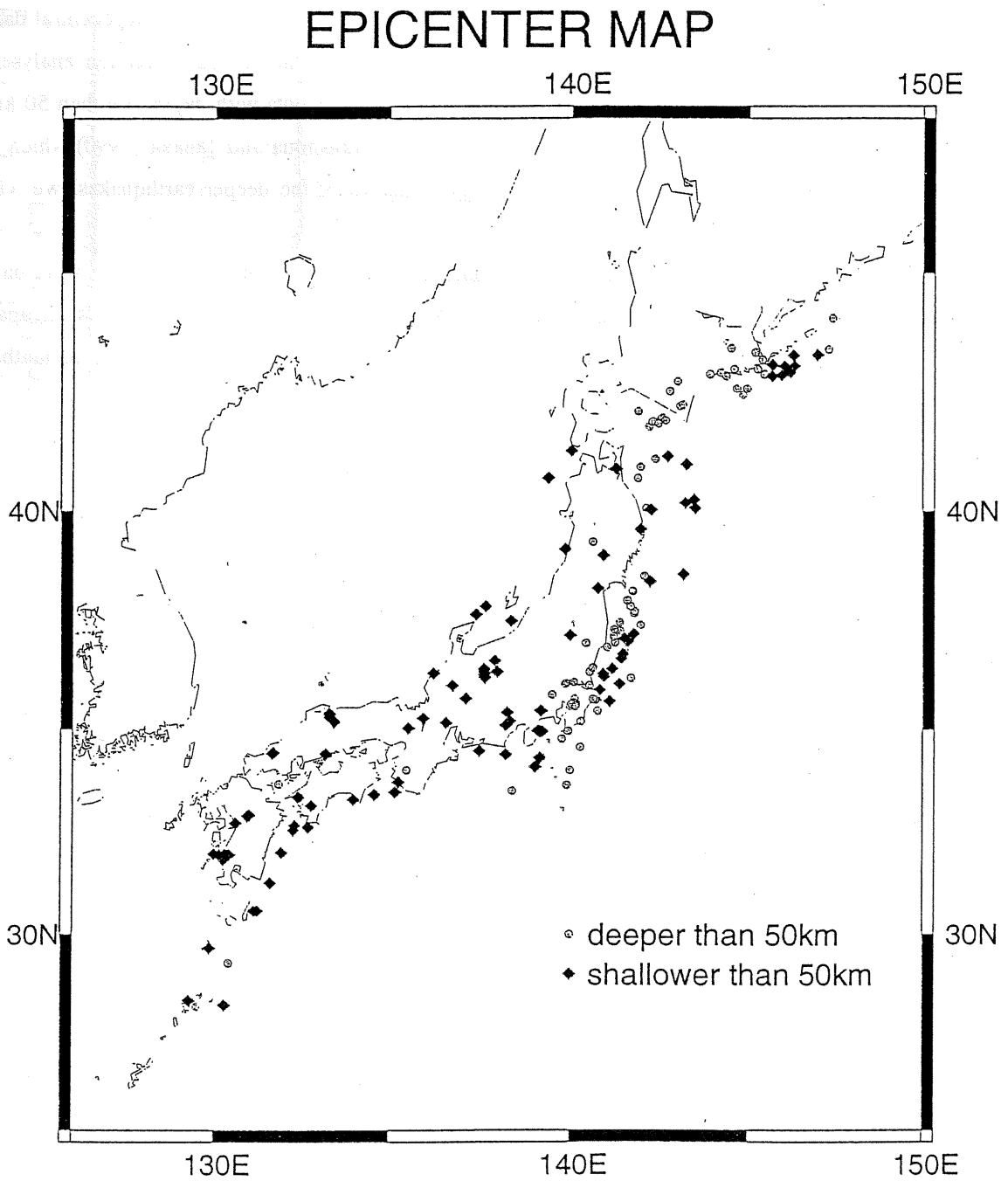


Fig. 3. Map of epicenters for earthquakes in this study. I analyzed 184 earthquakes ($M \geq 4.0$) that occurred from March 1997 through October 1999, plus the 2000 Tottori Earthquake. In this study, earthquakes shown by red circles occurred at depths shallower than 50 km. There are 115 of events with depths shallower than 50 km.

from these earthquakes are shown in Fig. 3 and Table 1. The moment and focal mechanism parameters were determined by the Freesia network which is operated by NIED. Hypocentral data were obtained from JMA. All of the earthquakes were used for the station correction analyses, however for the final determination of radiated energy, only the events with depth less than 50 km were used. In this study we used the attenuation relation of Fukushima and Tanaka (1990) which is appropriate for shallow events in Japan. For energy estimates of the deeper earthquakes, we will need a more appropriate attenuation relation.

For the estimates of radiated energy 2 to 161 stations were used, for most cases there were data from 34 or more stations. For the events that occurred under or close to the main islands of Japan there is good azimuth coverage of the stations, however for the offshore events, the azimuthal coverage was usually much more limited.

Data processing

Acceleration seismograms recorded by K-Net, which were picked up by the previous criterion, were down-loaded from the K-Net web site. The ASCII format data (i.e., raw data) were converted to SAC format binary data for the data processing in SAC. The flow of data processing in SAC is as follows.

- Read acceleration seismograms of two horizontal components (i.e., N-S and E-W components) and rotate to radial and transverse components.
- A 0.1 Hz high-pass filter was applied to the three components of acceleration seismograms. This filter is to eliminate the long-period noise. For these earthquakes there is little energy radiation at frequencies less than 0.1 Hz.
- Acceleration seismograms were integrated to velocity and squared.
- Velocity squared seismograms were integrated.
- The integrated value at 50 sec is used for the estimate of energy in equation (2-7).

For the analyses, only stations within 200 km from the earthquake were used.

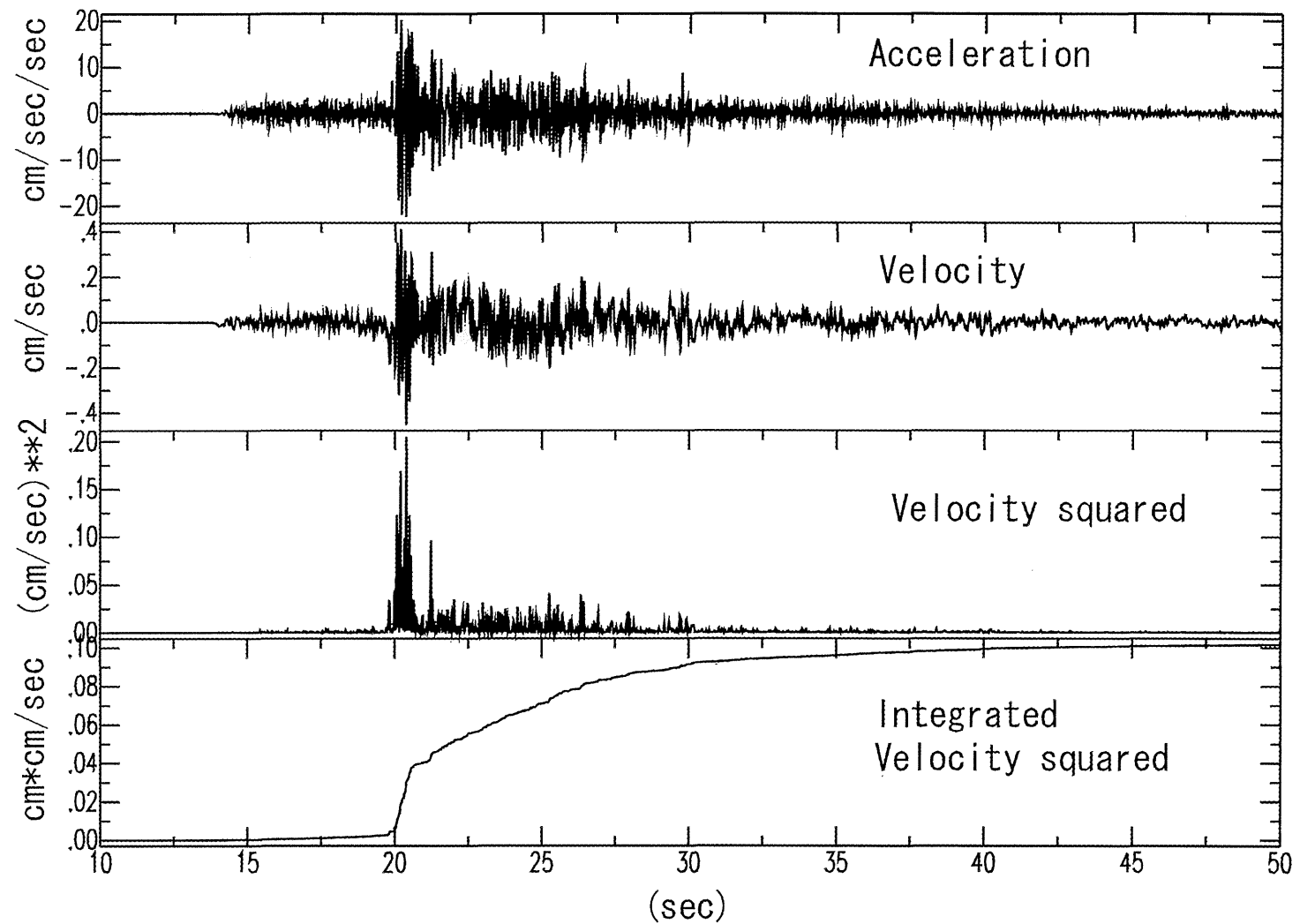


Fig. 4. Example of data processing used in this study. The final result used for estimating the radiated energy is the amplitude of the integrated squared velocity waveform at 50 sec.

Attenuation relation

One difference from the equations of Kanamori et al. (1993) is that we used a different attenuation relation. The amplitude decay of seismic waves in Japan is likely different from that in southern California.

The attenuation relation we used was modified from Fukushima and Tanaka (1990). They estimated attenuation relation using peak horizontal acceleration seismograms of 28 earthquakes in Japan. The result of the attenuation relation in Japan is

$$\log A = 0.41M - \log(R + 0.032 * 10^{0.41M}) - 0.0034 R + 1.30. \quad (5.1)$$

Parameters of equation (2.2) we used were modified from equation (5.1).

After calculated radiated energies, we examined the reliability of equation (5.1) for estimating E_s in Japan. To do so, we looked at the distance dependence of the energy estimates in this study. Fig. 5 shows the individual energy estimates plotted as a function of distance and normalized by the average energy. From this plot one sees that there is no strong systematic trend with distance, suggesting that the attenuation relation is appropriate for this study.

Radiation Pattern

In the equations of Kanamori et al. (1993) an average radiation pattern was included. we also tried to calculate the energies by explicitly putting in the effect of the radiation pattern. The following formulas are given by Aki and Richards (1980). For the double couple source in a homogeneous medium, the SV and SH radiation patterns are F^{SV} and F^{SH} , respectively,

$$\begin{aligned} F^{SV} = & \sin \lambda \cos 2\delta \cos 2i_\xi \sin(\phi - \phi_s) - \cos \lambda \cos \delta \cos 2i_\xi \cos(\phi - \phi_s) \\ & + \frac{1}{2} \cos \lambda \sin \delta \sin 2i_\xi \sin 2(\varphi - \phi_s) \\ & - \frac{1}{2} \sin \lambda \sin 2\delta \sin 2i_\xi (1 + \sin^2(\varphi - \phi_s)) \end{aligned}$$

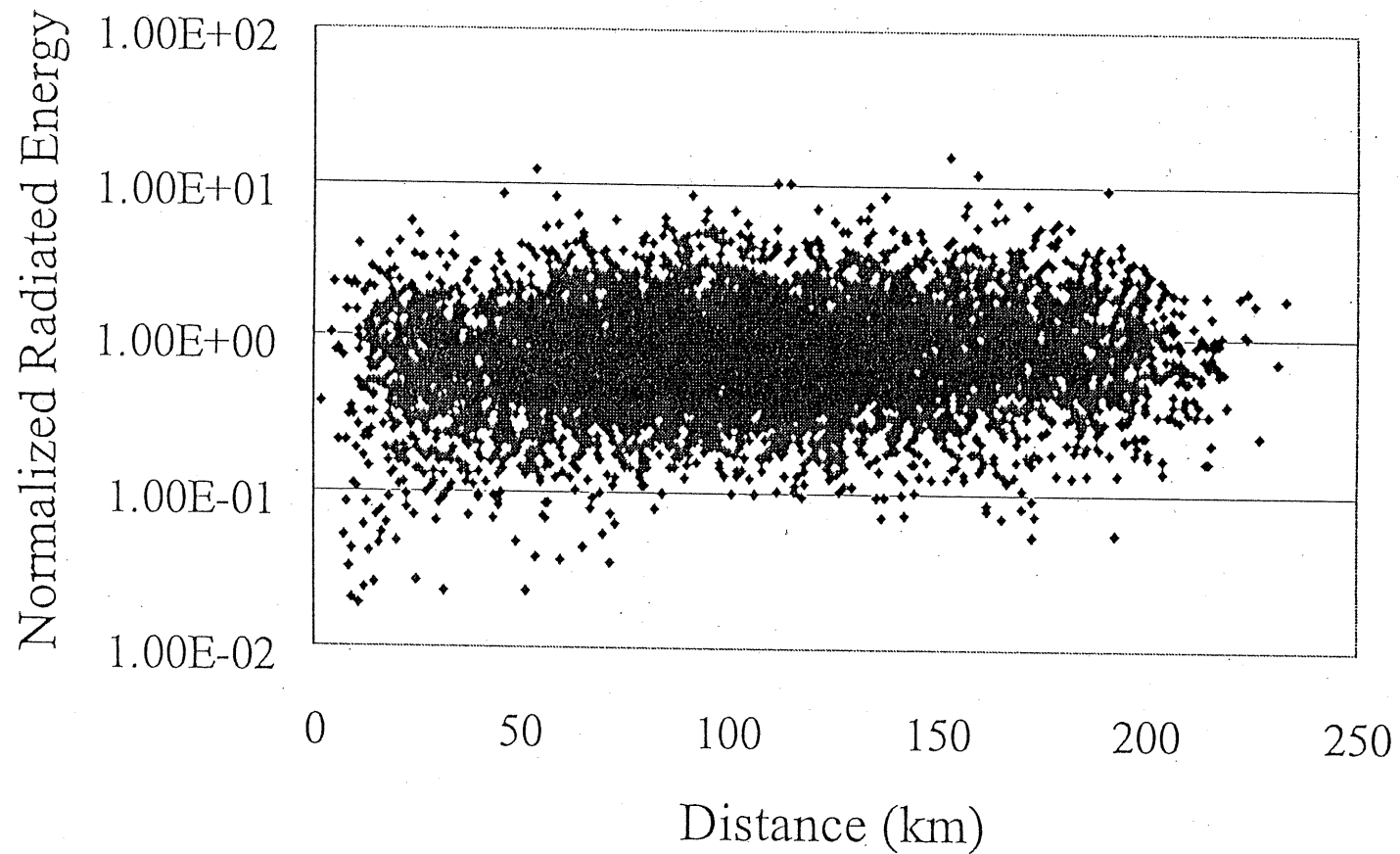


Fig. 5. Individual energy estimates plotted as a function of distance and normalized by the average energy. From this plot one sees that there is no strong systematic trend with distance, suggesting that the attenuation relation is appropriate for this region.

$$\begin{aligned}
F^{SH} &= \cos \lambda \cos \delta \cos i_{\xi} \sin(\phi - \phi_s) + \cos \lambda \sin \delta \sin i_{\xi} \cos 2(\phi - \phi_s) \\
&+ \frac{1}{2} \sin \lambda \cos 2\delta \cos i_{\xi} \cos(\phi - \phi_s) \\
&- \frac{1}{2} \sin \lambda \sin 2\delta \sin i_{\xi} \sin 2(\phi - \phi_s)
\end{aligned}$$

Using the focal mechanisms provided by the FREESIA network, we calculated the SH and SV radiation patterns and included them in the energy calculations. In the results section, we show the difference this makes for the energy estimate.

Station Corrections

In this study, the value of station corrections is an important factor for improving the quality of the results. There can be large amplitude effects at the stations which can effect our results. Site effects can cause amplitude differences of factor of 3 or greater. Since our energy estimate is based on the amplitude squared, this means it will change the radiated energy estimate by a factor of 9.

We used the following procedure to determine the station corrections.

1. Sites were separated into hard (stiff) and soft sites by the average S-wave velocity in the upper 30m. Hard sites were defined as having average S-wave velocities of 500 m/sec or greater. Soft sites had average S-wave velocities of less than 500 m/sec. These average velocities were determined from the site information available for K-Net sites from their web page. The sites I categorized as stiff, roughly correspond to Class A and B sites of the classification of strong-motion stations used by Boore et al. (1994).
2. The radiated energy for each earthquake was calculated using only the stiff sites.

$$\overline{e_{i,hard}} = \frac{1}{N_{si}} \sum_{j=1}^{N_{sj}} e_{i,hard_j} \quad (7.1)$$

3. A radiated energy estimate was calculated for each station and compared to the value determined from using only the stiff sites. The ratio of the individual station estimate to the stiff site estimate, averaged over all earthquakes, is the station correction.

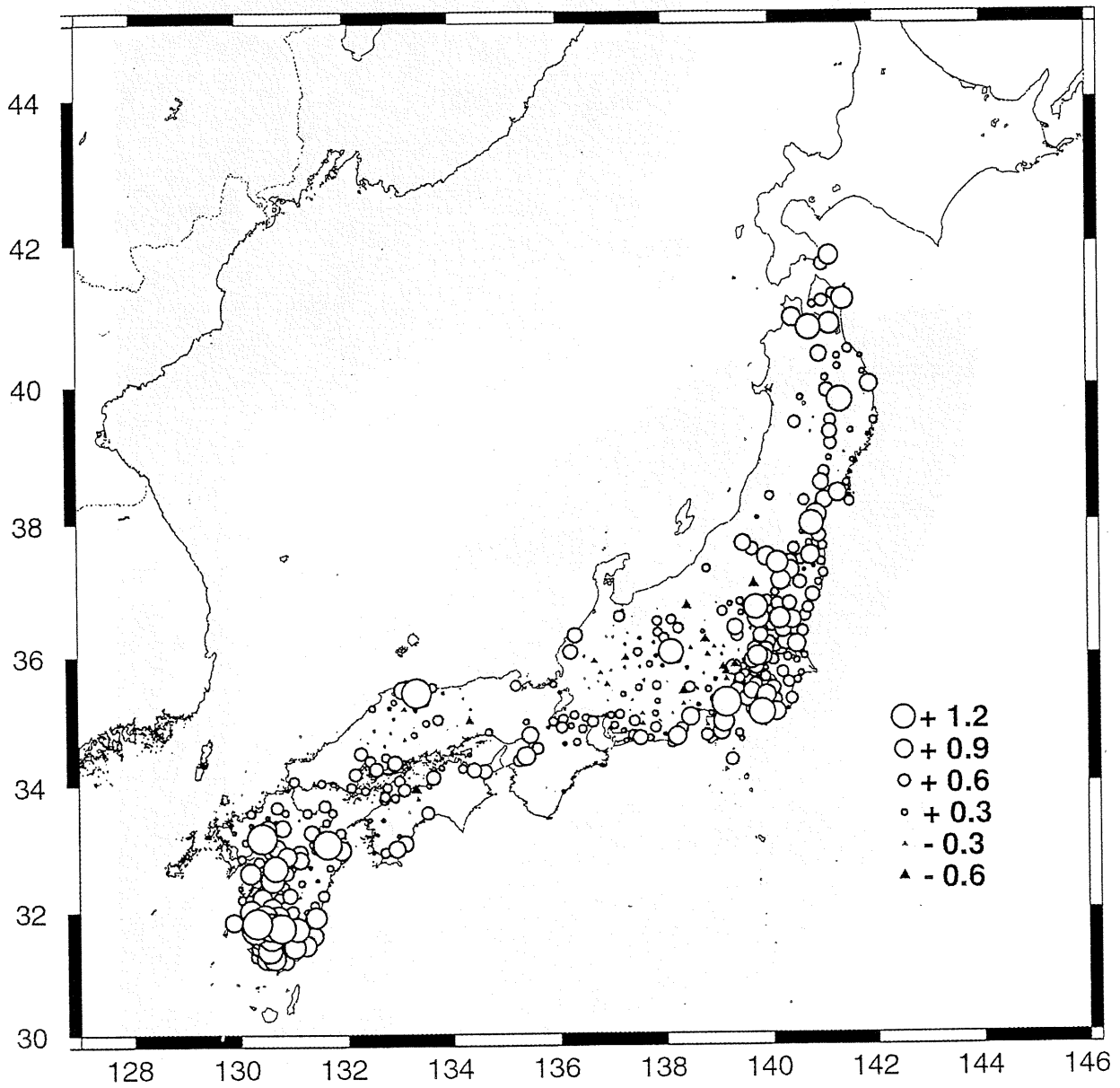


Fig. 6. Distribution of station corrections for the K-Net sites determined in this study.



Fig. 7. 1 : 1,000,000 geological map of Japan (Geological Survey of Japan, 1995) used for discussing the results of the stations corrections (shown in Fig. 6.). Large station corrections in the Kanto plain may be due to amplifications from the large sediment thickness in that region. The area of southern Kyushu also shows large positive station corrections. This may be due to amplifications on the thick volcanic sediments. The areas of central Japan generally show small amplitude that might be associated with hard sites in the central mountainous region.

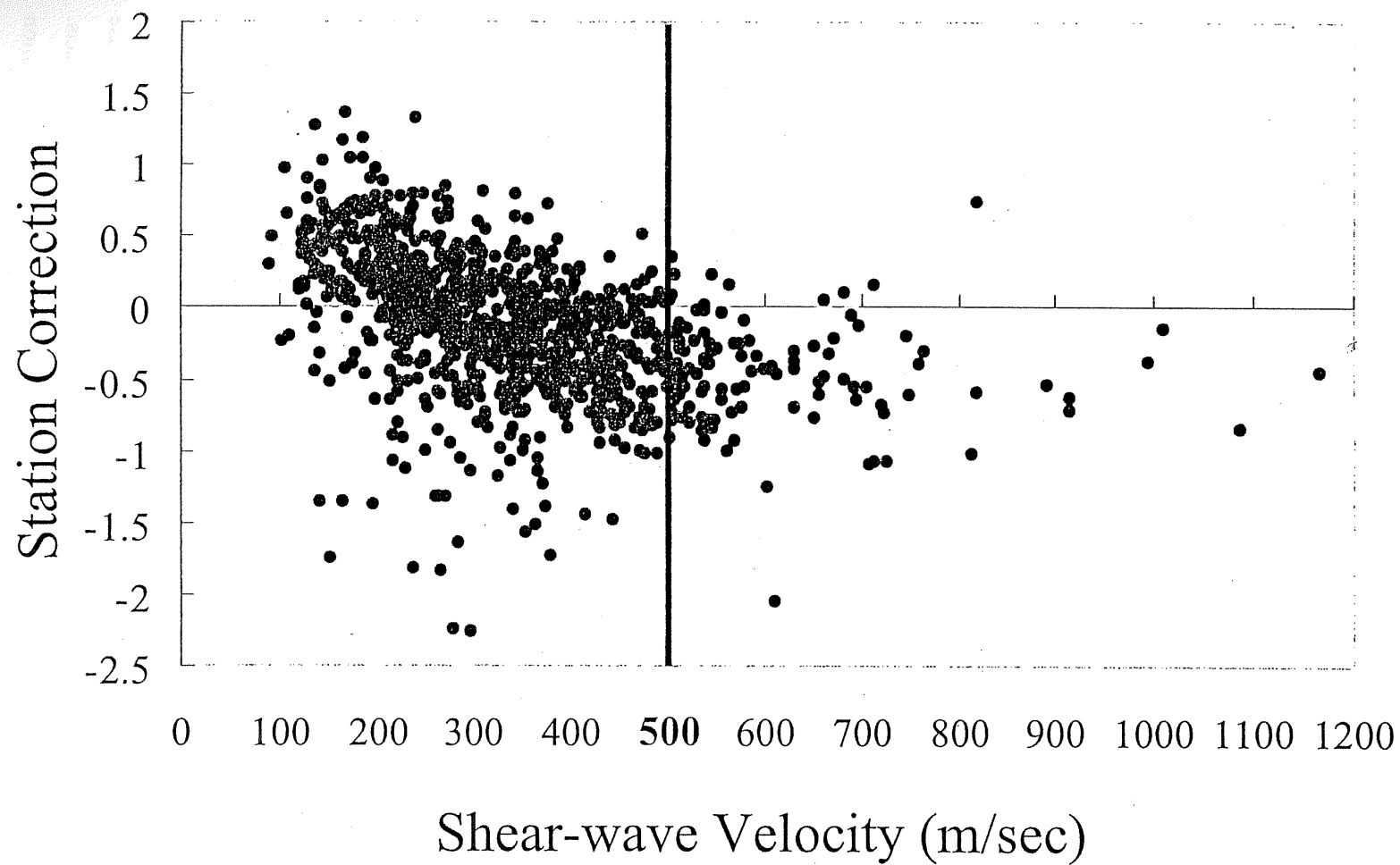


Fig. 8. The relationship between the calculated station correction and the 30 m average shear wave velocity from the K-Net site information. There is a clear trend of higher station corrections (sites that have larger observed amplitudes) with lower shear-wave velocity.

$$\overline{stacor}_j = \frac{1}{N_{ej}} \sum_{i=1}^{N_{sj}} \frac{e_{ij}}{e_i \text{hard}} \quad (7.2)$$

These stations corrections were used in the final estimates of the radiated energies.

The distribution of the stations corrections for the K-Net sites is shown in Fig. 6. There are some correlations with the regional geology as seen in the geological map (Fig. 7) from the Geological Survey of Japan (1995). Large station corrections in the Kanto plain may be due to amplifications from the large sediment thickness in that region. The area of southern Kyushu also shows large positive stations corrections. This may be due to amplifications on the thick volcanic sediments. The areas of central Japan generally show small amplitude that might be associated with hard sites in the central mountainous region.

Fig. 8 shows the relationship between the calculated station correction and the 30 meter average shear wave velocity from the K-Net site information. One can see a clear trend of higher station corrections (sites that have larger observed amplitudes) with lower shear-wave velocity.

Results

Station corrections

Figures 9 and 10 shows the results of the radiated energy estimates as a function of seismic moment, before and after applying the stations corrections. The error bars show the range of one standard deviation. The diagonal lines show trends of constant ratio of radiated energy to seismic moment. The top plot of both figures shows the results for all the events and the bottom plot shows the values for only the shallow earthquakes with depths less than 50 km. From these figures we can see two clear results.

1. The energy estimate values have smaller uncertainties when including the station corrections.
2. The values of radiated energy are lower when including the stations corrections.

The smaller uncertainties from the results including the stations corrections are expected because this procedure corrects for the large variations in amplitude that are caused by the local site effects. Fig. 11 shows explicitly the smaller standard deviation for the energy estimates after the station correction procedure is carried out. The overall lower values of the energy are also expected because

Fig. 9.

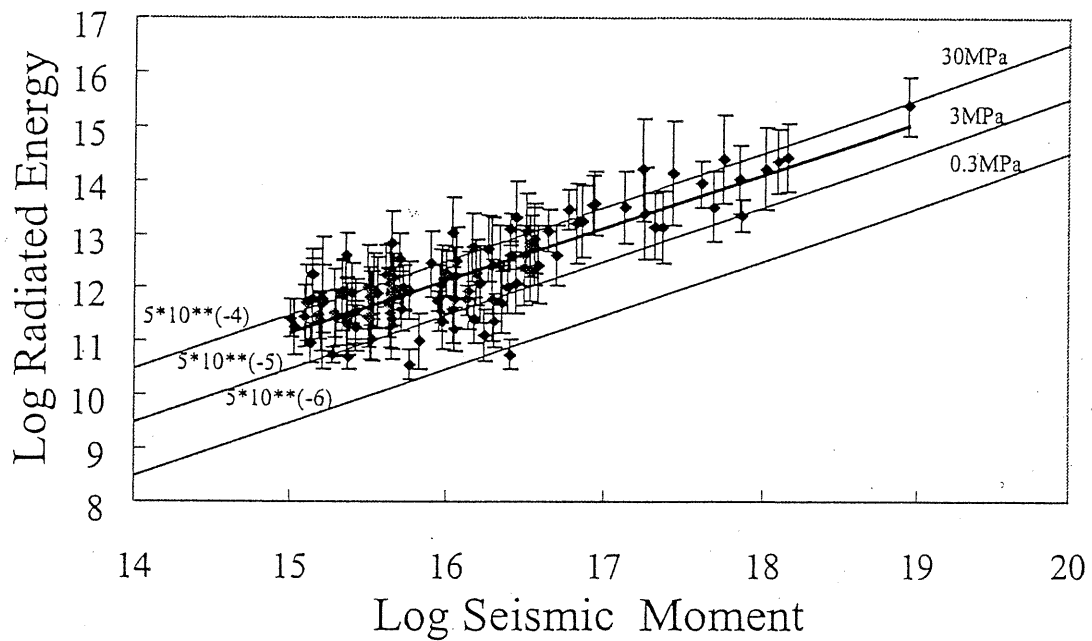


Fig. 9. Results of radiated energy estimates as a function of moment, before applying the station corrections.

Fig. 10.

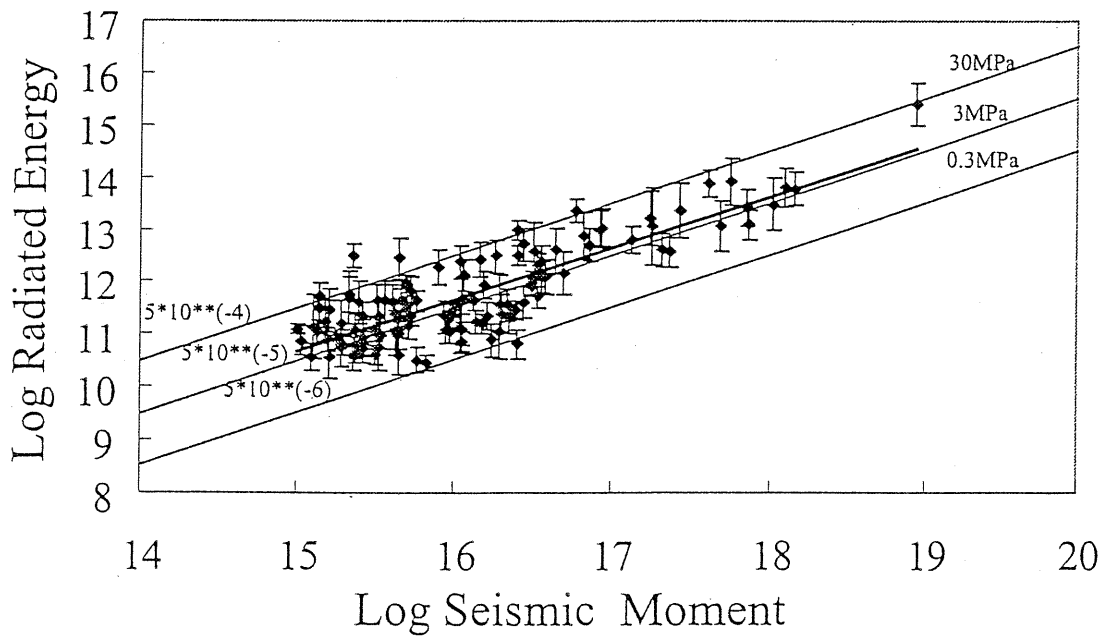


Fig. 10. Results of radiated energy estimates as a function of moment, after applying the station corrections. Compared with Fig. 9., the values of radiated energy are lower when station corrections are included.

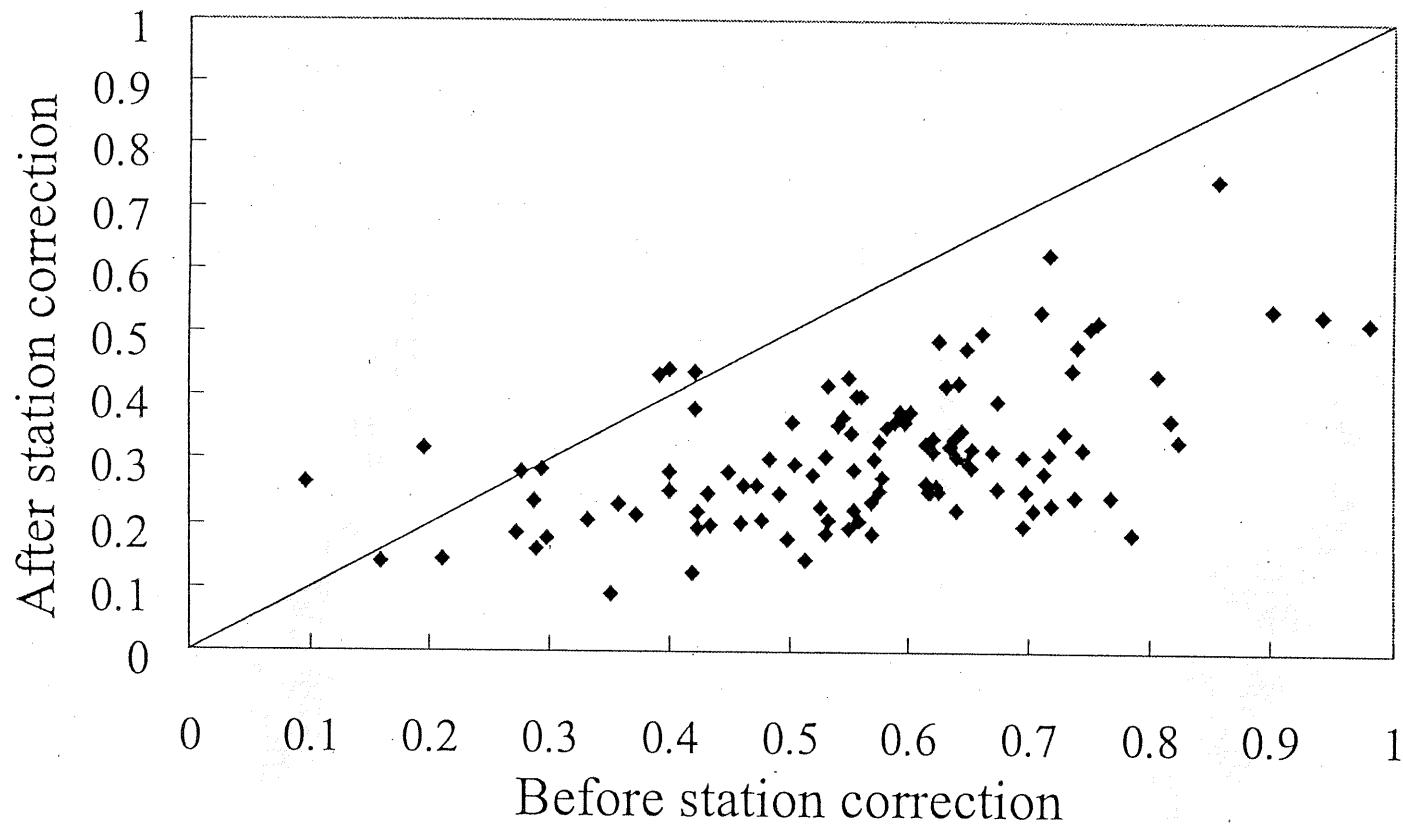


Fig. 11. Plot of the standard deviations at the energy estimates before and after the station correction procedure was carried out.

using all the data without station corrections includes many soft sites that amplify ground motions and would cause over estimates of the radiated energy.

Fig. 10 shows the best results for estimates of radiated energies of shallow earthquakes in Japan. In the next section the effects of the radiation pattern are described, but that procedure did not improve the results.

Radiation Pattern

Fig. 12 shows the results before and after the radiation pattern was included in the estimate of radiated energy. For the case that includes the radiation pattern, the same procedure described above was used to calculate the station corrections. The results of the energy estimates calculated with stations corrections and a radiation pattern correction are shown in Fig. 12(b). Comparison of Figures 12(a) and 12(b) show that there was not an improvement in the uncertainty with the inclusion of the radiation pattern. The error is in fact slightly larger. The reason for this result is probably because the energy from other arrivals beside the direct S wave is included in the observations. Since the entire S-wave coda is used, the energy from scattered waves is also measured. For this reason, it seems more appropriate to use an average radiation pattern for all stations, such as done by Kanamori et al. (1993) rather than to try and correct for the radiation pattern of the direct S wave. Under this assumption, however, it is important to have a reasonable good azimuthal station coverage for the earthquake. One might try to make the energy estimates using only the direct S wave, but this might underestimate the energy since it does not capture the scattered waves.

Interpretation and Discussion

Scaling of Radiated Energy

The main goal of this study was to determine the radiated energy of earthquakes and investigate the relation as a function of earthquake size. Fig. 10 shows the best estimates of radiated energy for shallow earthquakes plotted as a function of seismic moment. In this plot the trend of data appears to show a constant ratio of E_S to M_0 which is equal to 9.10×10^{-5} . However, there is a large scatter to the data and the ratio, if it has constant value that has a large range from 5×10^{-6} to 5×10^{-4} . Fitting least-squares line to all of these data gives

Table 1.

Year	Month	Day	Hour	Min.	Latitude (deg)	Longitude (deg)	Depth (km)	Number of Stations	M_0 (Nm)	E_s (J)	RMS	Strike (deg)	Dip (deg)	Slip (deg)	M_{JMA}	M_w	Region
1997	3	3	23	27	34.963	139.165	2	11	1.97E+15	6.068E+10	0.188	338	77	-40	4.3	4.2	E OFF IZU PENINSULA
1997	3	4	0	30	34.960	139.173	0	59	3.60E+16	1.229E+12	0.281	264	80	-147	4.7	5.0	E OFF IZU PENINSULA
1997	3	4	12	51	34.951	139.171	3	76	2.09E+17	3.915E+12	0.313	160	87	19	5.7	5.5	E OFF IZU PENINSULA
1997	3	5	22	43	34.958	139.156	3	21	1.39E+16	1.697E+11	0.230	346	80	-31	4.3	4.7	E OFF IZU PENINSULA
1997	3	6	15	50	40.725	139.383	36	48	2.77E+16	5.117E+12	0.307	197	81	101	4.5	4.9	W OFF AOMORI PREF
1997	3	7	10	20	34.963	139.240	5	17	1.95E+16	3.723E+11	0.539	172	82	35	4.2	4.8	E OFF IZU PENINSULA
1997	3	7	16	33	34.965	139.150	1	23	2.49E+16	2.823E+11	0.176	346	88	-32	4.5	4.9	E OFF IZU PENINSULA
1997	3	7	21	35	34.960	139.168	3	15	8.97E+15	1.199E+11	0.254	346	78	-16	4.3	4.6	E OFF IZU PENINSULA
1997	3	26	17	31	31.968	130.360	12	106	1.40E+18	6.039E+13	0.321	103	88	-9	6.5	6.1	NW KAGOSHIMA PREF
1997	3	26	18	5	31.968	130.398	13	41	9.53E+15	2.292E+11	0.224	9	88	174	4.4	4.6	NW KAGOSHIMA PREF
1997	3	26	21	15	31.991	130.015	18	23	2.64E+15	6.895E+10	0.229	120	87	-18	4.1	4.2	W OFF AMAKUSA ISLAND
1997	3	26	22	24	31.973	130.437	9	33	1.12E+16	1.251E+11	0.292	253	75	-42	4.3	4.7	NW KAGOSHIMA PREF
1997	4	3	4	33	31.966	130.323	15	63	1.33E+17	6.338E+12	0.256	99	89	-8	5.6	5.4	NW KAGOSHIMA PREF
1997	4	4	2	33	31.956	130.393	14	44	1.14E+16	4.627E+11	0.428	198	76	-156	4.6	4.7	NW KAGOSHIMA PREF
1997	4	5	13	24	31.966	130.405	12	53	3.11E+16	8.015E+11	0.184	195	86	-167	4.8	5.0	NW KAGOSHIMA PREF
1997	4	8	2	5	33.375	132.401	47	31	1.54E+15	8.253E+10	0.224	176	72	-86	4.1	4.1	SW EHIME PREF
1997	4	23	10	24	32.746	130.636	13	29	3.34E+15	5.769E+10	0.443	234	80	-167	4.1	4.3	NW KUMAMOTO PREF
1997	5	2	4	35	30.580	131.155	38	7	1.94E+16	1.158E+11	0.518	210	89	107	4.1	4.8	NEAR TANEGASHIMA ISLAND
1997	5	13	14	38	31.943	130.313	9	96	1.22E+18	6.369E+13	0.377	191	88	-175	6.3	6.0	NW KAGOSHIMA PREF
1997	5	14	8	32	31.931	130.345	9	39	2.21E+16	3.566E+11	0.318	91	87	-37	4.7	4.9	NW KAGOSHIMA PREF
1997	5	24	2	50	34.496	137.501	23	70	1.80E+17	1.154E+13	0.744	310	80	-15	5.9	5.5	ENSYUNADA
1997	6	25	18	50	34.438	131.668	8	123	5.66E+17	8.147E+13	0.435	319	89	14	6.3	5.8	YAMAGUCHI PREF
1997	7	26	18	36	31.966	130.438	9	23	3.12E+15	4.075E+10	0.196	92	78	-24	4.2	4.3	NW KAGOSHIMA PREF
1997	9	4	5	12	35.251	133.378	12	58	3.63E+15	4.323E+11	0.394	321	86	21	4.4	4.3	WESTERN TOTTORI PREF
1997	10	11	14	44	34.420	138.234	35.7	50	3.38E+16	2.082E+12	0.234	112	52	81	4.9	5.0	ENSYUNADA
1997	10	20	23	12	36.314	140.917	42.6	48	4.53E+15	4.493E+11	0.201	4	82	62	4.1	4.4	E OFF IBARAKI PREF

Table 1. (Continued)

1997	10	21	19	55	35.110	138.232	33.1	52	2.47E+15	4.005E+11	0.399	199	81	-73	4.3	4.2	CENTRAL SHIZUOKA PREF
1997	11	12	8	58	32.919	130.967	11.9	21	4.27E+15	9.377E+10	0.261	123	70	-44	4.1	4.4	NE KUMAMOTO PREF
1997	12	19	22	7	36.321	136.223	12.5	42	3.22E+15	4.259E+11	0.306	202	58	71	4.4	4.3	NW OFF HOKURIKU DISTRICT
1997	12	23	15	18	36.245	140.936	42.2	23	3.32E+15	2.221E+11	0.283	340	77	56	4.2	4.3	E OFF IBARAKI PREF
1998	1	8	23	46	37.869	137.672	29.6	5	1.01E+15	1.261E+11	0.092	182	59	74	4.2	4.0	SADOGASHIMA IS REG
1998	1	10	14	2	31.840	130.285	6.5	24	4.41E+15	3.941E+10	0.357	194	85	173	4.1	4.4	NW KAGOSHIMA PREF
1998	2	10	1	20	35.739	137.125	10.9	57	1.39E+15	3.229E+11	0.480	333	90	12	4.2	4.1	SE GIFU PREF
1998	2	26	10	44	35.671	141.102	24.9	5	2.62E+15	2.151E+11	0.265	203	85	7	4.3	4.2	NEAR CHOSHI CITY
1998	3	27	15	30	31.973	130.456	9.0	27	4.20E+15	1.082E+11	0.422	259	84	-9	4.1	4.4	NW KAGOSHIMA PREF
1998	4	4	1	40	37.540	138.376	27.0	40	7.90E+15	1.909E+12	0.336	34	57	94	4.5	4.6	OFF S NIIGATA PREF
1998	4	5	10	54	35.408	138.279	12.8	55	4.50E+15	4.402E+11	0.368	249	89	-154	4.4	4.4	AKAISHI MOUNTAINS REG
1998	4	22	10	41	34.956	139.194	8.1	16	2.31E+15	6.165E+10	0.253	324	84	-35	4.0	4.1	E OFF IZU PENINSULA
1998	4	22	17	50	34.950	139.190	5.7	14	2.59E+15	5.307E+10	0.260	328	79	-31	4.1	4.1	E OFF IZU PENINSULA
1998	4	22	20	32	35.165	136.570	10.5	161	6.74E+16	7.657E+12	0.443	24	67	108	5.4	5.2	SHIGA GIFU BORDER REGION
1998	4	25	18	34	34.977	139.184	6.2	12	2.61E+15	8.415E+10	0.361	353	73	-29	4.1	4.1	E OFF IZU PENINSULA
1998	4	26	7	37	34.960	139.175	4.7	37	3.42E+16	5.137E+11	0.206	346	85	-33	4.7	5.0	E OFF IZU PENINSULA
1998	4	26	15	3	34.977	139.110	0.9	19	9.04E+15	1.825E+11	0.198	84	77	-163	4.4	4.6	E OFF IZU PENINSULA
1998	4	26	22	3	34.947	139.188	5.2	10	1.90E+15	5.444E+10	0.365	343	74	-31	4.0	4.1	E OFF IZU PENINSULA
1998	4	27	6	9	34.953	139.193	7.2	24	1.62E+16	2.237E+11	0.245	349	69	-31	4.5	4.7	E OFF IZU PENINSULA
1998	5	3	11	9	34.956	139.178	2.8	79	2.35E+17	3.646E+12	0.288	165	85	8	5.7	5.5	E OFF IZU PENINSULA
1998	5	5	17	25	34.949	139.195	5.6	7	2.25E+15	4.161E+10	0.308	355	80	-17	4.0	4.1	E OFF IZU PENINSULA
1998	5	15	3	56	40.257	143.467	0.0	9	7.19E+17	1.221E+13	0.286	37	79	103	5.8	5.9	FAR E OFF SANRIKU
1998	6	25	6	30	34.336	139.164	9.7	5	1.09E+16	1.298E+11	0.488	271	62	135	4.2	4.7	NEAR NIJIMA ISLAND
1998	7	1	2	22	36.615	137.931	8.6	45	3.79E+16	1.202E+12	0.342	354	71	46	4.7	5.0	NORTHERN NAGANO PREF
1998	8	3	20	9	37.200	140.000	10.9	62	4.99E+16	1.436E+12	0.400	167	67	81	4.9	5.1	WESTERN FUKUSHIMA PREF
1998	8	12	9	40	36.230	137.653	5.2	9	6.60E+15	2.817E+10	0.146	86	84	149	4.1	4.5	HIDA MOUNTAINS REGION
1998	8	12	15	13	36.231	137.627	4.0	27	2.25E+16	1.993E+11	0.271	84	84	146	4.7	4.9	HIDA MOUNTAINS REGION

Table 1. (Continued)

1998	8	14	14	6	36.288	137.628	6.7	5	2.35E+15	3.980E+10	0.146	82	84	169	4.0	4.2	HIDA MOUNTAINS REGION
1998	8	14	19	36	36.297	137.627	6.6	21	1.52E+16	1.576E+11	0.199	87	83	162	4.4	4.8	HIDA MOUNTAINS REGION
1998	8	16	23	5	37.237	141.778	44.7	53	8.38E+16	9.970E+12	0.343	22	63	87	5.2	5.2	E OFF FUKUSHIMA PREF
1998	8	17	10	15	36.349	137.620	6.4	24	2.00E+16	2.388E+11	0.360	185	89	-17	4.3	4.8	HIDA MOUNTAINS REGION
1998	8	22	3	55	36.234	137.652	4.3	16	9.42E+15	1.155E+11	0.248	75	89	171	4.3	4.6	HIDA MOUNTAINS REGION
1998	9	5	10	8	36.401	137.632	5.9	17	1.76E+16	7.660E+10	0.301	354	82	15	4.4	4.8	HIDA MOUNTAINS REGION
1998	9	5	12	2	36.421	137.628	3.8	13	2.53E+16	6.438E+10	0.280	355	84	14	4.3	4.9	HIDA MOUNTAINS REGION
1998	9	7	5	49	43.131	145.668	48.9	17	5.28E+15	6.781E+11	0.253	237	87	-155	4.2	4.4	OFF NEMURO PENINSULA
1998	9	8	8	40	35.933	140.827	36.5	17	8.63E+15	2.143E+11	0.319	13	70	90	4.2	4.6	NEAR CHOSHI CITY
1998	9	15	8	16	32.577	132.265	36.8	7	4.30E+15	1.833E+11	0.184	346	48	-87	4.2	4.4	HYUGANADA REGION
1998	9	15	16	24	38.278	140.766	13.2	72	3.19E+16	3.885E+12	0.534	37	54	99	5.0	5.0	SOUTHERN MIYAGI PREF
1998	9	18	17	16	36.327	137.654	5.1	17	1.12E+16	7.420E+10	0.193	266	83	-166	4.4	4.7	HIDA MOUNTAINS REGION
1998	9	20	6	53	36.435	137.630	5.4	11	5.75E+15	3.235E+10	0.235	180	83	-13	4.0	4.5	HIDA MOUNTAINS REGION
1998	9	24	17	3	33.448	134.569	44.6	17	1.91E+15	1.621E+11	0.437	308	75	162	4.2	4.2	SE OFF SHIKOKU
1998	9	28	2	50	32.026	131.929	37.0	16	5.75E+15	4.234E+11	0.207	320	64	141	4.4	4.5	HYUGANADA REGION
1998	10	4	2	1	36.769	141.467	46.2	43	4.93E+15	8.429E+11	0.207	204	79	-105	4.5	4.4	E OFF IBARAKI PREF
1998	10	14	5	41	40.077	143.497	0.0	6	1.76E+17	1.613E+13	0.529	23	56	91	5.4	5.5	FAR E OFF SANRIKU
1998	11	7	20	13	28.324	129.309	20.9	3	1.01E+16	3.008E+11	0.124	243	76	138	4.5	4.6	NEAR AMAMI-OSHIMA ISLAND
1998	11	10	11	21	33.170	132.776	46.2	18	2.15E+15	4.910E+11	0.501	187	52	-75	4.2	4.2	SW KOCHI PREF
1998	11	16	8	8	37.682	137.403	14.9	36	1.45E+16	2.746E+12	0.336	74	79	143	4.7	4.7	OFF NOTO PENINSULA
1998	11	21	1	40	36.429	141.174	46.1	18	5.24E+15	2.272E+11	0.205	6	86	76	4.3	4.4	E OFF IBARAKI PREF
1998	11	25	2	36	37.066	141.610	42.2	43	1.08E+16	2.401E+12	0.317	25	76	90	4.6	4.7	E OFF FUKUSHIMA PREF
1998	12	5	1	38	33.501	135.148	44.7	20	1.50E+15	1.761E+11	0.381	324	7	-97	4.0	4.1	S PART OF KII CHANNEL
1998	12	16	9	18	31.278	131.604	32.3	44	1.02E+18	3.025E+13	0.507	12	73	-65	5.5	6.1	SE OFF OSUMI PEN
1998	12	17	21	49	36.076	141.376	41.1	27	4.37E+16	3.921E+12	0.434	8	85	67	4.9	5.1	FAR E OFF IBARAKI PREF
1999	1	11	9	10	36.042	136.749	8.9	26	4.36E+15	1.033E+11	0.305	160	52	86	4.3	4.4	FUKUI GIFU BORDER REGION
1999	1	16	15	41	36.666	141.427	40.7	27	4.11E+15	3.954E+11	0.351	9	89	89	4.4	4.4	E OFF IBARAKI PREF

Table 1. (Continued)

1999	1	22	7	2	38.596	143.170	0.0	16	4.77E+17	1.119E+13	0.476	23	68	96	5.5	5.8	FAR E OFF MIYAGI PREF
1999	1	28	10	25	36.367	137.994	8.8	50	1.17E+16	1.395E+12	0.296	357	67	48	4.7	4.7	CENTRAL NAGANO PREF
1999	2	1	1	52	37.118	141.547	48.5	64	8.58E+16	1.085E+13	0.360	22	64	83	5.1	5.3	E OFF FUKUSHIMA PREF
1999	2	1	2	1	37.124	141.518	48.2	35	1.38E+15	5.283E+11	0.262	23	78	79	4.4	4.1	E OFF FUKUSHIMA PREF
1999	2	1	4	29	43.343	146.958	46.4	14	4.06E+17	7.551E+13	0.247	240	84	-131	5.3	5.7	E OFF HOKKAIDO
1999	2	26	14	18	39.154	139.854	19.4	69	7.19E+16	4.908E+12	0.312	181	66	79	5.1	5.2	W OFF AKITA PREF
1999	3	2	23	20	32.651	132.684	38.5	8	3.15E+15	1.276E+11	0.242	51	66	-45	4.1	4.3	FAR E OFF MIYAZAKI PREF
1999	3	7	10	3	42.924	145.927	43.2	19	2.54E+16	9.644E+12	0.177	59	64	-136	5.0	4.9	OFF NEMURO PENINSULA
1999	3	9	12	53	32.944	131.014	9.6	62	2.79E+16	4.125E+11	0.300	133	72	-44	4.5	4.9	NE KUMAMOTO PREF
1999	3	11	20	6	39.603	141.958	32.7	52	4.41E+15	2.809E+12	0.377	269	62	71	4.6	4.4	NORTHERN IWATE PREF
1999	3	16	16	43	35.271	135.935	12.1	134	1.83E+16	3.054E+12	0.328	17	66	101	4.9	4.8	NW SHIGA PREF
1999	3	19	2	55	41.030	143.242	44.0	19	7.14E+17	2.585E+13	0.347	22	62	77	5.7	5.9	E OFF AOMORI PREF
1999	3	25	0	7	33.745	135.247	49.8	28	5.01E+15	3.377E+11	0.279	184	82	27	4.3	4.4	S PART OF KII CHANNEL
1999	3	28	1	37	34.119	139.046	18.4	28	3.61E+16	2.393E+12	0.324	42	83	-8	5.0	5.0	NEAR NIJIMA ISLAND
1999	4	3	3	45	31.958	130.312	8.0	28	3.41E+15	9.241E+10	0.253	14	82	166	4.1	4.3	NW KAGOSHIMA PREF
1999	4	19	3	44	39.020	140.919	12.1	25	5.06E+15	1.414E+11	0.253	197	48	92	4.3	4.4	SOUTHERN IWATE PREF
1999	5	7	21	48	35.213	138.344	19.9	69	1.56E+16	8.606E+11	0.265	16	76	33	4.7	4.8	CENTRAL SHIZUOKA PREF
1999	5	22	9	48	35.450	139.194	23.5	43	1.61E+15	2.843E+11	0.417	50	69	73	4.1	4.1	KANAGAWA PREF
1999	5	23	17	19	43.335	146.259	47.4	22	2.26E+15	3.099E+12	0.219	191	83	115	4.4	4.2	OFF NEMURO PENINSULA
1999	6	15	16	47	42.982	146.169	42.8	23	5.90E+16	2.238E+13	0.213	67	74	141	5.1	5.1	OFF NEMURO PENINSULA
1999	6	22	1	52	43.106	146.000	47.6	18	2.57E+16	3.171E+12	0.187	32	62	83	4.8	4.9	OFF NEMURO PENINSULA
1999	7	16	2	59	34.425	133.196	20.5	79	2.12E+15	5.611E+11	0.330	201	83	161	4.4	4.2	EASTERN HIROSHIMA PREF
1999	7	16	11	19	29.649	129.897	34.7	2	1.32E+16	4.271E+11	0.163	271	52	-104	4.5	4.7	NEAR TOKARA ISLANDS
1999	7	31	7	55	31.965	130.169	10.7	19	1.22E+15	3.670E+10	0.254	30	86	166	4.0	4.0	W OFF AMAKUSA ISLAND
1999	9	13	5	32	40.932	141.267	14.7	17	1.26E+15	1.375E+11	0.626	194	66	83	4.0	4.0	SHIMOKITA PENINSULA REG
1999	10	3	6	9	40.182	143.223	0.0	22	2.71E+17	2.199E+13	0.516	28	70	95	5.6	5.6	FAR E OFF SANRIKU
2000	10	6	13	30	35.275	133.349	11.2	119	8.62E+18	2.514E+15	0.417	150	85	-9	7.3	6.6	WESTERN TOTTORI PREF

Table 1. (Continued)

2000	10	6	22	57	35.181	133.426	8.4	3	1.35E+15	1.118E+11	0.230	241	81	-17	3.9	4.1	WESTERN TOTTORI PREF
2000	10	6	23	13	35.293	133.291	7.9	6	1.84E+15	7.487E+10	0.141	253	71	177	4.1	4.1	WESTERN TOTTORI PREF
2000	10	7	6	38	35.358	133.297	10.9	10	3.21E+15	1.070E+11	0.331	249	52	-175	4.3	4.3	WESTERN TOTTORI PREF
2000	10	7	8	17	35.382	133.288	8.4	4	1.58E+15	3.675E+10	0.397	260	86	-170	4.0	4.1	WESTERN TOTTORI PREF
2000	10	7	12	3	35.372	133.316	8.9	15	2.31E+15	1.270E+11	0.284	67	77	-172	4.3	4.2	WESTERN TOTTORI PREF
2000	10	8	20	51	35.368	133.313	8.9	46	3.11E+16	9.637E+11	0.224	256	81	-177	5.0	5.0	WESTERN TOTTORI PREF
2000	10	8	20	59	35.364	133.306	9.3	12	1.06E+15	7.375E+10	0.278	78	73	159	3.8	4.0	WESTERN TOTTORI PREF
2000	10	10	21	58	35.371	133.306	11.4	36	4.15E+15	2.439E+11	0.251	253	76	-180	4.4	4.4	WESTERN TOTTORI PREF

Table 1. Source parameters for events analyzed in this study. Moments and focal mechanisms are from the FREESIA Network operated by NIED. Locations are from JMA.

Fig. 12(a).

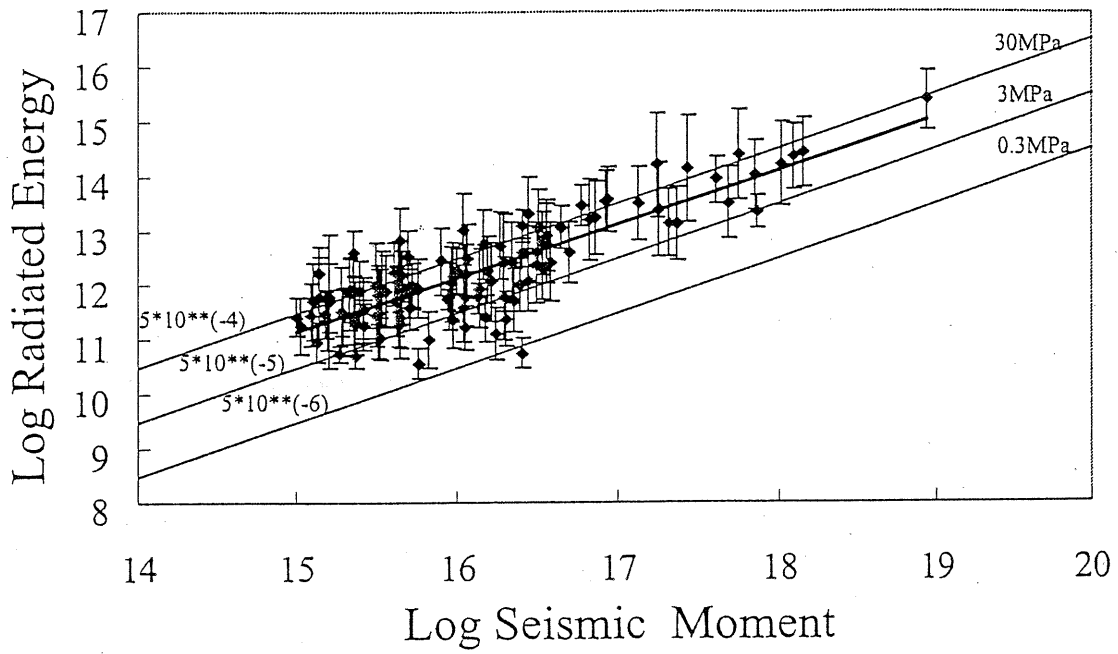


Fig. 12(b).

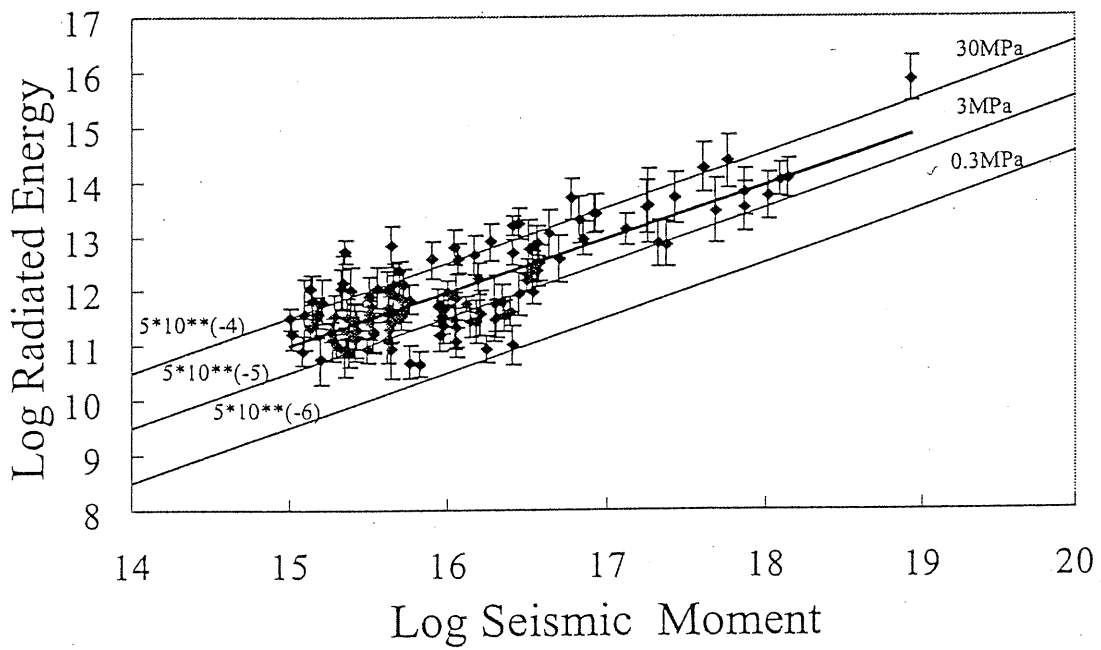


Fig. 12. Results before and after the radiation pattern was included in the estimate of the radiated energy.

$$\log E_s = 0.9766 \log M_0 - 3.9628 \quad (R^2 = 0.7093). \quad (9.1)$$

The slope (0.9766) is very close to one and R^2 is the correlation factor.

Looking more carefully at the data, it is possible that there is more than one trend that might be caused by mixing of data sets. For example, separating the events by tectonic setting or location might separate the results into different trends. To test this idea, we tried dividing the data using smaller subsets using the following classification.

1. Plotted ratio of radiated energy to moment as a function of rake angle to separate events by focal mechanism (Fig. 13).
2. Separated the data by source depths into two groups, shallower than 15km and 15 km to 50 km (Fig. 14). Also, plotted the ratio of radiated energy to moment as a function of source depth (Fig. 15).
3. Separated the data into two groups by regional location, events directly under the main islands of Japan and offshore events (Fig. 16).

From the Figures 13 –16, there did not seem to be much difference in the results when events were separated by focal mechanism or by regional location. However, there seems to be some significance to separating the events by depth. If we look at Fig 14, which shows the results for the shallow (< 15 km) events, there is a slight positive slope to the values. Although, the slope is small, these results appear to be fairly consistent for the results from southern California (Kanamori et al., 1993) which are also for shallow earthquakes (Fig. 17). In particular the larger events (such as the 2000 Western Tottori-ken earthquake M_w 6.6) appear to be radiating proportionately more seismic energy than the smaller events. The interesting observation is for the deeper earthquake and the data set as a whole do not seem to follow this trend that is observed in southern California. The trends are still not clearly determined, especially with the lack of larger earthquakes. However, taking into account these uncertainties, these results suggest that for the deeper earthquakes in Japan, the larger events do not radiate proportionally more seismic energy. The deeper earthquakes and the data set as a whole is more consistent with simple models that have a constant ratio of E_s to M_0 that does not depend on earthquake size.

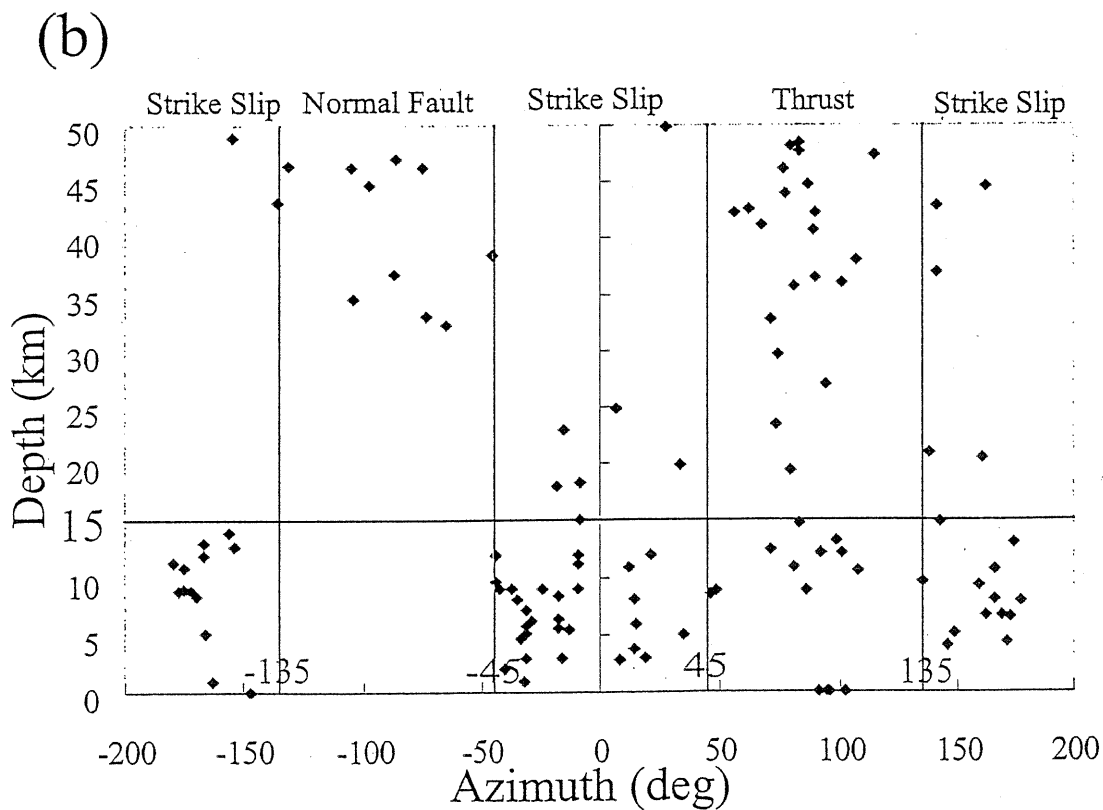
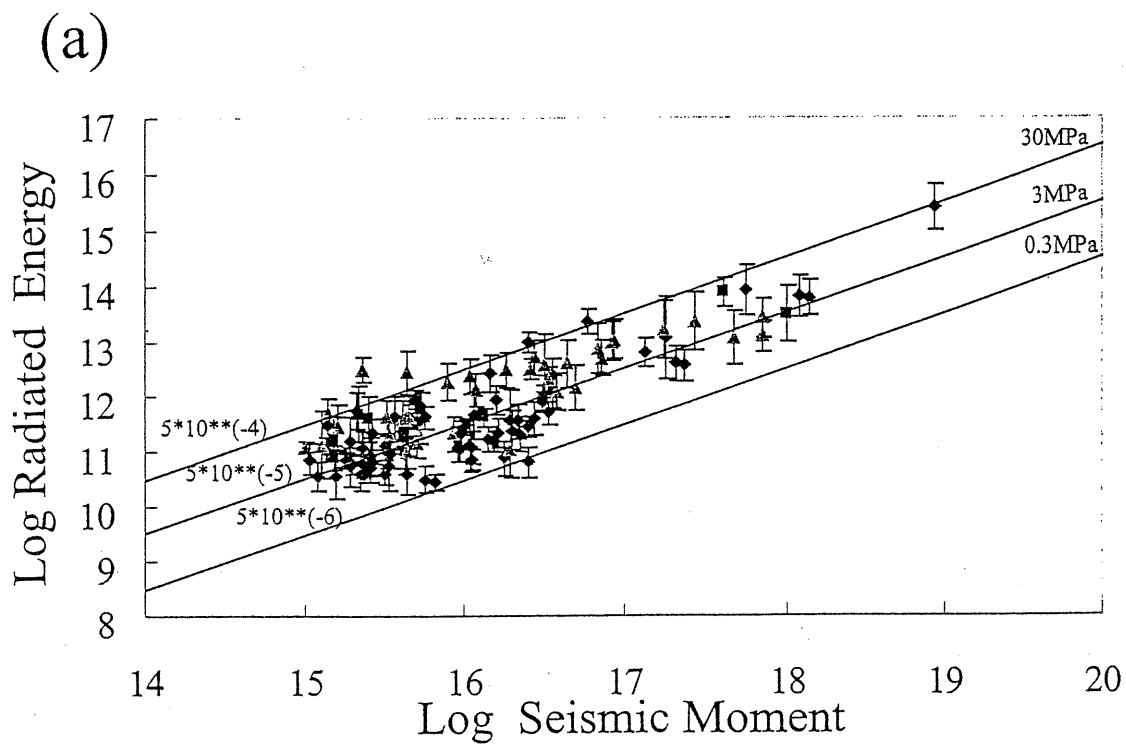


Fig. 13. (a) Radiated energies separated by focal mechanism. (b) Depth of events plotted as a function of rake angle showing that the strike-slip events tend to be shallow.

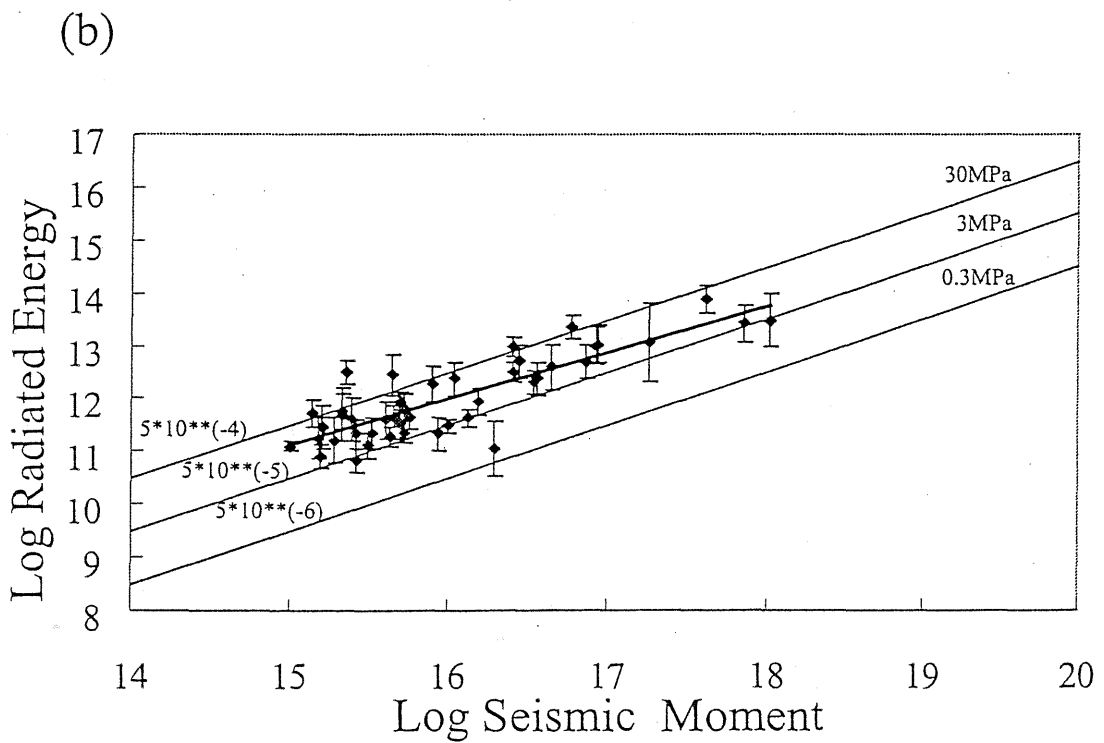
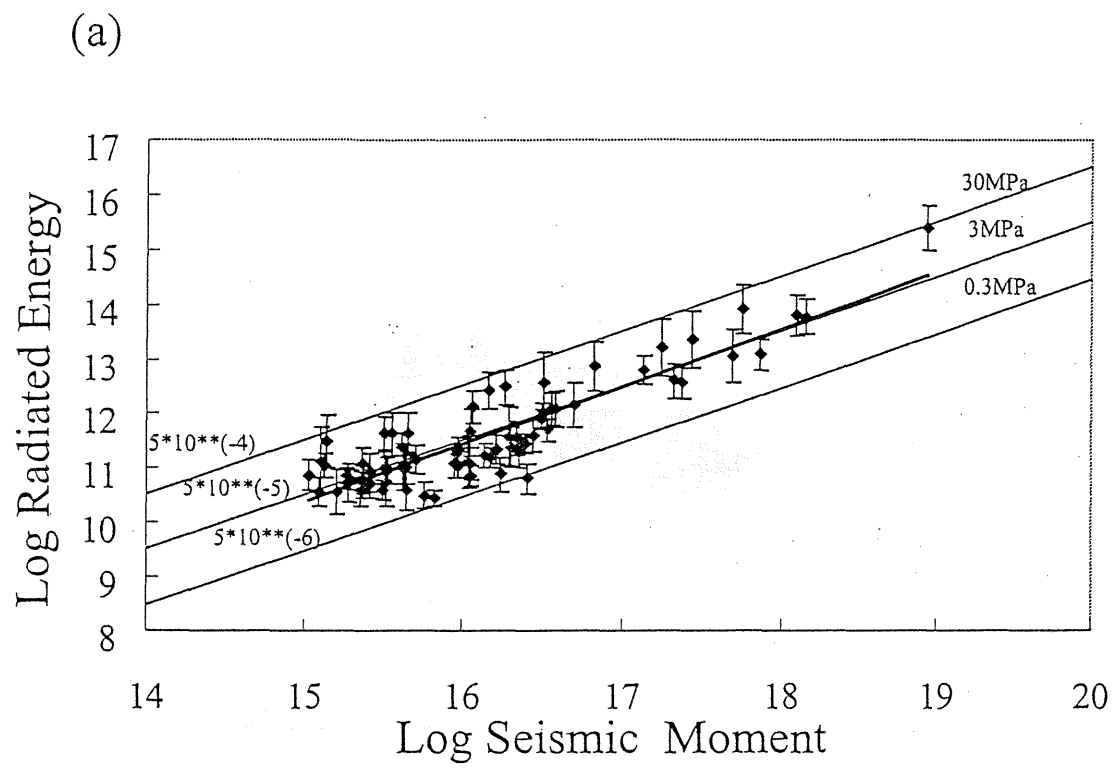


Fig. 14. Data separated into two groups by source depths. (a) Events shallower than 15 km. (b) Events with depths 15 to 50 km.

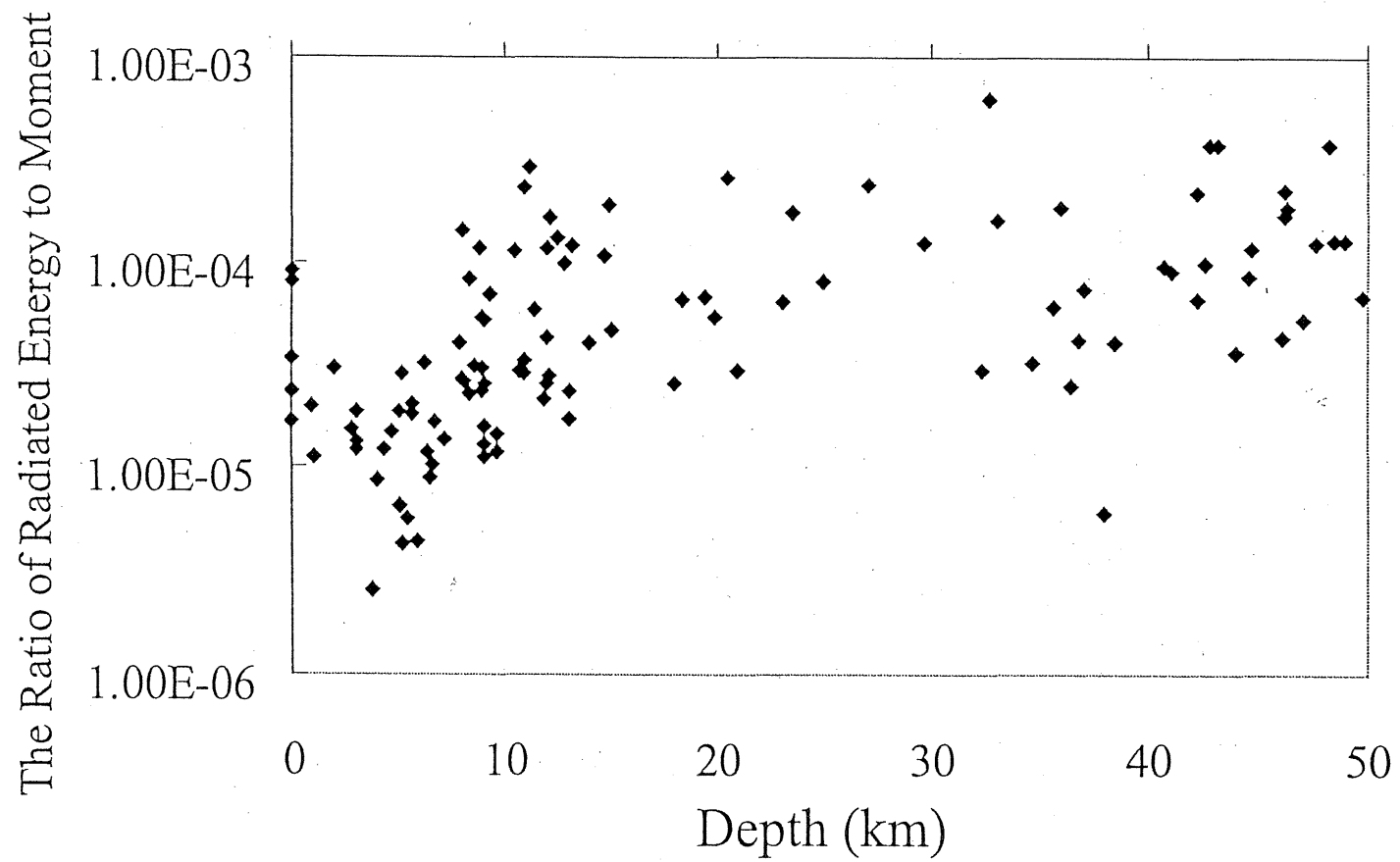


Fig. 15. Ratio of radiated energy to moment plotted as a function of source depth.

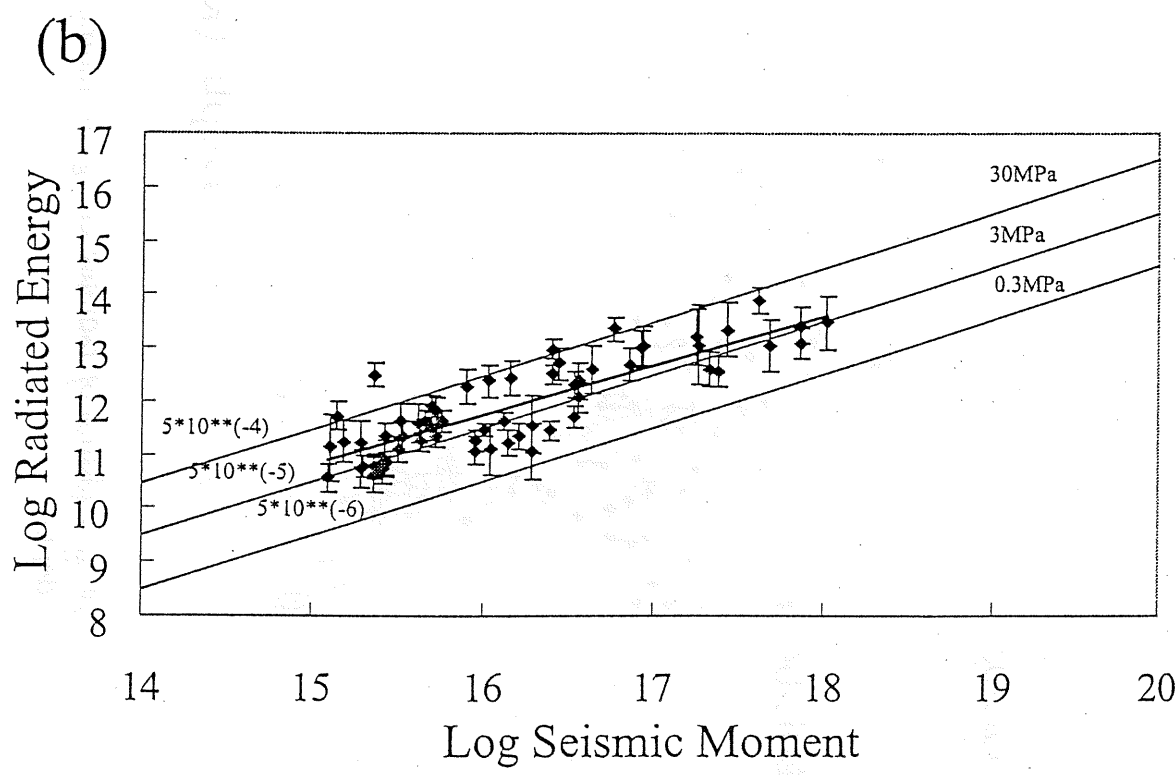
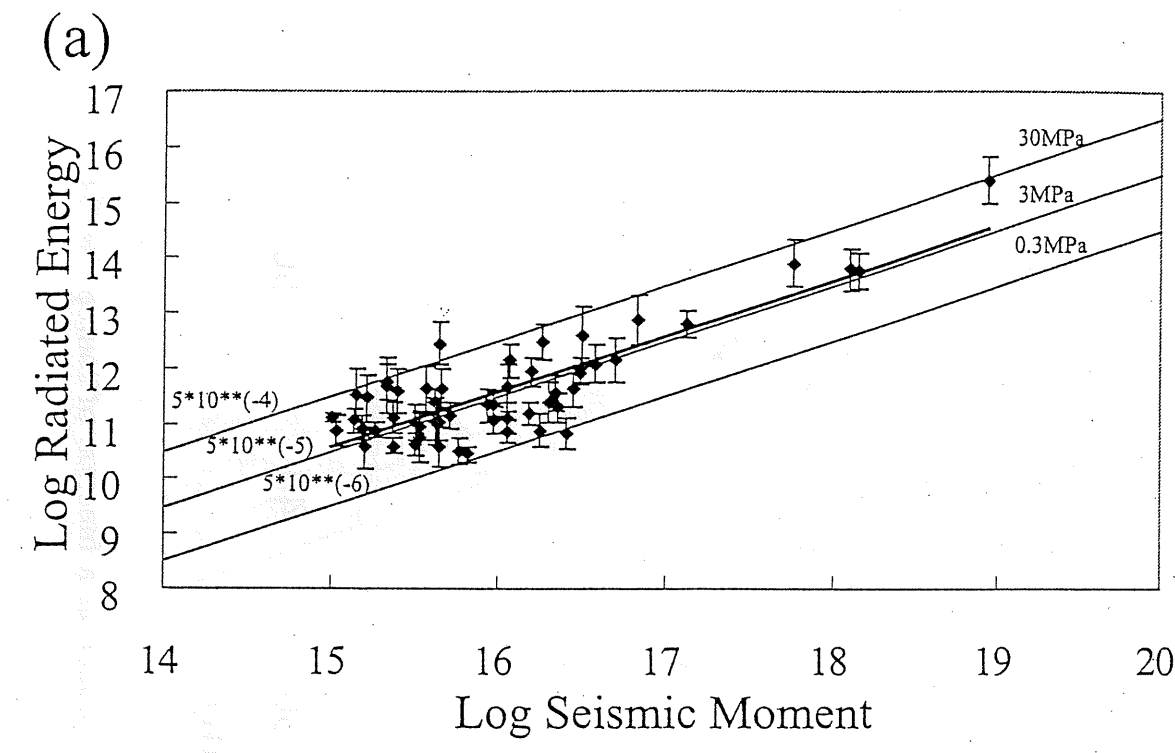
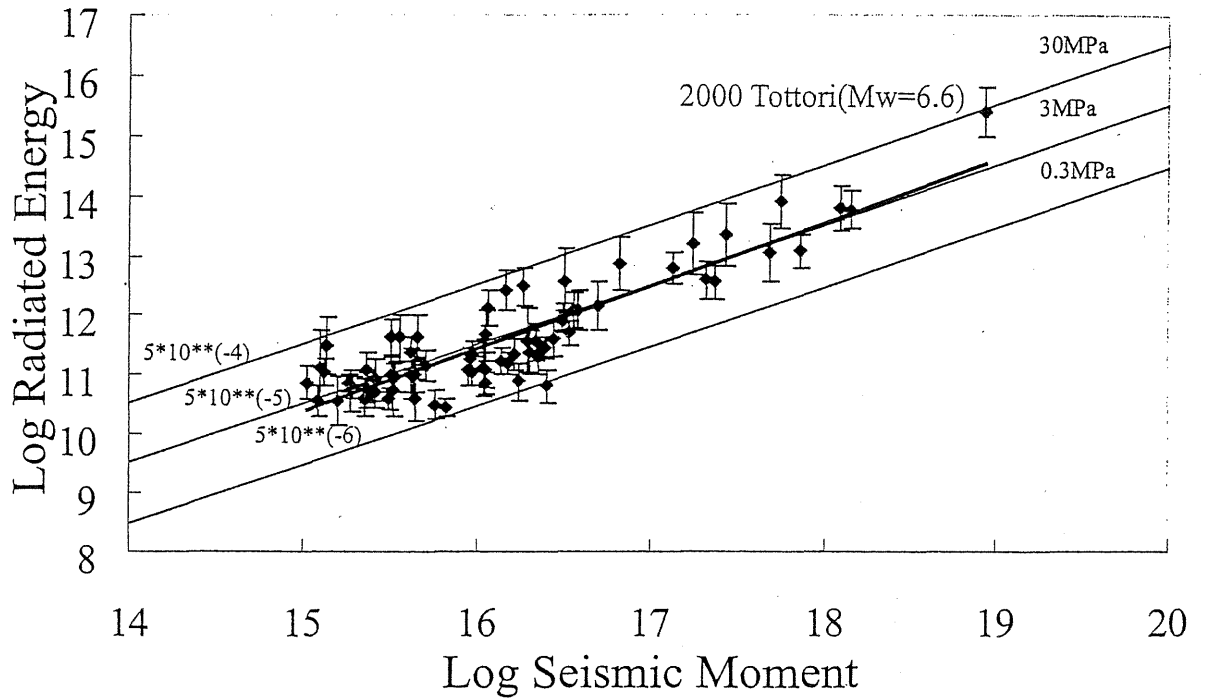


Fig. 16. Data separated into two groups by regional location. (a) Events under the main islands in Japan. (b) Offshore events.

(a) This Study



(b) Kanamori *et al.* (1993)

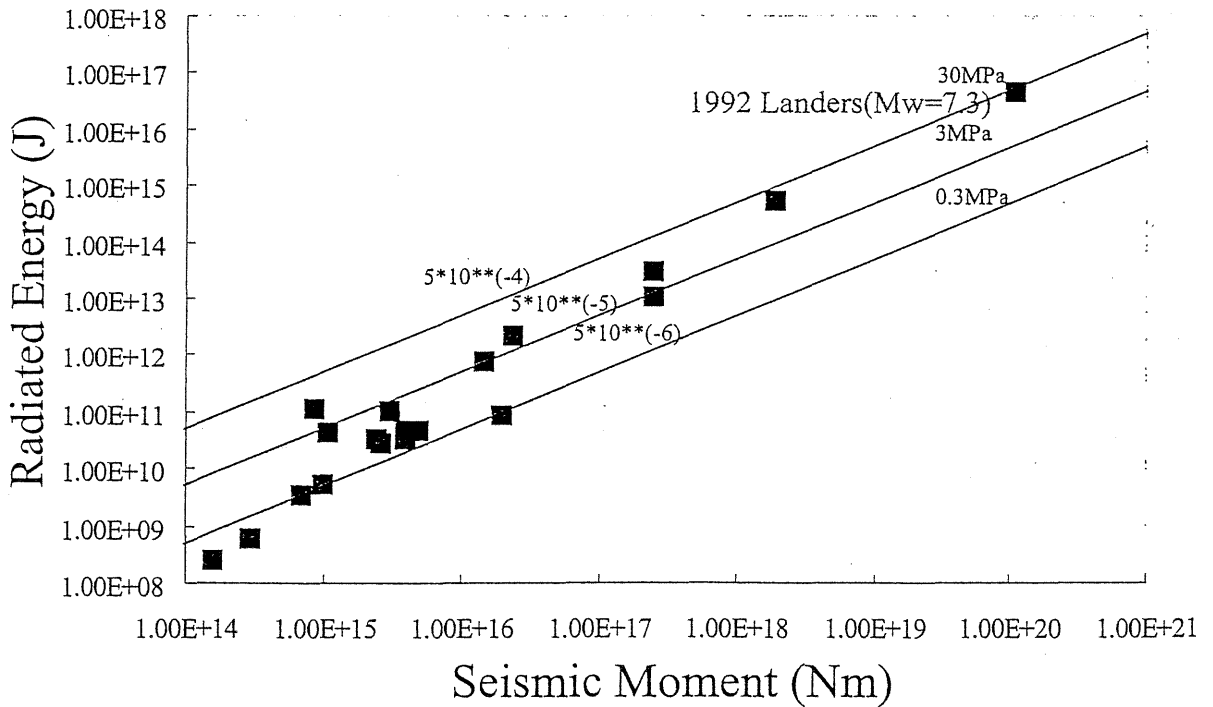


Fig. 17. (a) : The results of this study for earthquakes shallower less than 15 km. The largest event is 2000 Tottori earthquake ($M_w = 6.6$). For these shallow events, a slight trend is seen of increasing of radiated energy to seismic moment, as a function of seismic moment. (b) : Figure after Kanamori *et al.* (1993). The largest event of their study is the 1992 Landers earthquake ($M_w = 7.3$). Compared with (a), there is a larger increase in the ratio of radiated energy to moment, as a function of moment.

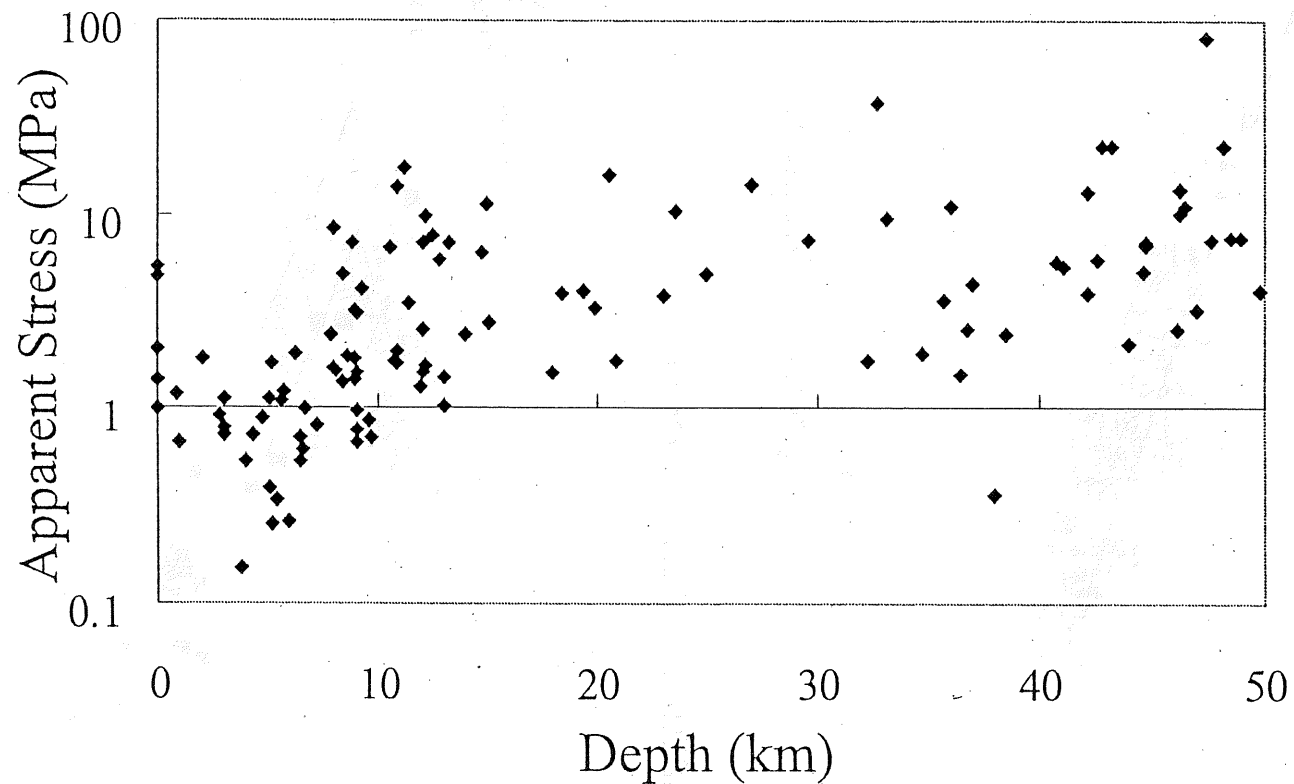


Fig. 18. Relationship between depth (km) and apparent stress (MPa). The definition of apparent stress is $\sigma_a = 2\mu \frac{E_s}{M_0}$, where μ is rigidity. Apparent stress seems to increase with depth.

Apparent Stress

Similar to other studies that estimate E_s , we took the ratio of E_s / M_0 and introduce the apparent stress (Wyss and Brune, 1968, 1971). From their studies, apparent stress $\Delta\sigma_a$ is defined as

$$\Delta\sigma_a = 2\mu E_s / M_0, \quad (9.2)$$

where μ is rigidity. Constant lines of $E_s / M_0 = 5 \times 10^{-4}$, 5×10^{-5} , 5×10^{-6} are shown in Fig.9-18. These correspond to values of apparent stresses of $\Delta\sigma_a = 30\text{MPa}$, 3MPa , 0.3MPa for a rigidity of $3 \times 10^4\text{MPa}$. Apparent stress does not have physical meaning as a stress measurement, but it is useful for discussing the relationship between the quantity of the radiated energy and the earthquake scale. Kikuchi and Fukao (1988) show that E_s / M_0 has a relationship as follows

$$\frac{E_s}{M_0} = \frac{1}{\mu} \left(\frac{\overline{\sigma_1} + \overline{\sigma_2}}{2} - \langle \overline{\sigma_f} \rangle \right) \quad (9.3)$$

where $\overline{\sigma_1}$, $\overline{\sigma_2}$ are the averaged initial and final stresses respectively, and $\langle \overline{\sigma_f} \rangle$ is the frictional stress averaged over the fault plane. Using the assumption of Orowan (1960), $\sigma_2 = \sigma_f$ i.e., the final stress is equal to the frictional stress, they obtain

$$\frac{E_s}{M_0} = \frac{\Delta\overline{\sigma}}{2\mu} \quad (9.4)$$

where $\Delta\overline{\sigma} = \overline{\sigma_1} - \overline{\sigma_2}$ is the average stress drop. From equation (9.4), the apparent stress is recognized as the indicator of stress drop for the simple Orowan model. Further more, Kanamori and Heaton (2001) connected E_s / M_0 ratio between the static stress drop $\Delta\sigma_s$ and the dynamic stress drop $\Delta\sigma_d$ as follows

$$\frac{E_s}{M_0} = \frac{(2\Delta\sigma_d - \Delta\sigma_s)}{2\mu} \quad (9.5)$$

From the results shown in Fig. 18, the apparent stress seems to depend on the depth. There are

larger apparent stresses for the deeper events. This implies proportionately more radiated energy and might be due to larger static stress drops for deeper earthquakes.

Conclusions

1. Including the effect of station corrections reduces the uncertainty and the overall value of the radiated energy estimate.
2. The energy estimates using this methodology are not improved by explicitly including the SH and SV radiation patterns. This is because both the direct S wave and scattered S waves of the coda are used for the energy estimate.
3. For the whole data set of 115 earthquakes with depths less than 50 km, the ratio of radiated energy to seismic moment is fairly constant and has a value of 9.10×10^{-5} .
4. There appears to be a depth dependence for the radiated energy estimates. For the shallowest earthquakes (less than 15 km depth) there is a slight trend of increasing ratio of radiated energy to seismic moment, as a function of seismic moment, which is consistent with the observations of shallow events in southern California.

Acknowledgments.

We thank National Institute for Earth Sciences and Disaster Prevention for use of the K-Net waveform data and focal mechanisms provided by the Freesia Network.

References

- Abercrombie, R. E., Earthquake source scaling relationships from 1 to 5 M_L using seismograms recorded at 2.5-km depth, *J. Geophys. Res.*, *100*, 24,015-24,036, 1995.
- Aki, K., and P. G. Richards, *Quantitative Seismology*, W. H. Freeman, New York, 1980.
- Boatwright, J., A spectral theory for circular seismic sources; simple estimates of source dimension, dynamic stress drop, and radiated seismic energy, *Bull. Seismol. Soc. Am.*, *70* 1-27, 1980.
- Boore, D. M., W. B. Joyner, and T. E. Fumal, Estimation of response spectra and peak accelerations from western north American earthquakes: an interim report part 2 *U.S. Geol.*

- Surv. Open file Report*, 94-127, 1994.
- Bullen, K. E., *An Introduction to the Theory of Seismology*, Cambridge University Press, Cambridge, p. 127., 1965.
- Choy, G. L., and J. L. Boatwright, Global patterns of radiated seismic energy and apparent stress, *J. Geophys. Res.*, 100, 18,205-18,228, 1995.
- Fukushima, Y., and T. Tanaka, A new attenuation relation for peak horizontal acceleration of strong earthquake ground motion in Japan, *Bull. Seismol. Soc. Am.*, 80, 757-783, 1990.
- Geological Survey of Japan, 1:1,000,000 Geological Map of Japan Ver. 3 CD-ROM version, Mathematical Geological Map G-1, *Geol. Surv. of Japan*, 1995. (in Japanese).
- Gutenberg, B., and C. F. Richter, Earthquake magnitude, intensity, energy, and acceleration, *Bull. Seismol. Soc. Am.*, 46, 105-145, 1956.
- Jost, M. L., T. Busselberg, O. Jost, and H.-P. Harges, Source parameters of injection-induced microearthquakes at 9 km depth at the KTB deep drilling site, Germany, *Bull. Seismol. Soc. Am.*, 88, 815-832, 1998.
- Kanamori, H., and T. H. Heaton, Microscopic and macroscopic physics of earthquakes, submitted, 2001.
- Kanamori, H., J. Mori, E. Hauksson, T. H. Heaton, L. K. Hutton, and L. M. Jones, Determination of earthquake energy release and M_L using TERRAScope, *Bull. Seismol. Soc. Am.*, 83, 330-346, 1993.
- Kikuchi, M., and Y. Fukao, Seismic wave energy inferred from long-period body wave inversion, *Bull. Seismol. Soc. Am.*, 78, 1707-1724, 1988.
- Mayeda, K., and W. R. Walter, Moment, energy, stress drop, and source spectra of western United States earthquakes from regional coda envelopes, *J. Geophys. Res.*, 101, 11,195-11,208, 1996.
- McGarr, A., On relating apparent stress causing earthquake fault slip, *J. Geophys. Res.*, 104, 3003-3011, 1999.
- Mori, J., R. E. Abercrombie, and H. Kanamori, Stress drops and radiated energies of aftershocks of the 1994 Northridge, California earthquake, submitted, 2001.
- Orowan, E., Mechanism of seismic faulting, *Geol. Soc. Am. Mem.*, 79, 323-345, 1960.
- Singh, S. K., and M. Ordaz, Seismic energy release in Mexican subduction zone earthquakes, *Bull. Seismol. Soc. Am.*, 84, 1553-1550, 1994.
- Wyss, M., and J. N. Brune, Seismic moment, stress, and Source Dimensions for earthquakes in the California-Nevada region, *J. Geophys. Res.*, 73, 4681-4694, 1968.
- Wyss, M., and J. N. Brune, Regional variations of source properties in southern California estimated from the ratio of short to long-period amplitudes, *Bull. Seismol. Soc. Am.*, 61, 1153-1167, 1971.

Estimates of Radiated Seismic Energy for Shallow and Intermediate-depth Earthquakes beneath Northeastern Japan

AI Kim and James Mori

Disaster Prevention Research Institute, Kyoto University

Kyoto JAPAN

Abstract

We studied radiated seismic energy for shallow (5–21km) and intermediate-depth earthquakes (64–156km) to understand the differences of source parameter scaling. In this study, we analyzed 32 shallow (M_{JMA} 3.6–5.4) and 37 intermediate-depth events (M_{JMA} 3.6–6.5), that occurred in northeastern Japan from June 1996 to December 2001, and which were recorded by at the K-net and Freesia network stations. Because the Q structure is different at shallow and intermediate-depths, propagation effects were obtained separately for the two depth ranges. Also site response is considered to be a function of incident angle, so it was also examined separately for the two depth ranges. The results of the estimation of radiated energy show that intermediate-depth earthquakes have nearly constant energy to moment ratios. This is different from shallow events, which from previous studies are reported to have increasing energy to moment ratios as a function of moment. Comparing radiated energies for the two depth ranges at large moments, those of the shallow events are somewhat higher than intermediate-depth events, but the apparent stresses are almost the same. This implies that the seismic efficiency of intermediate-depth events is lower. For deep events more energy may go into heat and fracture formation.

Introduction

A large number of observational data and studies indicate that shallow events occur because of either brittle shear fracture during creation of a fault or stick-slip friction on

a preexisting fault (Scholz, 1990). However, such frictional processes are strongly dependent on both thermal and pressure states. Because increasing temperature and pressure inhibit brittle fracture, such earthquakes should not occur below 30km depth (Ito, 1990). In this view, the occurrence of intermediate-depth (70–300km) and deep (300–700km) earthquakes requires a different explanation.

Since Wadati (1927), it is well known that deep earthquakes occur and it is thought that they are located in the slab where the temperature is relatively low, although the pressure is still very high. Some researchers suggested that intermediate-depth events occur because of dehydration embrittlement (e.g. Seno, 2001) but because laboratory experiments show hydrothermal metamorphism can not occur at locations more than 4–6km from the surface of the slab, this hypothesis can not explain the observed double seismic zone of subducting slabs. So there is not confirmation for this explanation of deep events (Karato, 2000).

To investigate the source process of deeper earthquakes, we studied the radiated seismic energy, E_s , for intermediate-depth and shallow events, which is important for understanding the rupture process of those earthquakes. The energy associated with earthquake can be divided into the radiated seismic energy, heat loss during faulting, and energy for creation of fracture (Kanamori *et al.*, 1993). Among these parameters E_s is the only quantity which can be observed from seismological data. E_s is only a part of the energy budget, however, it is still an important parameter for understanding the rupture processes.

Studies of E_s have been done by many researchers, for example Gutenberg and Richer (1942, 1956a, 1956b), Boatwright and Choy (1985), Vassilou and Kanamori (1982), Kikuchi and Fukao (1988), Kanamori *et al.* (1993). However, E_s for deep and intermediate-depth earthquakes have been estimated using only teleseismic data because of the lack of stations near the hypocenters. Using teleseismic data limits the studies to large earthquakes. There are few studies on E_s for smaller deep and intermediate-depth events because one needs short period-information. To understand the rupture process and source parameter scaling of these events and to discuss differences between deep and shallow events it is necessary to study E_s for small events.

The goal of this study is to estimate E_s for shallow and intermediate-depth earthquakes using short-period data and to compare their energy to moment ratios. E_s is directly dependent on the absolute amplitudes of the estimated ground velocity. In this study, path and site effects were considered carefully because they have an important effect on the energy estimates. Both these corrections were obtained as depth and

frequency dependent values. The ray paths from the shallow and intermediate-depth earthquakes pass through regions of significantly different Q . For example, Kamura and Uetake (2001) estimated the Q s structure beneath the Japan Island, and obtained values of about 400 for 90-120km depths and about 200 for 0-30 km depths in the Tohoku region. So it is necessary to examine path effects separately for each of the two depth ranges events.

Data

We used three components records from the Fundamental Research on Earthquakes and Earth's Interior Anomaly (Freesia) and the Kyoshin-net, both operated by the National Institute for Earth Sciences and Disaster Prevention (NIED). We analyzed 32 and 37 events for shallow and intermediate-depth events, respectively, that occurred in northeastern Japan from June 1996 to December 2001 (Figure 1). For the shallow events, the hypocentral depth ranged from 5 to 20km, and the magnitude ranged from 3.6 to 5.4 on the JMA scale. Only stations at hypocentral distances less than 60km were used to avoid the effects from surface waves. For the deeper events, the hypocentral depth ranged from 64 to 156km, and the magnitude ranged from 3.6 to 6.5. Stations at hypocentral distances less than 170km were used. The number of stations used for the energy estimation of each earthquake was from 2 to 21. These stations had signal to noise ratios greater than 2. Examples of waveforms and spectra are shown in Figure 2 and the information for all events is listed in Tables 1a and b.

All of the stations of the Freesia network are equipped with broadband seismometers and a data logger with a 24-bit digitizer at 80 Hz. The gain of the instrument is constant to ground velocity between 0.027 and 7Hz. For the Freesia sites the subsurface structure is not well known, and only geological information such as rock type is available at each station.

Kyoshin network stations have a strong motion accelerometer and data logger with resolution of 16-bits sampled at 100Hz. The gain of the instruments is constant to ground acceleration to 20Hz. The subsurface structure and S wave velocity beneath K-net stations are well known. All stations of the K-net and Freesia network used in this study are plotted in Fig 3.

Figure 1.

Map of epicenters for earthquakes used this study. Open stars are shallow events ($5\text{km} < \text{depth} < 25\text{km}$). Solid stars are intermediate-depth events ($67\text{km} < \text{depth} < 156\text{km}$).

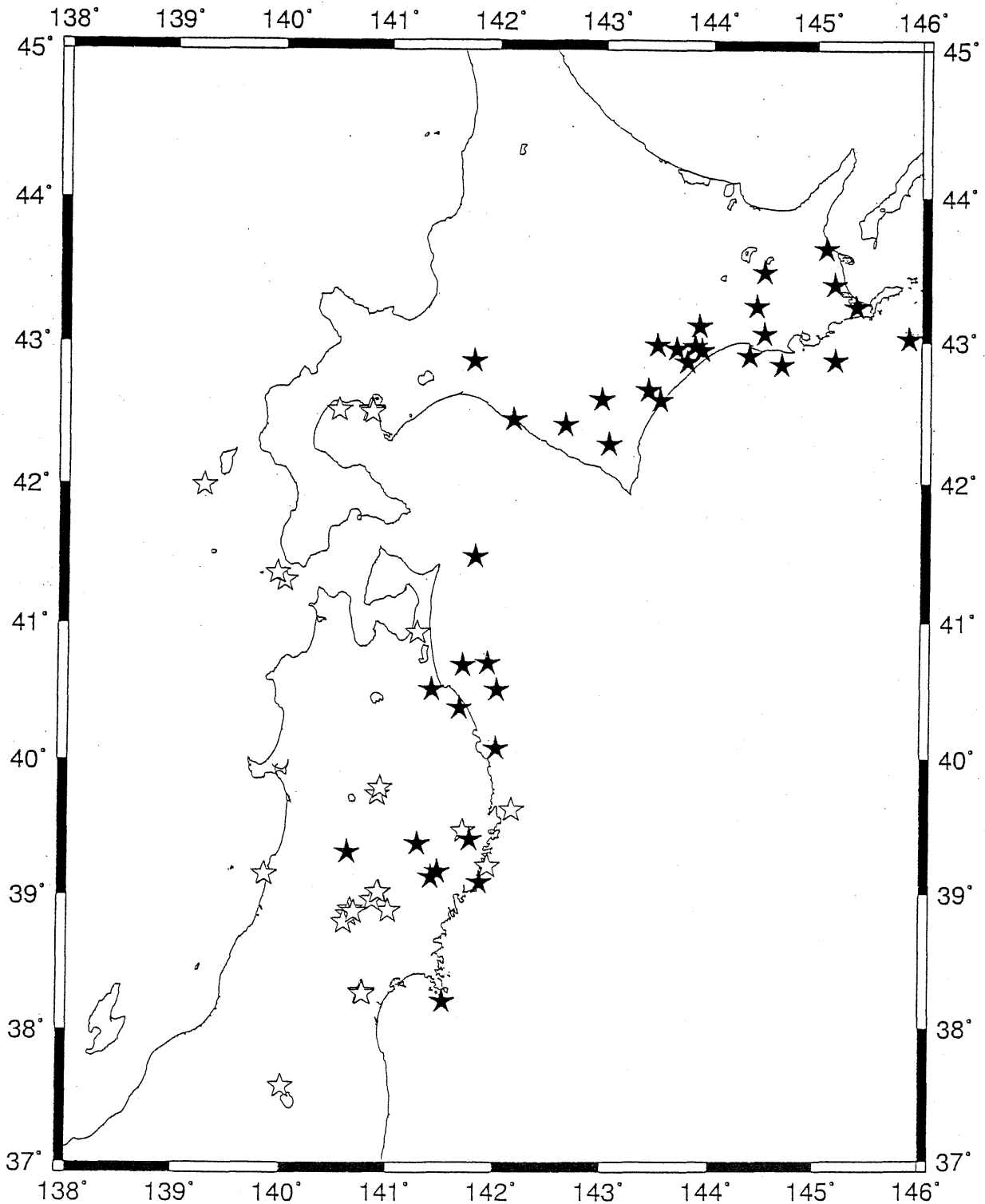
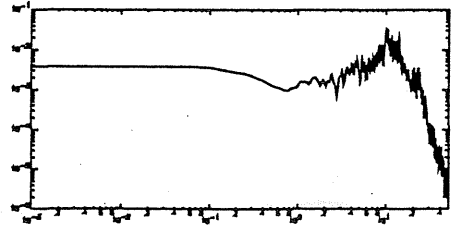
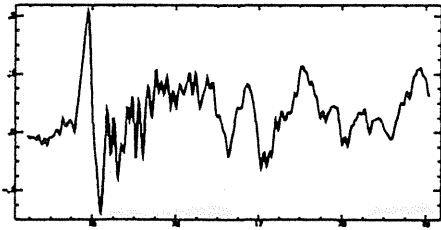


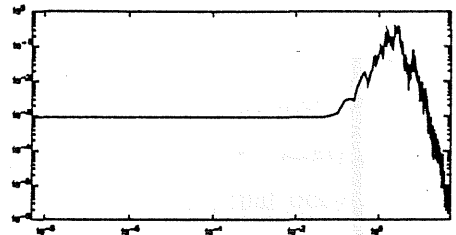
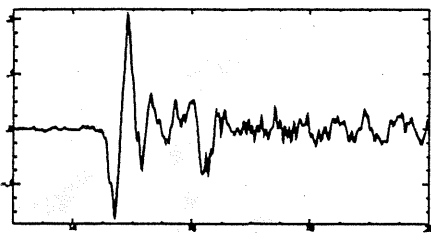
Figure 2

Example of waveforms, spectra and noise level.
All data used this study have signal to noise ratios which are greater than 2.

Shallow earthquake 02/25/00 IWT007 Δ : 9.24km



Intermediate-depth earthquake 12/08/00 HDK083 Δ : 60.74km



Signal and Noise(0.1Hz-10Hz)

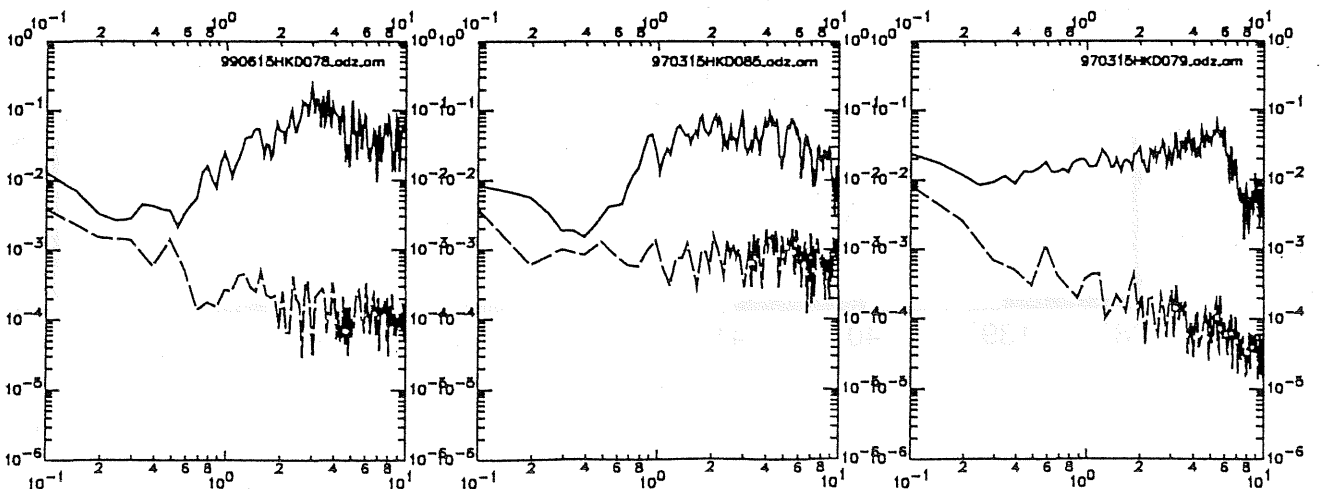
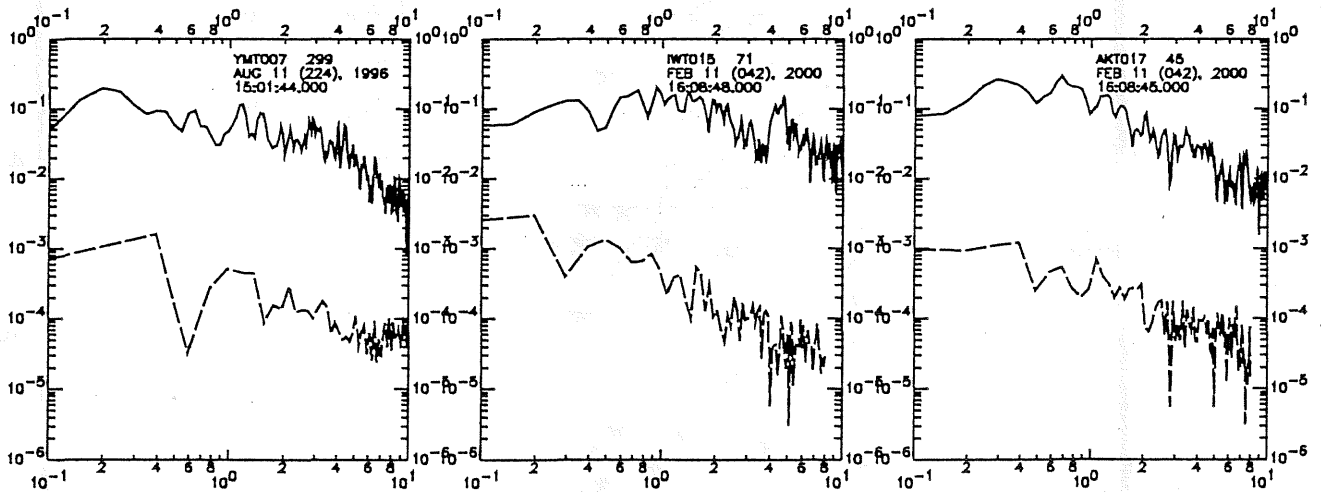
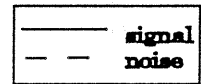


Figure 3

Map of stations for K-net (Solid triangles) and Freesia (Solid circles) both of those operated by NIED (National Research Institute for Earthquake Science and Disaster Prevention).

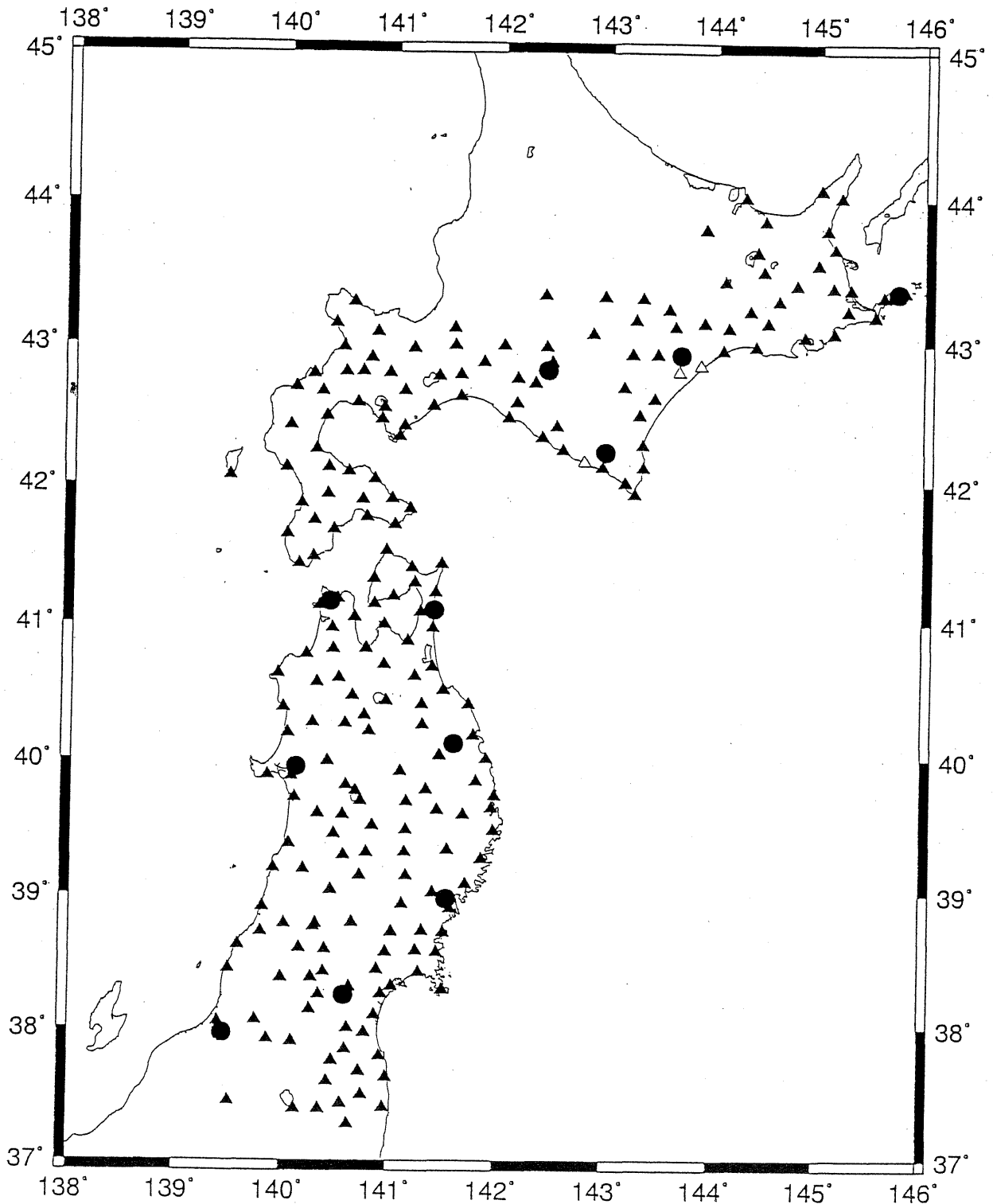


Table 1 a)

List of events used in this study. (shallow events)

Date(mm/dd/yy/hh:mm)	Latitude(deg)	Longitude(deg)	Depth(km)	Mo(Nm)	Es($\times 10^{10}$ J)	RMS	M _{JMA}
06/05/96/09:37	39.473	141.703	12.80	1.12e15	9.269e9	0.638	4.1
08/11/96/03:54	38.893	140.653	8.90	1.06e17	1.651e12	0.612	5.4
08/11/96/05:26	38.855	140.637	9.70	5.62e14	3.184e9	0.526	3.9
08/14/96/07:52	38.800	140.595	8.50	7.94e14	9.450e9	0.637	4.0
01/23/97/14:44	38.880	141.010	8.60	3.98e14	8.862e9	0.606	3.8
02/11/97/20:12	39.628	142.162	12.70	5.62e14	4.890e9	0.443	3.9
04/26/97/13:44	41.313	140.023	11.30	1.12e15	8.963e9	0.503	4.1
02/21/98/22:17	41.989	139.268	21.68	9.79e14	7.547e9	0.477	4.0
09/03/98/17:10	39.745	140.900	9.80	5.62e14	3.463e9	0.481	3.9
09/03/98/21:57	39.794	149.927	11.05	3.66e14	2.745e9	0.496	3.7
09/15/98/16:18	38.275	140.766	12.99	2.95e14	1.320e9	0.483	3.6
09/15/98/16:24	38.278	140.766	13.25	3.19e16	8.457e11	0.573	5.0
09/15/98/17:56	38.272	140.773	13.06	7.94e14	1.459e9	0.472	4.0
09/26/98/23:07	38.271	140.758	13.44	3.98e14	3.896e8	0.489	3.8
10/24/98/23:19	38.264	140.769	12.80	5.62e14	8.189e9	0.572	3.9
01/08/99/04:10	38.963	140.858	13.55	2.81e14	1.674e9	0.499	3.7
02/26/99/14:18	39.154	139.854	19.41	7.16e16	9.760e11	0.348	5.1
03/08/99/17:46	39.157	139.851	20.74	1.75e15	2.349e9	0.438	4.2
04/19/99/03:44	39.020	140.919	12.07	5.06e15	5.236e10	0.671	4.3
09/13/99/05:32	40.932	141.267	14.72	1.26e15	1.783e10	0.586	4.0

Table 1 a) (Continued)

01/10/00/17:33	38.875	140.686	12.61	2.95e15	1.273e10	0.462	4.2
02/18/00/22:38	39.020	140.910	11.83	2.81e14	5.932e9	0.489	3.7
02/25/00/15:25	39.213	141.941	16.18	3.98e14	6.583e9	0.542	3.8
03/29/00/19:40	42.526	140.821	7.04	3.90e14	5.291e9	0.475	3.7
03/29/00/20:01	42.522	140.522	6.89	2.22e14	4.687e9	0.511	3.6
03/30/00/02:54	42.524	140.824	6.80	1.47e15	3.387e10	0.358	4.0
03/30/00/05:16	42.524	140.824	7.28	3.01e14	1.785e9	0.485	3.6
03/30/00/18:51	42.513	140.835	7.88	3.05e15	1.372e10	0.449	4.0
03/31/00/06:48	42.516	140.814	8.20	3.90e14	4.453e9	0.516	3.7
04/01/00/03:12	42.505	140.829	7.81	2.15e16	9.343e10	0.327	4.6
04/12/00/00:08	41.367	139.953	13.24	1.62e15	8.230e9	0.688	4.3
04/26/00/05:09	37.571	140.016	14.23	3.98e14	2.652e9	0.403	3.8

Table 1 b)

List of events used in this study. (intermediate-depth events)

Date(mm/dd/yy/hh:mm)	Latitude(deg)	Longitude(deg)	Depth(km)	Mo(Nm)	Es($\times 10^{10}$ J)	RMS	M _{JMA}
01/11/97/04:53	40.083	142.007	72.60	1.12e15	1.785e10	0.539	4.1
03/04/97/11:57	42.970	143.840	84.00	7.50e14	9.213e9	0.583	3.9
03/23/97/10:57	40.517	141.402	83.30	1.99e14	4.543e9	0.425	3.6
03/15/97/13:54	42.840	144.663	72.80	1.50e15	2.563e10	0.511	4.1
03/20/97/14:30	42.283	143.037	72.70	3.00e15	2.253e11	0.659	4.3
03/25/97/02:41	42.590	143.515	63.90	3.92e14	9.455e9	0.542	3.7
05/04/97/06:08	43.242	145.373	103.50	1.93e15	5.403e10	0.563	4.2
06/05/97/08:15	42.597	142.970	106.50	1.98e15	4.121e10	0.681	4.2
06/07/97/21:33	42.905	144.353	112.30	1.42e15	3.278e10	0.440	4.1
07/17/97/19:09	43.398	145.170	124.90	1.51e15	6.431e10	0.545	4.1
10/27/97/04:06	39.320	140.619	119.77	1.43e17	3.120e12	0.470	5.1
11/03/97/03:19	41.483	141.803	68.52	6.89e14	3.264e10	0.369	4.0
11/15/97/16:05	43.647	145.088	153.10	1.34e18	3.811e13	0.515	6.1
12/23/97/04:08	42.978	143.488	113.31	4.62e16	8.471e11	0.638	5.1
04/12/98/19:18	42.418	142.635	78.70	3.38e14	7.600e9	0.371	3.7
02/17/99/08:43	42.454	142.150	117.97	4.87e14	10.452e9	0.436	3.8
05/13/99/02:59	42.944	143.909	103.57	1.72e18	1.163e14	0.412	6.4
06/13/99/07:57	43.486	144.495	145.45	1.63e15	4.871e10	0.567	4.1
06/15/99/17:13	43.058	144.497	90.38	2.93e15	3.489e10	0.444	4.3
08/08/99/20:29	40.514	142.011	89.97	4.21e14	9.456e10	0.357	3.7

Table 1 b) (Continued)

08/25/99/10:07	42.862	143.770	113.270	1.99e14	1.952e10	0.372	3.6
08/28/99/18:01	40.710	141.927	67.89	3.11e14	6.389e9	0.569	3.6
12/18/99/22:30	42.954	143.671	114.70	3.01e15	9.264e10	0.505	4.3
03/06/00/04:04	39.093	141.863	86.10	1.99e14	6.341e9	0.323	3.6
03/09/00/02:28	42.870	145.178	84.31	3.71e14	2.634e9	0.324	3.7
04/28/00/17:57	39.172	141.466	77.33	2.81e14	8.273e9	0.516	3.7
09/06/00/01:59	43.112	143.884	126.08	7.90e14	3.763e10	0.309	3.9
12/06/00/15:12	42.660	143.404	86.67	2.01e15	1.512e10	0.454	4.2
12/08/00/06:14	43.248	144.421	128.83	2.22e15	5.218e10	0.575	4.2
12/10/00/21:30	39.130	141.404	79.20	8.44e14	8.982e10	0.671	4.0
02/13/01/04:15	42.866	141.784	147.21	6.89e14	7.125e10	0.437	3.9
01/30/01/19:23	38.205	141.520	82.52	3.27e14	7.347e9	0.528	4.1
04/05/01/07:22	39.413	141.768	104.77	5.81e15	1.729e11	0.474	4.3
04/06/01/20:07	40.382	141.662	71.93	2.81e14	5.753e9	0.348	3.7
04/27/01/02:48	43.020	145.881	83.05	1.03e18	8.113e13	0.559	5.9
06/16/01/21:22	40.693	141.6935	75.02	1.99e14	8.245e9	0.323	3.7
12/02/01/22:01	39.382	141.2745	128.06	5.34e18	3.784e14	0.413	6.5

Method

To estimate the energy, we follow Kanamori et al. (1983). Consider the particle-motion velocity, V_0 , on a small sphere, with radius r_0 surrounding the earthquake. The observed velocity of ground motion far from the sphere, V , can be expressed as

$$V = V_0 C P(r)/P(r_0) G \quad (1)$$

where C is constant which includes the free surface effect and radiation pattern, r is the focal distance to the station (*i.e.*, $r^2 = \Delta^2 + h^2$, Δ : epicentral distance, h : depth), and G is the site amplification factor. The function P is the attenuation function, which includes the effects of geometrical spreading, attenuation and scattering. Procedures for obtaining P and G will be described later.

In this study, the radiated S-wave energy were assumed to be close to the total radiated energy, since the P-wave energy is only 4% of the S-wave energy (Haskell, 1964), which is much smaller than the uncertainties in the E_s estimations. The radiated S-wave energy from a small sphere is written by

$$E_\beta = \rho_0 \beta_0 \int_{S_0} V \hat{f}(f) df dS \quad (2)$$

where ρ_0 and β_0 are the density and S-wave velocity, respectively, of the medium at the focal sphere(*e.g.* Haskell, 1964). The surface integral is taken over the focal sphere and the integration over frequency, f , is taken over the S-wave spectrum.

Substituting (1) into (2), we obtain

$$E_\beta = \rho_0 \beta_0 \int_{S_0} V \hat{f}(f) C^{-2} [P_0(f)/P(f)]^2 G^{-2}(f) df dS \quad (3)$$

Propagation effects

We assume that the data consist of S-waves, which have a geometrical spreading proportional to the inverse of the hypocentral distance, R , so an attenuation function P

can be written as

$$P = R^{-1} \exp(-\alpha(f)R) \quad (4)$$

The observed ground velocity at the station in the frequency domain can be expressed by

$$V(f) = C S(f) G(f) R^{-1} \exp(-\alpha(f)R) \quad (5)$$

where $S(f)$ is the source spectra and α is written by

$$\alpha(f) = \pi f / \beta_0 Q(f) \quad (6)$$

where $Q(f)$ is the quality factor.

Because of the small earthquake sizes it was assumed that seismic waves are radiated symmetrically from the source. Liu and Helmberger (1985) compared observed short-period ground motion amplitudes with theoretical radiation pattern coefficients which were calculated from source mechanisms for M5 range events. As a result, they found that the amplitude is azimuthally symmetric for frequency above 0.5Hz and for frequencies below 0.5 Hz, amplitudes have dependence less than expected. In this study, we consider it is appropriate to use an azimuthally independent average radiation pattern of 0.63, which is calculated by Boore and Boatwright (1984).

To obtain the attenuation function we used a two-fold spectral ratio method (Matsuzawa *et al*, 1989). In this method there are two stations which record two common events. Using spectral ratios, the source, site and free surface cancel, so that one can obtain a distance dependent attenuation relationship.

$$\frac{V_{1,A}(f) V_{2,B}(f)}{V_{1,B}(f) V_{2,A}(f)} = \frac{S_1(f) P_{1,A}(f) G_{1,A}(f) S_2(f) P_{2,B}(f) G_{2,B}(f)}{S_1(f) P_{1,B}(f) G_{1,B}(f) S_2(f) P_{2,A}(f) G_{2,A}(f)} \quad (7)$$

(*ith event, i = 1,2,3...*, *jth station, j = A,B,C...*)

Assuming $G_{1,A}(f) = G_{1,B}(f)$ and $G_{2,A}(f) = G_{2,B}(f)$,

this can be expressed with (5) as

$$\frac{V_{1,A}(f) V_{2,B}(f)}{V_{1,B}(f) V_{2,A}(f)} = \left(\frac{R_{1,A} R_{2,B}}{R_{1,B} R_{2,A}} \right)^{-1} \exp \left[-\alpha(f) (R_{1,A} - R_{1,B} + R_{2,B} - R_{2,A}) \right] \quad (8)$$

Using this method, attenuation functions for shallow and intermediate-depth events were calculated separately. We also divided the stations into two groups for intermediate-depth earthquakes, depending on the ray path from the hypocenter, because the effect of the slab significantly affects the attenuation. One group is for rays that pass mainly through the slab, the other group is for rays that do not pass through the slab. When determining the type of ray path, we used Kamiya *et al.* (1985) which is a depth contour of the slab determined by plotting microseismicity. Table 2 shows the area and number of station pairs used in this method.

3.2 Site amplification factor

After correcting for the path effects, one can estimate the site effect, from equation (5)

$$V_{i,j}(f)/P_{i,j}(f) = S_i(f) G_{i,j}(f) \quad (9)$$

Generally, the site amplification factor can be a function of the incident angle, so we calculated it separately for the two depth ranges. In this study, the site amplification coefficients were determined using spectral ratios of the S-wave at a reference station and at each station. This method does not give absolute site response, but information relative to the reference station

Reference stations were chosen using this procedure. First we obtain the log average of (9) for all events at the *j*th station.

$$\log \overline{S(f) G_j(f)} = 1/n \sum_{i=1}^n \log S_i(f) G_{i,j}(f) \quad (10)$$

The station having the smallest $\overline{S(f) G_j(f)}$ and the highest S-wave velocity beneath the station was chosen to be the reference station. Next, all products of source

and site effect were divided by those of the reference station and to obtain the site coefficient, $G_{ij}(f)$ for each i -th event and j -th station. Finally average station site amplification factors were obtained by calculating the log average over all the events, at each station.

S wave energy estimation

Assuming a symmetric radiation pattern, and integrating equation (3) over space, the energy can be expressed as

$$E_{\beta} = 4\pi r_0^2 \rho_0 \beta_0 \int V^2(f) C^{-2} [P_0(f)/P(f)]^2 G^{-2}(f) df \quad (11)$$

where r_0 is radius of a small sphere around the earthquake (Kanamori, 1993). Numerical values were assumed to be $\rho_0 = 2.5g/cm^3$, $\beta_0 = 2.7km/s$ for shallow events and $\rho_0 = 3.0g/cm^3$, $\beta_0 = 4.5km/s$ for intermediate-depth events.

In the method described above, a point source was assumed because events which were used here were relatively small. However when considering larger events it will be necessary to modify to a finite fault.

Although data were selected to avoid effects of surface waves, observed waveforms sometimes consisted of several pulses. It is not always possible to identify exactly each of these phases. To avoid this complexity as much as possible, direct S waves having enough large amplitudes compared with later phases were chosen for this study.

Results

Attenuation function

For estimates of radiated energy it is sufficient to calculate the function $\alpha(f)$ empirically in equation (4). However one of purpose for this study is to determine path effects as correctly as possible. So it is useful to evaluate the Q values including other information.

From equation (4) $\alpha(f)$ values were obtained and converted to a frequency dependent Q(f) using

$$Q(f) = \pi f / \beta_0 \alpha(f) \quad (12)$$

where $\beta_0 = 2.7 \text{ km/s}$, 4.5 km/s were assumed for shallow and intermediate-depth earthquakes, respectively. In this study, it is assumed that $Q(f)$ is the apparent Q consisting of both intrinsic and scattering Q . Figure 4 shows the results of $Q(f)$ for shallow events, which has an uncertainty of about 20% (Table 2).

The frequency dependence shows a trend that is greater than f^1 . It has been reported that when the geometrical spreading was assumed to be the inverse of the ray length, the frequency dependence of $Q(f)$ is about $f^{0.7}$ (Kinoshita, 1993; Satoh *et al.*, 1997). Satoh *et al.* (1997) studied frequency dependent Q in the eastern Tohoku district for events that occurred in the subduction zone. However, other studies have obtained a frequency dependence of about $f^{1.5}$ for crustal events in Tohoku, Japan (e.g. Satoh *et al.*, 1998). The reason for this difference might be that ray paths were different between earthquakes in the crust and in the subduction zone. In this study shallow events were limited these that are occurred in the crust, so the results compare favorably with the crustal results from Tohoku.

Figure 5 shows $Q(f)$ for intermediate-depth earthquakes which occurred in the Hokkaido region. The solid triangles show $Q(f)$ for rays that pass mainly through the slab (path 1) and open triangles indicate $Q(f)$ for rays that do not pass through the slab (path 2). $Q(f)$ for path 1 have somewhat larger values compare with that of path 2, because these ray pass through high Q slab longer than path 1. The dependence is almost the same between shallow and intermediate-depth events for each area.

Figures 6a and 6b show the individual energy estimates plotted as a function of distance and normalized by the average energy. From this plot it can be said that there is no strong systematic trend with distance, which suggests that the estimation of the attenuation function was appropriate for this study.

Site responses

Figures 7a and 7b show the map of predominant frequency of ground conditions of each station for the two depth ranges. There are no significant differences for the shallow and intermediate-depth events in both predominant frequency and amplitude. However, the site response calculated at a given station for intermediate-depth earthquakes have less scatter than for shallow events. These reason for this might be because the site amplification depends on the incidence angle; shallow events have a

Region	Number of event	Station pairs	RMS
Tohoku (Shallow)	9	44	0.081
Tohoku (Intermediate-depth)	6	29	0.087
Hokkaido (Shallow)	5	38	0.096
Hokkaido (Intermediate-depth, path 1)	4	18	0.119
Hokkaido (Intermediate-depth, path2)	7	27	0.092

Table 2

Data used for estimation of frequency dependent attenuation factor.

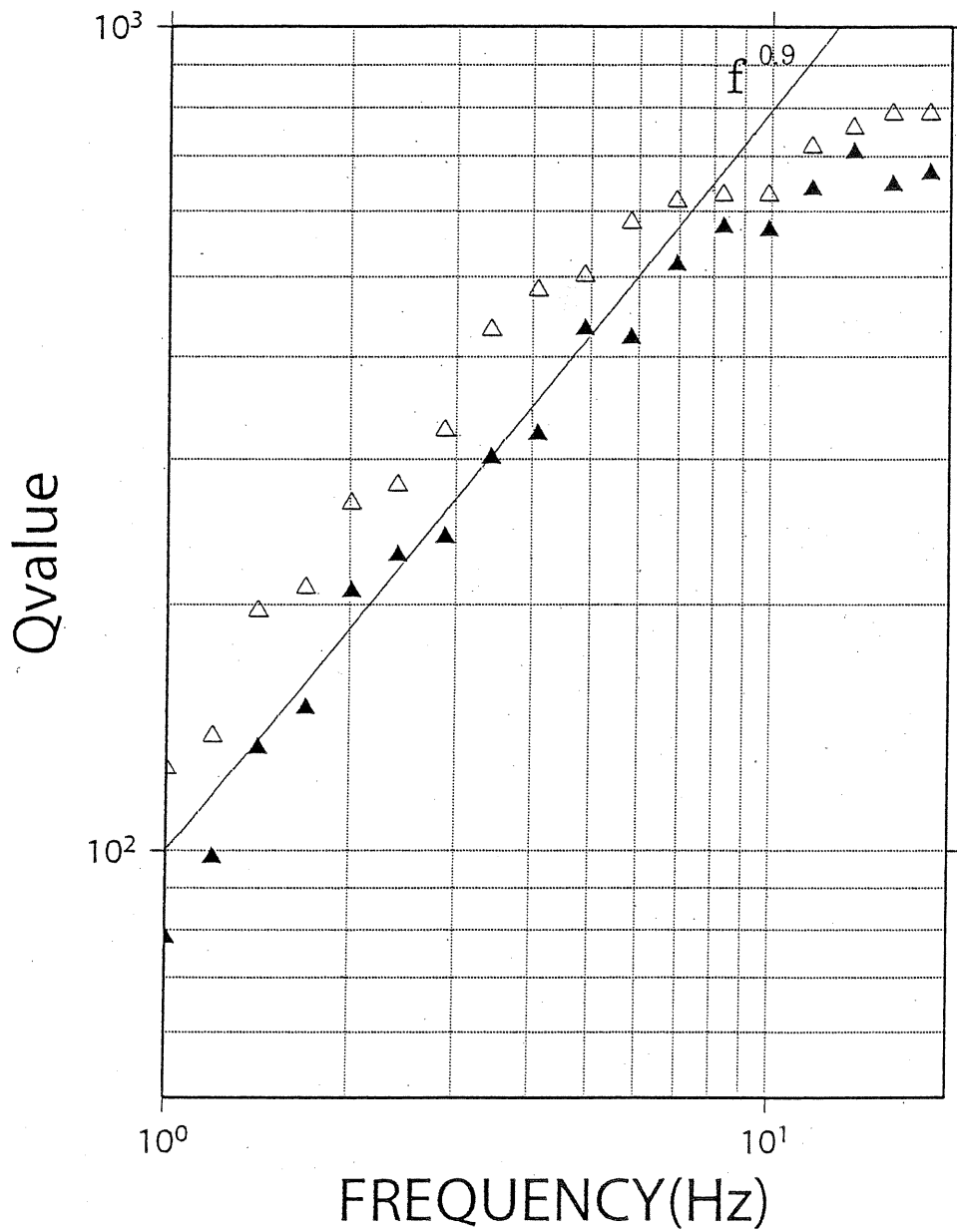


Figure 4

Frequency dependent Q values for shallow events. Solid circles indicate values from the Tohoku region and open circle indicate values from the Hokkaido region.

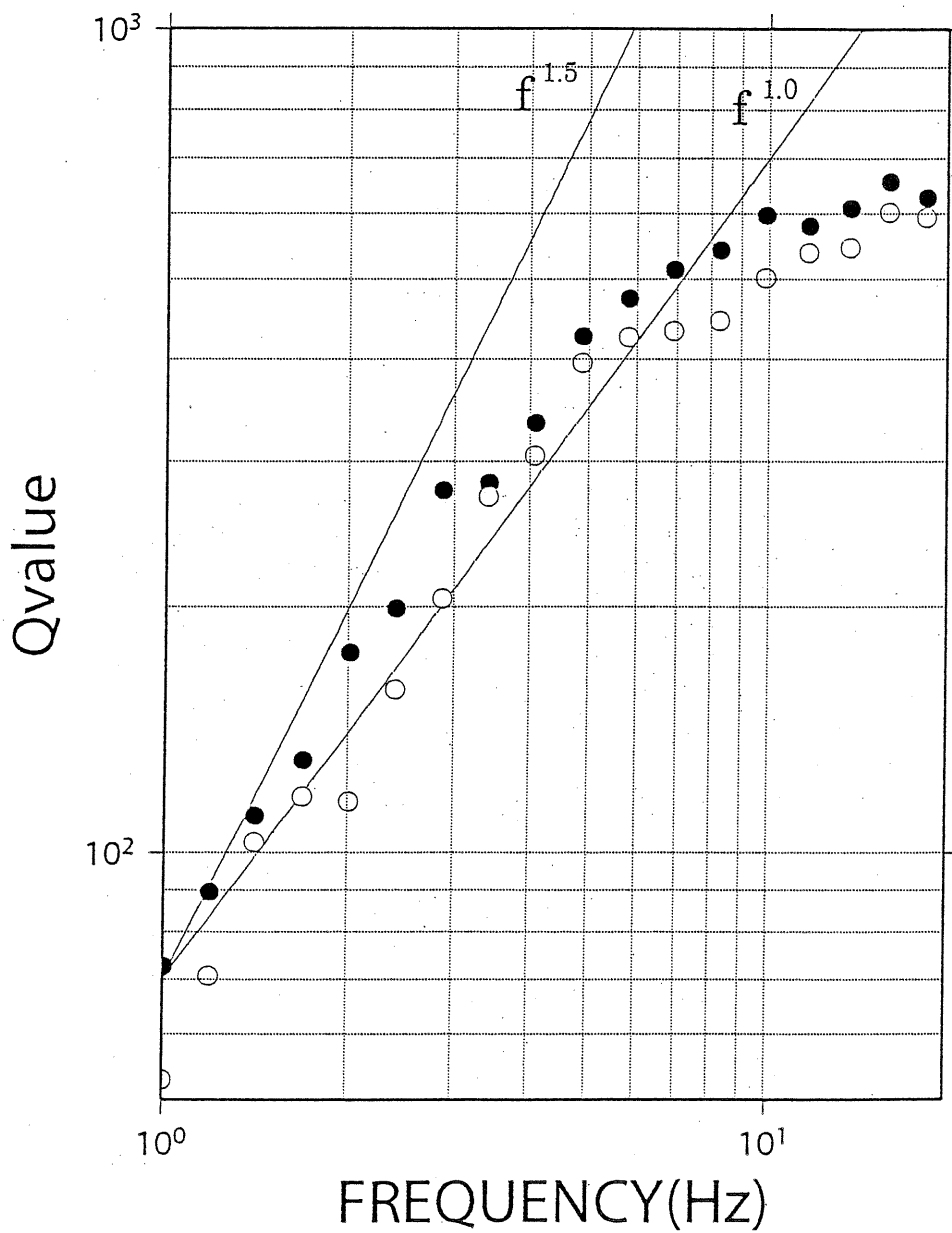


Figure 5

Frequency dependent Q value for Intermediate-depth earthquakes in the Hokkaido region. Solid triangles show Path 1 (rays that pass mainly through the slab) and open triangles show Path 2 (rays that do not pass trough the slab).

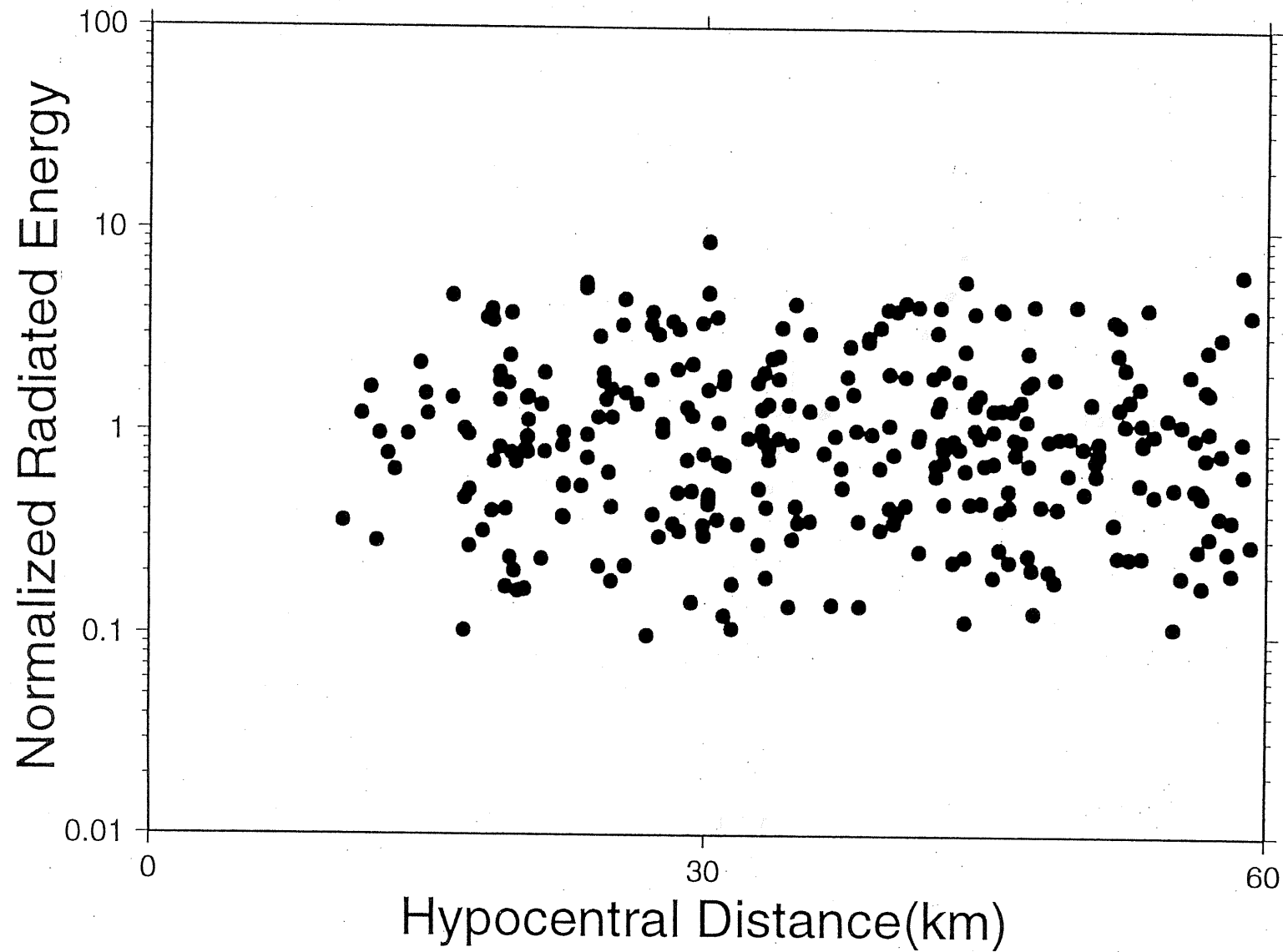


Figure 6 a)

Individual energy estimates plotted as a function of distance and Normalized by the averaged energy for shallow earthquakes

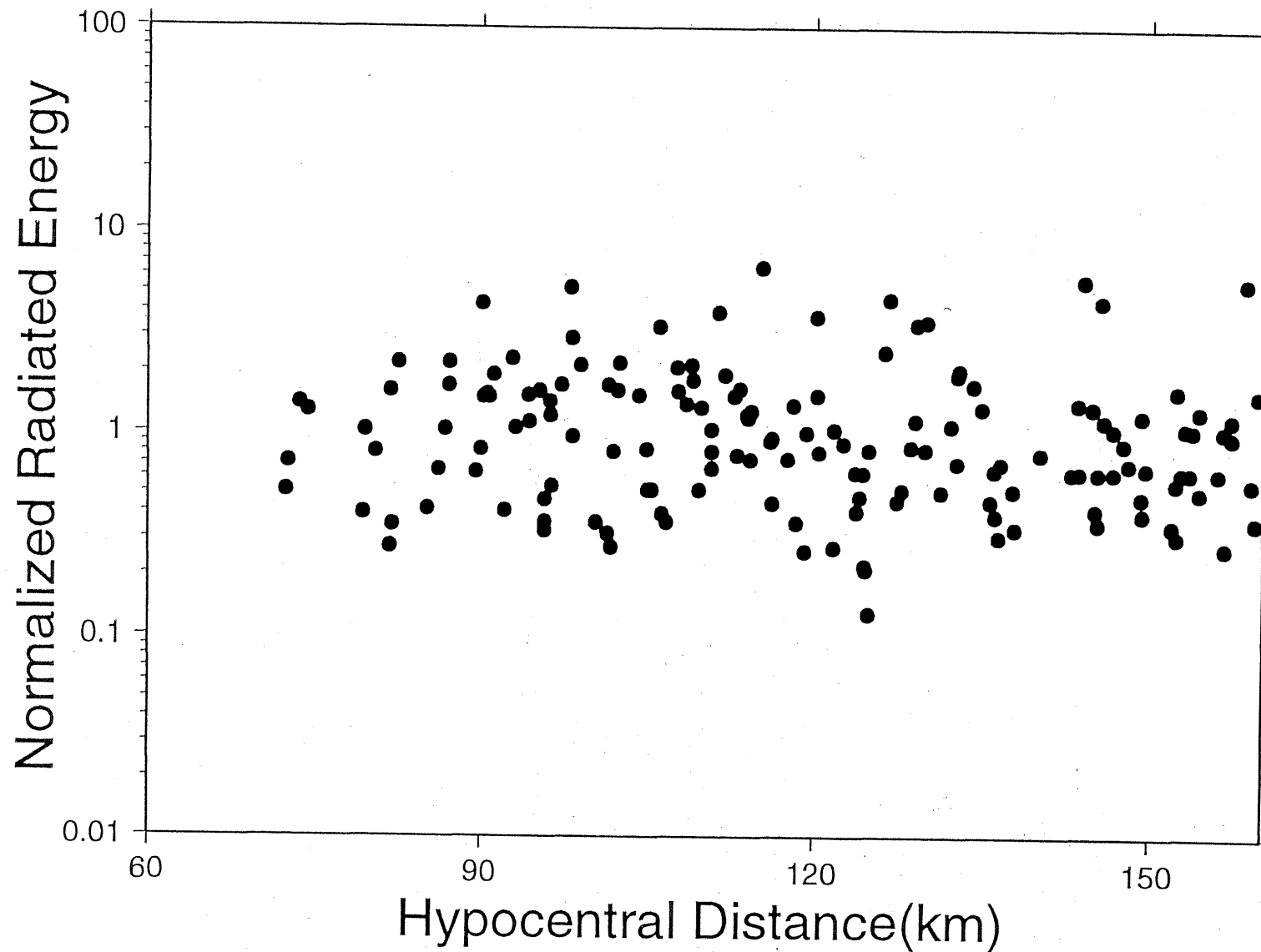


Figure 6 b)

Individual energy estimates plotted as a function of distance and Normalized by the averaged energy for intermediate-depth earthquakes

Figure 7 a)

Map of the predominant frequency of ground motions at sites used in this study results from shallow events. Stars indicate reference station.

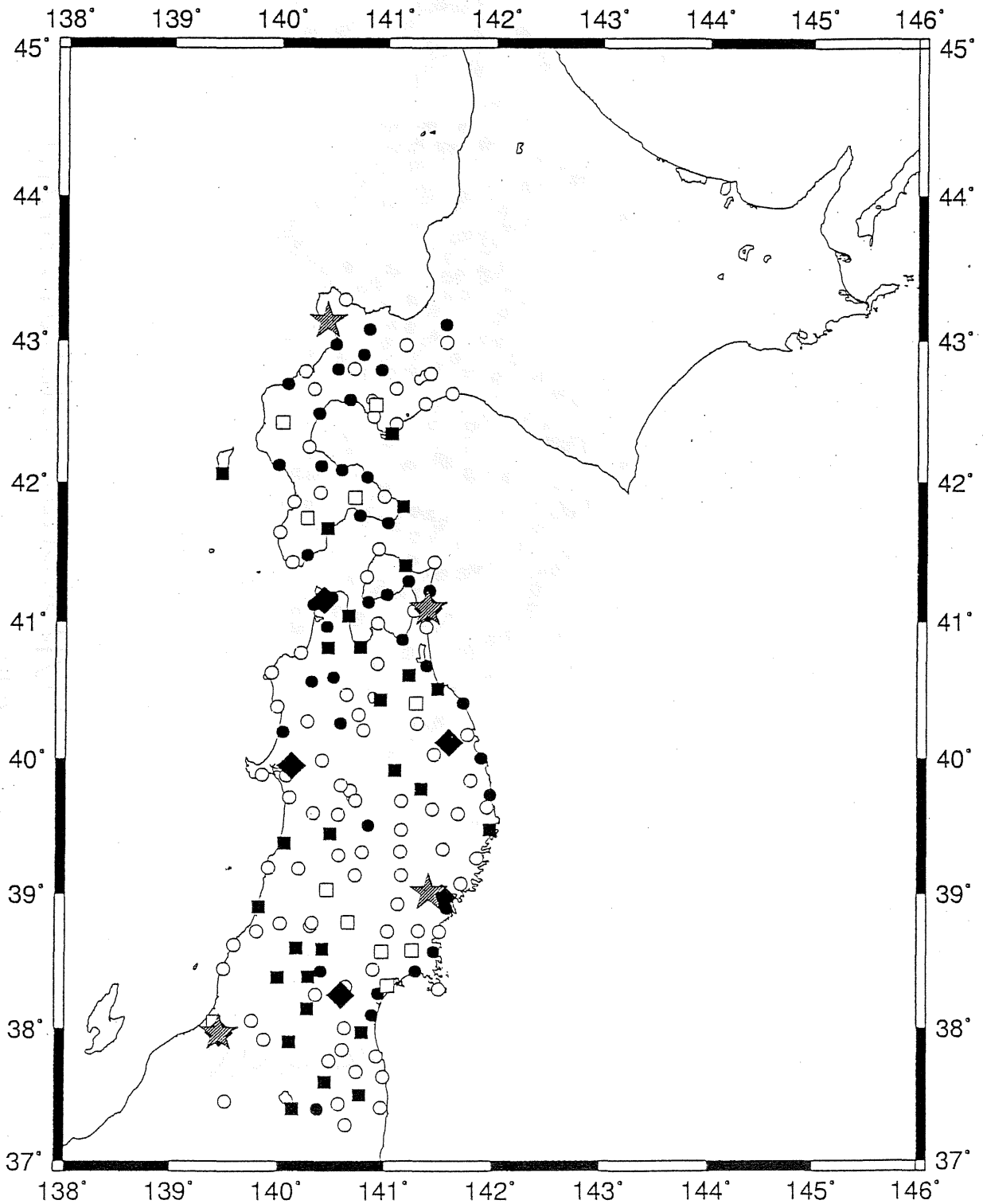


Figure 7 b)

Map of the predominant frequency of ground motions at sites used in this study results from intermediate-depth events.

Stars indicate reference station.

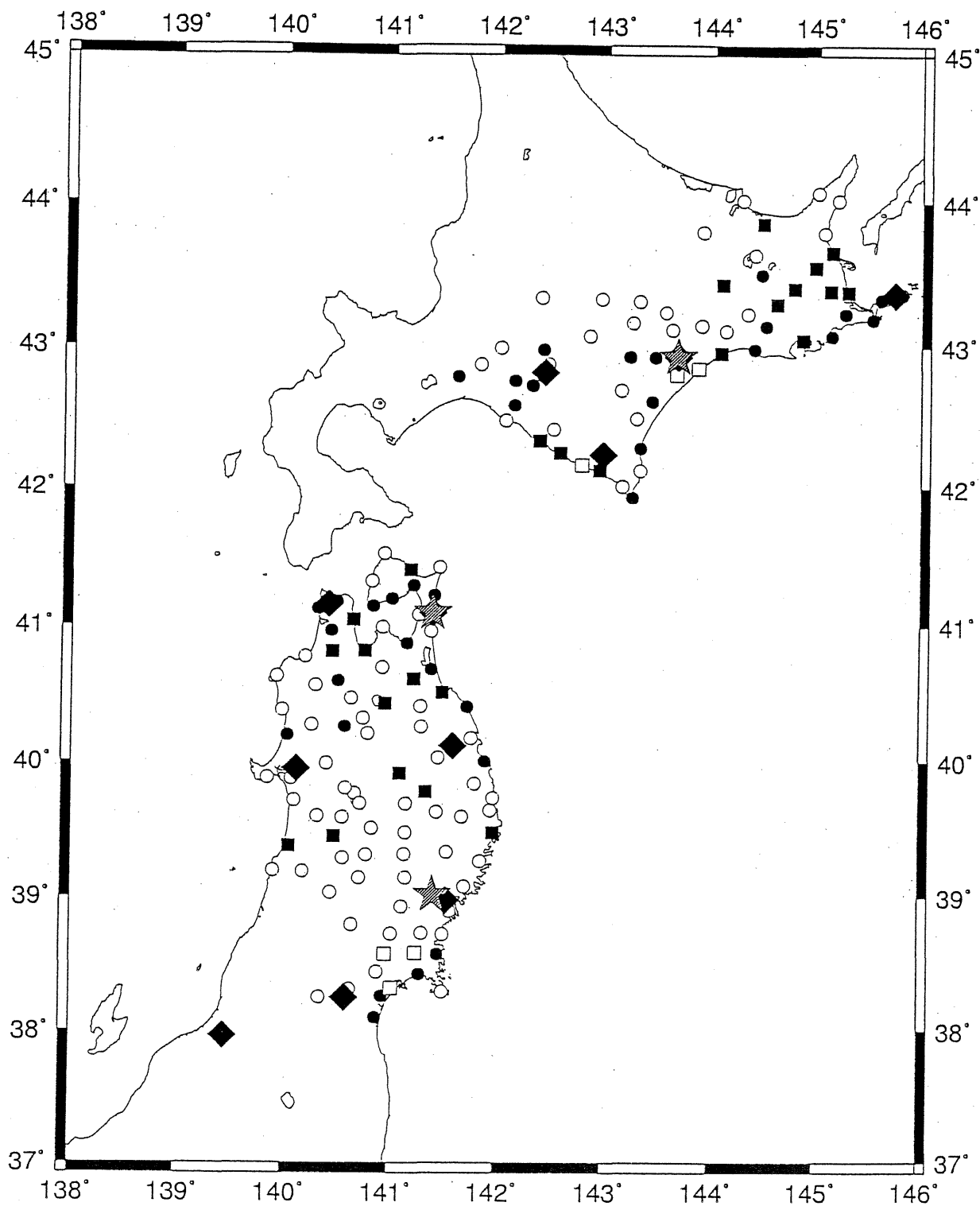


Table 3

Classification of station groups by site response.

Shallow events

Group	predominant frequency (Hz)	RMS
1	$f > 5.0$	0.382
2	$2.5 < f < 5.0$	0.393
3	$1.5 < f < 2.5$	0.443
4	$f < 1.5$	0.524

Intermediate-depth events

Group	predominant frequency (Hz)	RMS
1	$f > 5.0$	0.399
2	$2.5 < f < 5.0$	0.435
3	$1.5 < f < 2.5$	0.406
4	$f < 1.5$	0.468

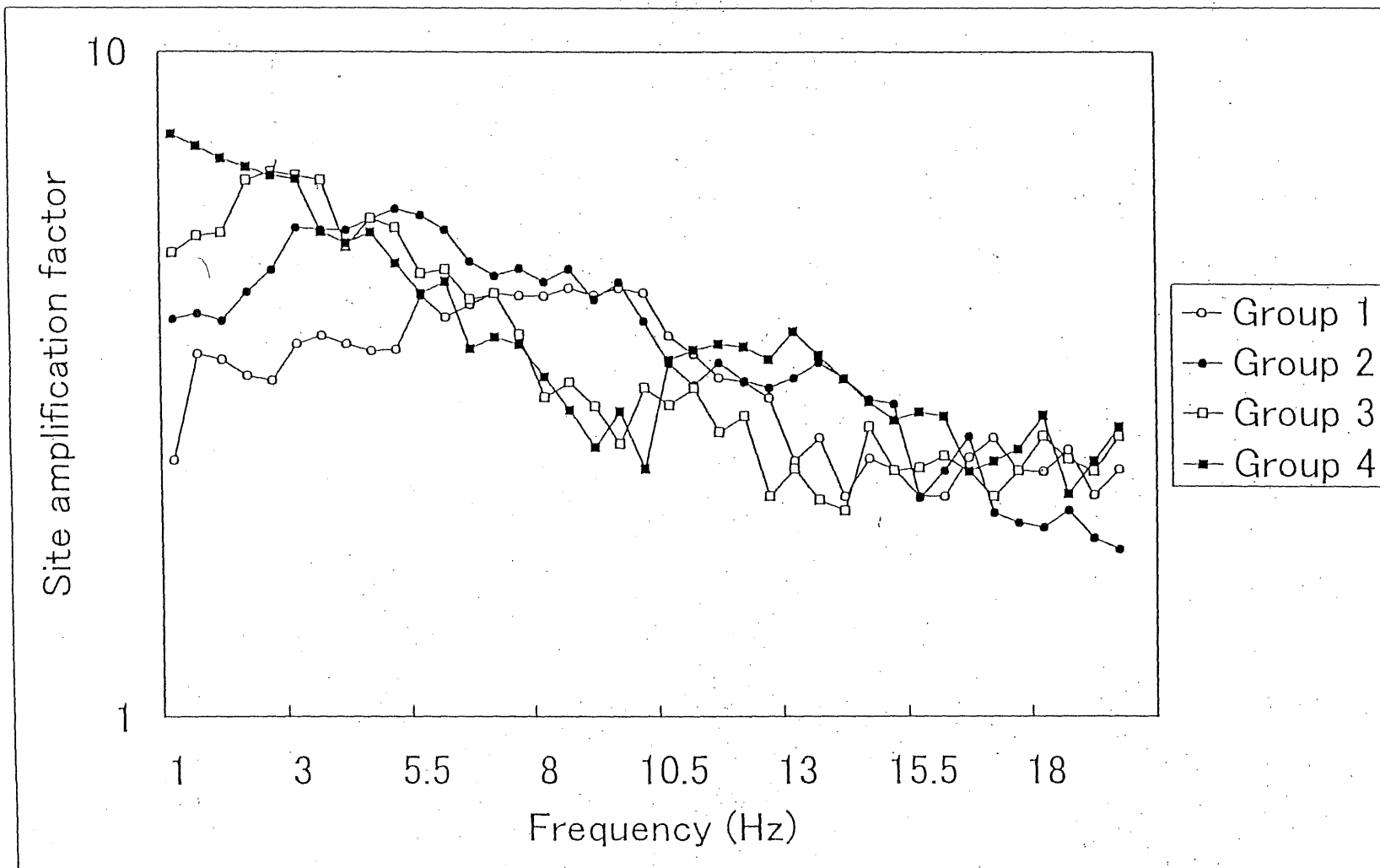


Figure 8 b)

Average site amplification factor results from intermediate-depth events.

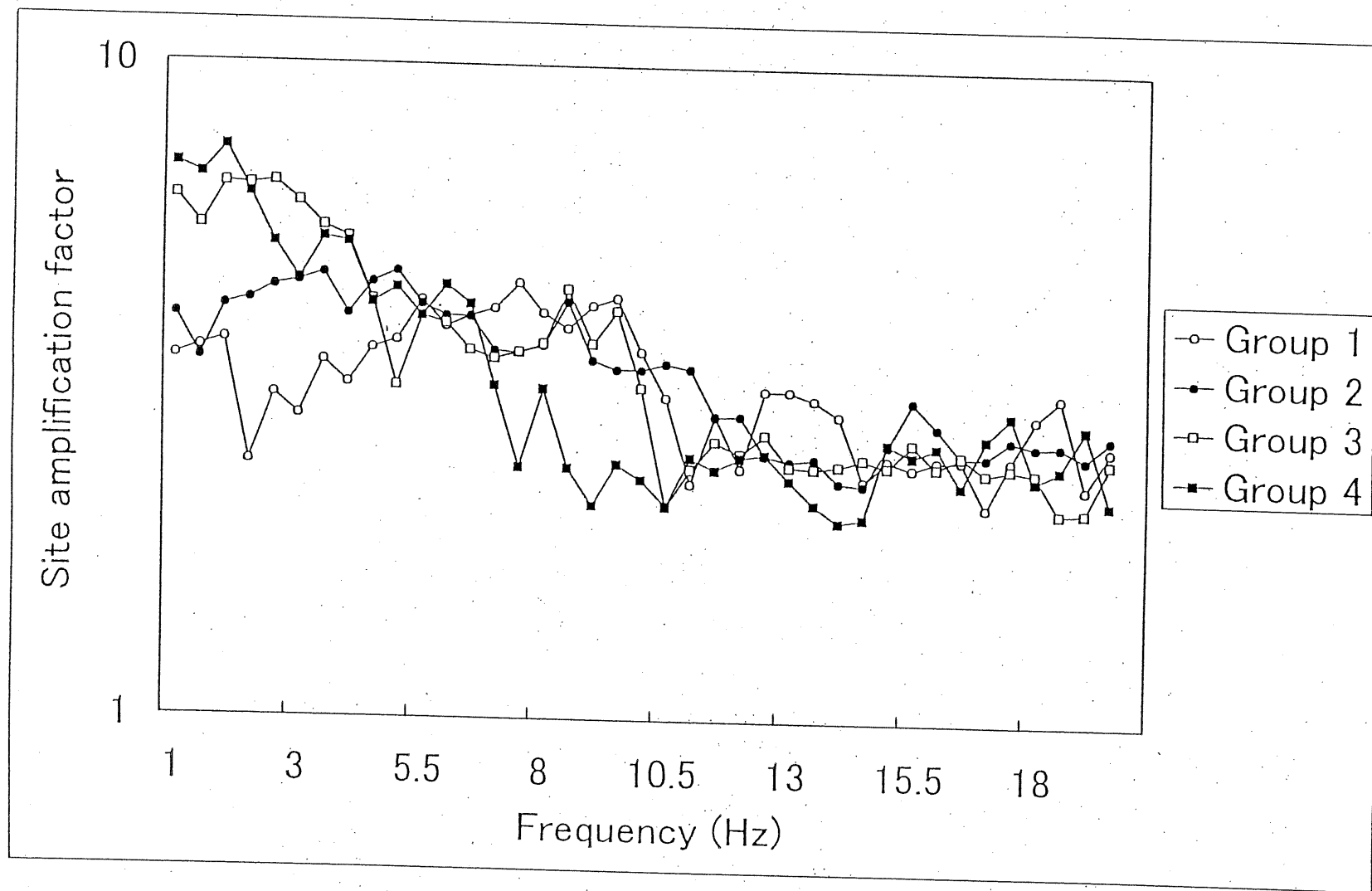


Figure 8 a)

Average site amplification factor results from shallow events.

wide range incident angles compared with deep events.

The site responses can be divided into 4 groups by the predominant frequency. Table 3, Figures 8a and 8b show the classification of groups and average site amplification for each group. Because near-surface structure and S-wave velocity beneath station were known *a priori*, it can be examined whether stations in a group have common sub-surface structures. Comparing site responses with these structures, some consistent results were obtained. Group 1, which have small amplitudes at high frequency are located harder sites (average S-wave velocity is above 500 m/s) and Group 2 and Group 3 which have larger site amplifications are located on softer sites (average S-wave velocity below 500m/s). This consistency implies that the estimation is appropriate for the site amplification.

Estimates of radiated seismic energy

Figures 9a and 9b shows plots of radiated seismic energy as a function of seismic moment for shallow and intermediate-depth earthquakes, respectively, Seismic moments were obtained from the mechanism solution from the Freesia network. For those events where moments were not available from Freesia, seismic moments were calculated based on the empirical relationship between moment and JMA magnitude (Takemura, 1990).

$$\log Mo = 1.5(M_{JMA} - 0.2) + 16.2 \quad (13)$$

Solid lines indicate apparent stress $\Delta\sigma_{app}$ (Wyss and Brune, 1968) for 0.03MPa, 0.3MPa, 3MPa, 30MPa.

$$\sigma_{app} = \mu E_s / Mo \quad (14)$$

where μ is the rigidity assumed to be 0.3×10^{11} Pa (Kikuchi and Fukao, 1988) and 0.68×10^{11} Pa for shallow and intermediate-depth events, respectively.

Comparing Figures 9a and 9b, it can be seen that compared to shallow earthquakes, intermediate-depth earthquakes have a larger E_s for the smaller moments. This means intermediate-depth events excite larger amplitude waves than shallow events at higher frequencies. There is a difference of about a factor of 5 between these events. At larger moments this difference tends to become smaller.

Figures 10a and 10b show comparisons with other studies. These results, for shallow events which were calculated in this study have almost the same radiated energy.

Also, these results show that intermediate-depth events have a constant E_s/M_0 ratio over a large moment range. This is different from shallow events which show an increase in E_s/M_0 as a function of moment. It means deep events have constant apparent stress. For shallow events, E_s/M_0 is different between large and small events by about a factor of 100 (Kanamori *et al.* 1993). Although there are only a small number of data, average E_s for the shallow events were about a factor of 5 larger than for intermediate-depth events at large moments. This study shows there are differences in the source scaling between shallow and intermediate-depth earthquakes.

Estimates for E_s are affected by attenuation and site effects. In this study corrective filters were obtained for these two effects. After correction of path effects, there is no strong trend of the energy estimates with distance. Furthermore for the site amplifications obtained, there are some correlation between predominant frequency and sub-surface structure beneath station. These results imply that these two filters were estimated appropriately. However there is still a large scatter in the energy estimates of the earthquakes studied. There may be several reasons for errors in the source parameters. For example, inadequate separation of the source and propagation or uncertainty of estimates of M_0 . Moments of small shallow events which occurred before 1997 were often not determined, so I used an empirical relation, which could have some bias. However there is still a significant difference between the average E_s between shallow and intermediate-depth events.

Discussion

In this study differences of E_s between shallow and intermediate-depth events were obtained. Intermediate-depth earthquake appear to have constant E_s/M_0 . This implies that the rupture processes of deep events have no significant difference over a wide moment range. On the other hand, for large shallow events it can be considered that the slip velocity of shallow earthquake may become faster because of mechanisms such as fault lubrication or fault melting. Ma *et al.* (2000) studied the 1999 Chi-Chi, Taiwan earthquake ($M_w 7.7$), and found differences of ground motion between the rupture of the northern and southern partitions of the fault. They suggested the reason for the large slip velocity observed in north is a result of fault lubrication; the fault zone contains viscous

Figure 9 a). Plots of radiated seismic energy as a function of seismic moment for shallow events .

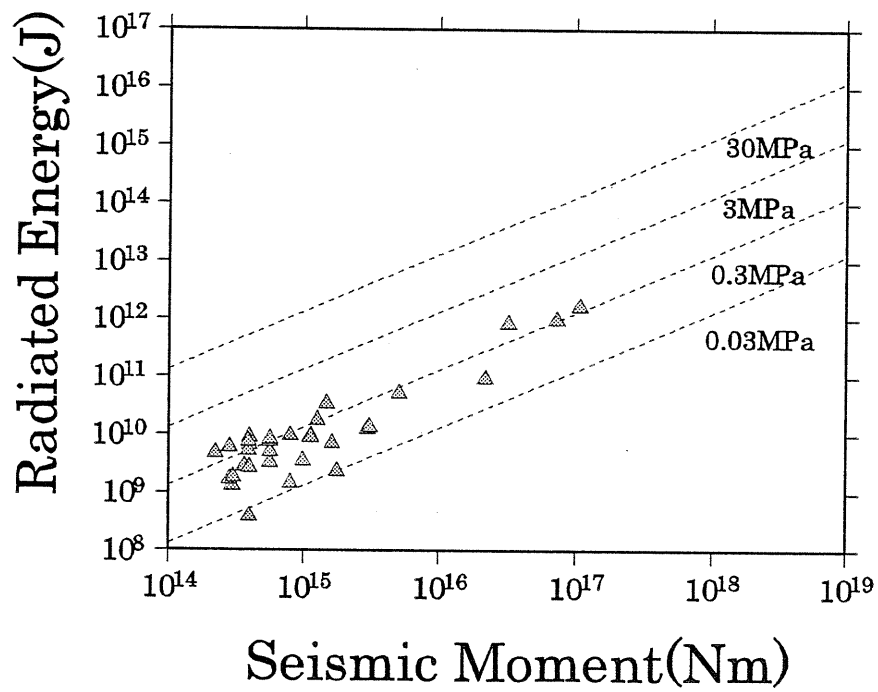


Figure 9 b). Plots of radiated seismic energy as a function of seismic moment for intermediate-depth events .

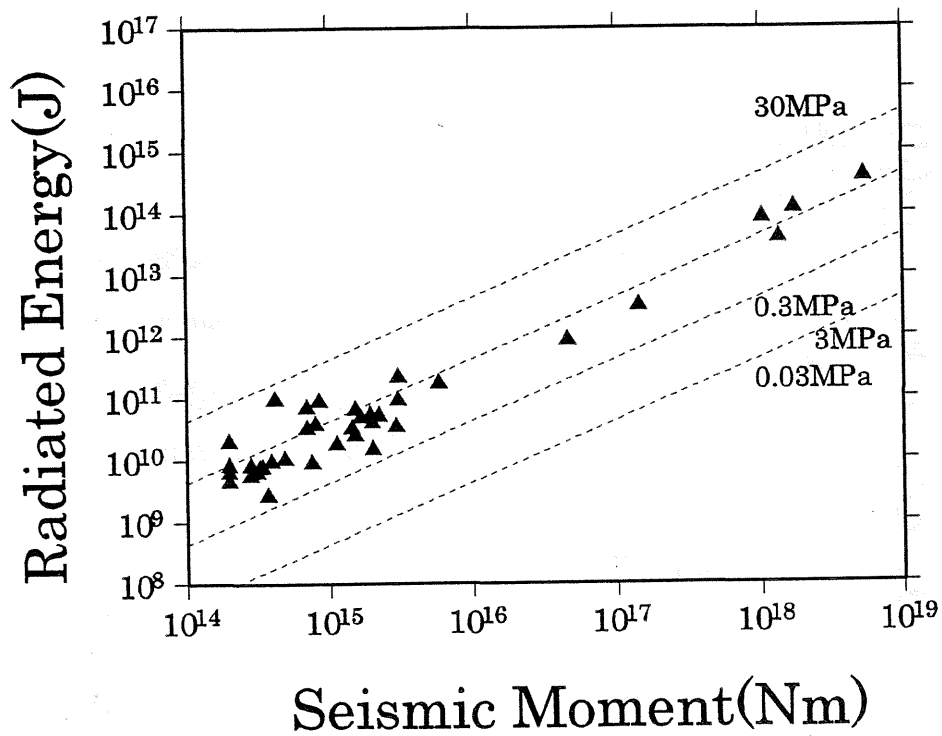


Figure 10 b)

Comparison of radiated energies with other studies for intermediate-depth earthquakes.

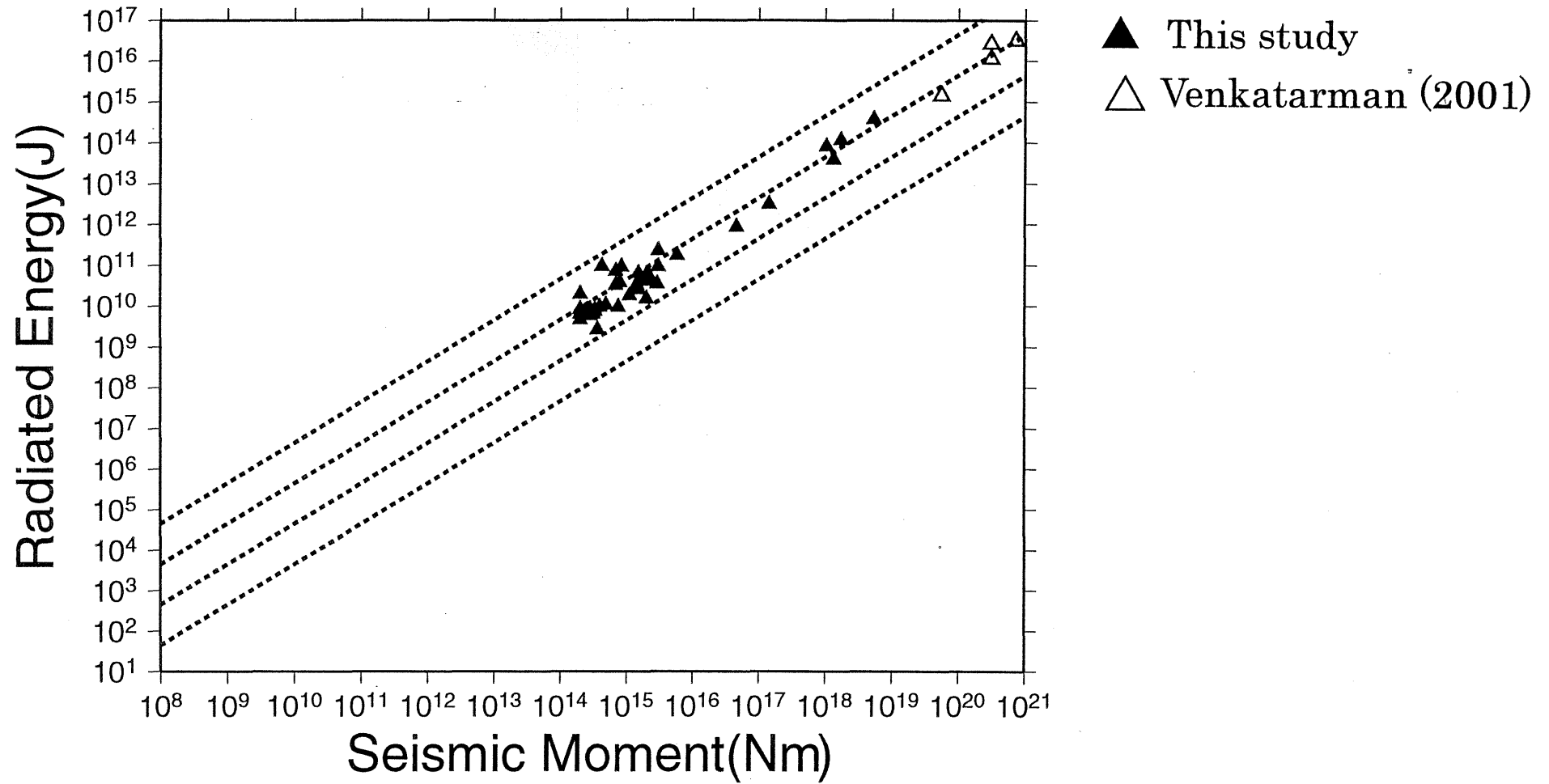
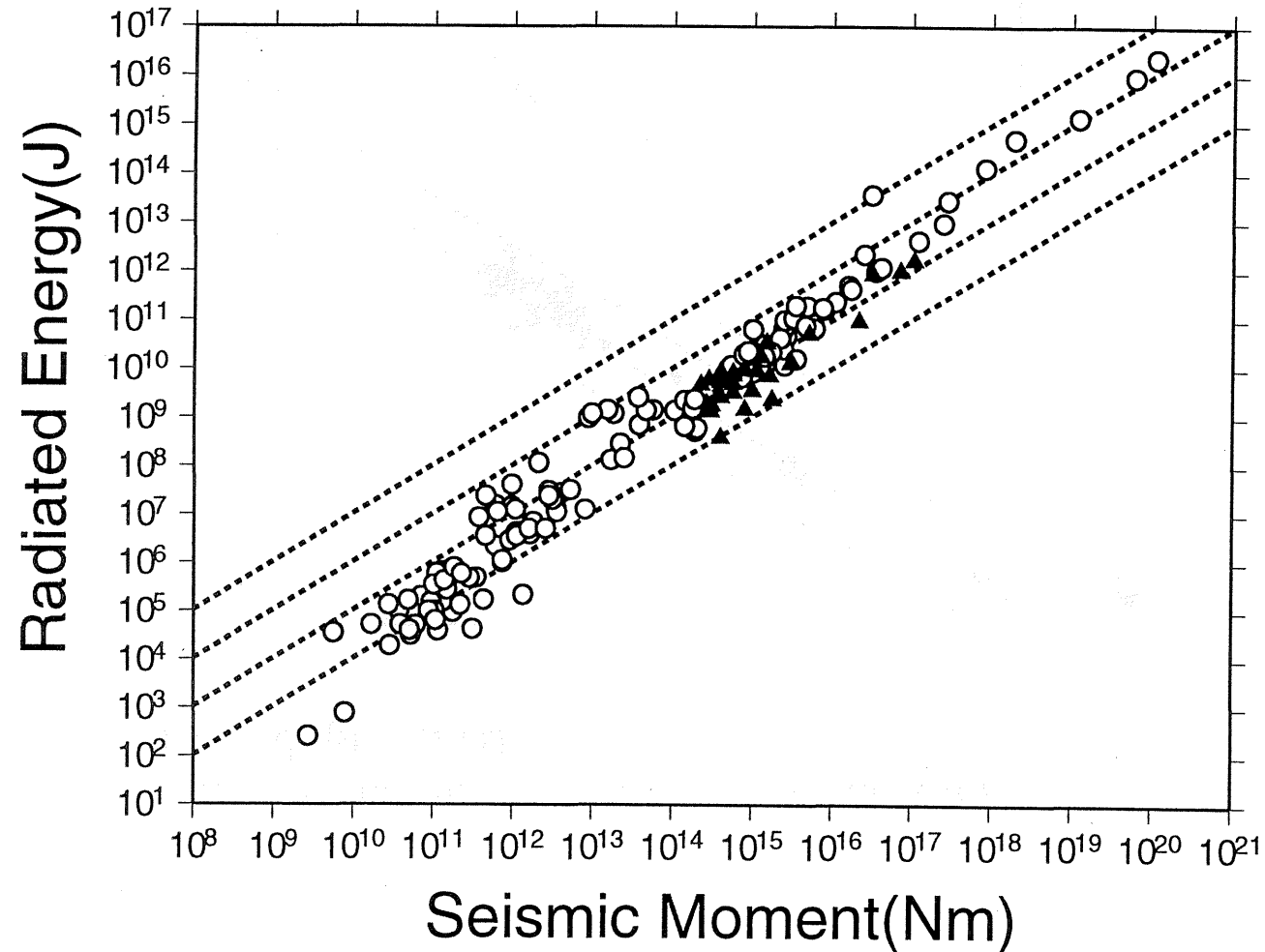


Figure 10 a)

Comparison of radiated energies with other studies
for shallow earthquakes.

▲ This study

○ Southern California, Kanamori et al. (1993), Cajon Pass Borehole, Abercrombie (1995)
Northridge aftershocks, Mori et al. (2001), Long Valley Borehole, Prejean and Ellsworth (2001)



material (e.g. gouge), which lead to increases of pore pressure and reduction of the area of contact during large slips. This may be associated with the pressure and thermal state. Similarly, Kanamori and Heaton (2000) proposed the reason for reduction of friction in the fault zone is that the rupture process for large events involve frictional melting. They suggested that fluid which is produced from frictional melting reduces friction and increases slip velocity. These mechanisms are consistent with past studies for E_s/M_o which show large earthquakes have E_s/M_o about 100times larger than small events (Kanamori *et al.*, 1993). This results means there are differences in the rupture process between small and large events for shallow earthquakes.

The two mechanisms for reducing friction occur at relatively low pressure states, therefore it is doubtful whether deep events can have the same type of increases slip velocity. Of course, fault melting may occur for deep focus earthquake because of the high pressure. The pressure at depths of 100km is 3.1Gpa (Bullen, 1963), which can be considered so high that the effects of dynamic faulting do not affect the friction.

Our results show that the apparent stress is almost the same for both shallow and intermediate-depth events for large moments. Apparent stress is defined as the product of the seismic efficiency factor η and the average shear stress σ on the fault. η is expressed as

$$\eta = E_s / E_{tot} \quad (15)$$

where E_{tot} is the total strain energy which is released during faulting. As mentioned before, it is impossible to obtain absolute values of the total energy by seismological method, so it is difficult to calculate η . However an upper bound of η can be estimated from the ratio of the apparent stress to estimates of the stress drop, $\Delta\sigma$ (Wyss, 1970)

$$\eta_{max} = 2\sigma_{app} / \Delta\sigma \quad (16)$$

Several different investigators find that stress drops of intermediate-depth earthquakes are somewhat higher than for shallow events (e.g. Wyss and Molnar, 1972; Kikuchi and Fukao, 1987). Sasatani (1980) and Mikumo (1971) studied stress drops for deep and intermediate-depth earthquakes and pointed out that stress drop increases with depth. Combining this with results of our study, for large moments ($M_o > 1 \times 10^{17} \text{Nm}$) indicates that the seismic efficiency is lower for deeper events compared to shallow events. A lower seismic efficiency is equivalent to saying that there is a greater rate of energy dissipation at the source.

Conclusions

An important result obtained in this study is that intermediate-depth events have a nearly constant E_s/M_0 ratio. This is different from shallow events which have been studied previously. Changes in frictions may cause the larger radiated energies for large shallow earthquakes. Because of the higher pressure state of deep earthquakes, these types of mechanism probably cannot occur for deep earthquakes. Since the deeper earthquakes radiate less energy, this means the seismic efficiency is smaller, compared to shallow earthquakes. This idea is consistent with our observations that the apparent stresses for shallow and deep earthquakes are about the same, but the static stress drop of deep earthquakes is higher. Lower seismic efficiency for deep earthquakes indicates the possibly proportionately more energy goes into heat or fracture formation.

Acknowledgement

We thank the National Research Institute for Earth Sciences and Disaster Prevention for providing digital waveform data.

References

- Boatwright, J. and G. L. Choy, Teleseismic estimates of the energy radiated by shallow earthquakes, in U. S. Geol. Surv. Open-File Rept. 85-0290-A, Workshop XXVIII on the Borah peak, Idaho earthquake, R. S. Stein, R. C. Bucknam, and M. L. Jacobson (Editors), 409-448, 1985.
- Boore, D. M. and J. Boatwright, Average body wave radiation coefficient, *Bull. Seism. Soc. Am.* 72, 1049-1068, 1984.
- Bullen, An Introduction to the Theory of seismology, 3rd Ed., Cambridge Univ. Press. 109-121, 1963.
- Gutenberg, B and C. F. Richer, Earthquake magnitude, intensity, energy, and acceleration, 1, *Bull. Seism. Soc. Am.* 32, 163-191, 1942.

- Gutenberg, B and C. F. Richer, Earthquake magnitude, intensity, energy, and acceleration, 1, Bull. Seism. Soc. Am. 46, 105-145, 1956a.
- Gutenberg, B and C. F. Richer, Magnitude and energy of earthquakes, Ann. Geofis. Rome 9, 1-15, 1956b.
- Haskell, N., Total energy and energy spectral density of elastic wave radiation from propagating faults, Bull. Seism. Soc. Am. 56, 1811-1842, 1964.
- Ito, K., Regional variations of the cutoff depth of seismicity in the crust and their relation to heat flow and large inland-earthquake, J. Phys. Earth. 38, 223-250, 1990.
- Kamiya, S., T. Miyatake and K. Hirahara, Three-dimensional P-wave velocity structure beneath the Japanese Islands, Bulletin of the Earthquake Research Institute. 64:4, 457-485, 1989.
- Kanamori, H., J. Mori, E. Hauksson, T. Heaton, L. Hutton, and L. Jones, Determination of earthquake energy release and M_L using Terrascope, Bull. Seism. Soc. Am. 83, 330-346 1993.
- Kanamori, H. and T.H. Heaton, Microscopic and macroscopic physics of earthquakes, Report U. S. Geological Survey. 1-41 2000.
- Karato, S., Rheology and Earth science, Tokyo, Japan: Tokyo Univ. Press, 2000.
- Kikuchi, M. and Y. Fukao, Inversion of long-period P-waves from great earthquakes along subduction zones, Tectonophysics, 144, 231-247, 1987.
- Kikuchi, M. and Y. Fukao, Seismic wave energy inferred from long-period body wave inversion, Bull. Seism. Soc. Am. 78, 1707-1724, 1988.
- Kinoshita, S, Evaluation of site factor and propagation characteristics by means of earthquake observation, Jisin, 46, 161-170, 1993.
- Liu, H. L. and D. V. Helmberger, The 23.19 aftershock of the 15 October 1979 Imperial Valley earthquake; more evidence for an asperity. Bull. Seism. Soc. Am. 75, 689-708, 1985.
- Ma, K., J. Mori and S. Yu, Rupture behavior analysis of the 1999 Chi-Chi, Taiwan, earthquake from teleseismic, strong motion and GPS, World Chinese Conference on Geological Sciences. 2, A36-A38, 2000.
- Matsuzawa, T., A. Hasegawa, A. Takagi, Q_p structure beneath the northeastern Japan Arc estimated from twofold spectral ratio method, Tohoku Geophysical Journal, 32, 21-33, 1989.
- Mikumo, T., Source process of deep and intermediate earthquakes as inferred from long-period P and S waveforms, Part 2, J. Phys. Earth, 19, 303-320, 1971.
- Nakamura, R. and T. Uetake, Three dimensional attenuation structure and site

- amplification inversion by using a large quantity of seismic strong motion records in Japan, paper presented at 12th World Conference on Earthquake Engineering, Auckland, New Zealand, ID 0724, 2000.
- Sasatani, Source parameters and rupture mechanism of deep-focus earthquakes, *J. Fac. Sci. Hokkaido Univ.*, ser 7, *Geophys.*, 6, 301-384, 1980.
- Satoh, T., H. Kawase and T. Sato, Statistical spectral model of earthquakes in the eastern Tohoku district, Japan, based on the surface and borehole records observed in Sendai, *Bull. Seism. Soc. Am*, 87, 446-462, 1997.
- Satoh, T., H. Kawase and S. Matushima, Source spectra, attenuation function, and site amplification factors estimated from the K-NET records for the earthquakes in the border of Akita and Miyagi prefectures in August, 1996, *Jisin*, 50, 415-429, 1998.
- Scholz, C.H., *The Mechanics of Earthquakes and Faulting*. Cambridge, UK: Cambridge Univ. Press, 1990.
- Seno, T. (2001). Double seismic zone and dehydration embrittlement (abstract), *EOS, Trans. Am. Geophys. Union* 82, 908, 2001
- Vassiliou, M. S. and H. Kanamori, The energy release in earthquakes, *Bull. Seism. Soc. Am.* 72, 371-387, 1982.
- Venkataraman. A., Rupture dynamics of subduction zone earthquakes in list of energy-to-moment ratios, (abstract), *EOS, Trans. Am. Geophys. Union* 82, 1267.
- Wadati, K., Existence and study of deep earthquakes, *J. Meteorol. Soc. Jpn. Ser.2*, 5, 119-145, 1927.
- Wyss, M. and J. N. Burune (1968). Seismic moment, stress, and source dimensions for earthquakes in California-Nevada region, *J. Geophys. Res.*, 73, 4681-4694.
- Wyss, M., Stress estimates for South American shallow and deep earthquakes, *J. Geophys. Res.*, 75, 1529-1544, 1970.
- Wyss, M. and P. Molnar, Source parameters of intermediate and deep focus earthquakes in the Tonga arc, *Phys. Earth Planet. Inter.*, 6, 279-292, 1972.

Stress Drops and Radiated Energies of Aftershocks of the 1994 Northridge, California Earthquake

Jim Mori, Disaster Prevention Research Institute,
Kyoto University, Kyoto, JAPAN

Rachel E. Abercrombie, Department of Earth and Planetary Sciences,
Boston University, Boston MA, USA

Abstract

We study stress levels and radiated energy to infer the rupture characteristics and scaling relationships of aftershocks and other southern California earthquakes. We use empirical Green functions to obtain source time functions for 47 of the larger ($M \geq 4.0$) aftershocks of the 1994 Northridge, California earthquake ($M6.7$). We estimate static and dynamic stress drops from the source time functions, and compare them to well-calibrated estimates of the radiated energy. Our measurements of radiated energy are relatively low compared to the static stress drops, indicating that the static and dynamic stress drops are of similar magnitude. This is confirmed by our direct estimates of the dynamic stress drops. We infer that these earthquakes have nearly complete stress drops and that the absolute level of crustal driving stress is in the range of a few to several tens of MPa. Combining our results for the Northridge aftershocks with data from other southern California earthquakes shows an increase in the ratio of radiated energy to moment, with increasing moment. There is no corresponding increase in the static stress drop. This systematic change in earthquake scaling from smaller to larger ($M3$ to $M7$) earthquakes suggests differences in rupture properties that may be attributed to differences of dynamic friction on the faults.

Introduction

We investigate the relationship between stress drops (static and dynamic) and radiated energy using well-determined source parameters for a set of Northridge aftershocks and

other southern California earthquakes. The 1994 Northridge Earthquake (M_w 6.7) was a large damaging event in southern California (U.S. Geological Survey, 1996), and the well-recorded mainshock and aftershock sequence has been the focus of numerous seismological and engineering studies (e.g., CURee, 1998). Estimates of the radiated energy and stress drop provide information about the mechanics of earthquake ruptures and help distinguish between models that describe the tectonic and frictional stress levels before, during, and after the earthquake (e.g. models described in Lachenbruch and Sass [1980] and Kikuchi and Fukao, [1988]). Although earthquake stress drops reflect only the relative changes in stress, we can use our results to make inferences about the absolute levels of tectonic stress. *Lachenbruch and Sass [1980]* used radiated seismic energies to infer low stress levels (< 20 MPa) on the San Andreas fault. In a similar way, we determine estimates of the radiated energy and use them to infer the tectonic stress level for the southern California region. We discuss our observations of radiated energy and stress drop in the context of simple models that describe the stress and friction conditions during the earthquake.

We also investigate how source parameters vary as a function of earthquake size. Recent observations have suggested that as earthquakes increase in magnitude they radiate an increasingly larger proportion of energy [*Kanamori et al., 1993, Abercrombie, 1995, Mayeda and Walter, 1996*] which implies differences from standard constant stress drop models [e.g. *Aki, 1967, Kanamori and Anderson, 1975*]. Small (M_L 1 to 5) earthquakes recorded at Cajon Pass borehole show a relative increase of radiated energy with magnitude without a corresponding increase in static stress drop [*Abercrombie and Leary, 1993, Abercrombie, 1995*]. This study looks at larger magnitude ($M4-5$) events to investigate if the same trend exists. Systematic changes in the relative amounts of energy radiated as a function of event size could indicate important differences in the rupture dynamics of small and large earthquakes [*Kanamori, 1998*].

Using well-resolved source time functions derived from empirical Green function deconvolutions, we obtain reliable estimates stress drops and radiated energy. We then investigate the relationships between these source parameters to provide constraints on the stresses driving the earthquakes and source scaling for $M4$ to $M7$ earthquakes.

Data and Method

Earthquake source parameter studies are always complicated by difficulties in separating source and propagation effects in the waveforms. This problem is somewhat simplified for larger earthquakes ($M > 4$) recorded at distances of less than 50 km since there are usually clear body wave arrivals and wave propagation effects, such as attenuation and multiple arrivals, are less dominant at the relevant frequencies. Large aftershock sequences that are recorded with modern instrumentation provide the opportunity to study a significant number of such earthquakes. This was the case following the 1994 Northridge earthquake ($M 6.7$) when an active aftershock sequence with numerous larger events was recorded by high-quality permanent and portable stations in southern California.

We examine all the aftershocks with magnitude greater or equal to M_L 4.0 from January 1994 to May 1995, and select the earthquakes that had clean P -wave arrivals for which we can obtain clear Green function deconvolutions. We have to discard earthquakes mainly because the P -wave arrival is contaminated by other events. This is particularly true for the first day following the mainshock when aftershocks were occurring at a high rate. This left 47 of the larger ($M \geq 4.0$) Northridge aftershocks (Table 1) for our estimates of source parameters. These earthquakes were recorded on broadband TERRAscope [Kanamori *et al.*, 1991] stations and the temporary station LA00 operated by Univ. of California, Santa Barbara (Figure 1). We use hypocenters determined with a three-dimensional velocity model which improves the depth determinations [Mori *et al.*, 1995]. Focal mechanisms and seismic moments were determined by Thio and Kanamori [1996] using regional surface waves. All data in this study are obtained from the Southern California Earthquake Center Data Center.

Empirical Green Functions

We use empirical Green function deconvolutions to remove path and site effects from the P waveforms [e.g. Mueller, 1985, Mori and Frankel, 1990] and extract source time functions. The waveform of a small earthquake is used as an empirical Green function to remove the path and site effects from the waveform of a larger target earthquake. This results in a waveform corresponding to the far-field source time function of the target earthquake. One of the important aspects of this method is choosing an appropriate small earthquake for use as the empirical Green function. We examine a

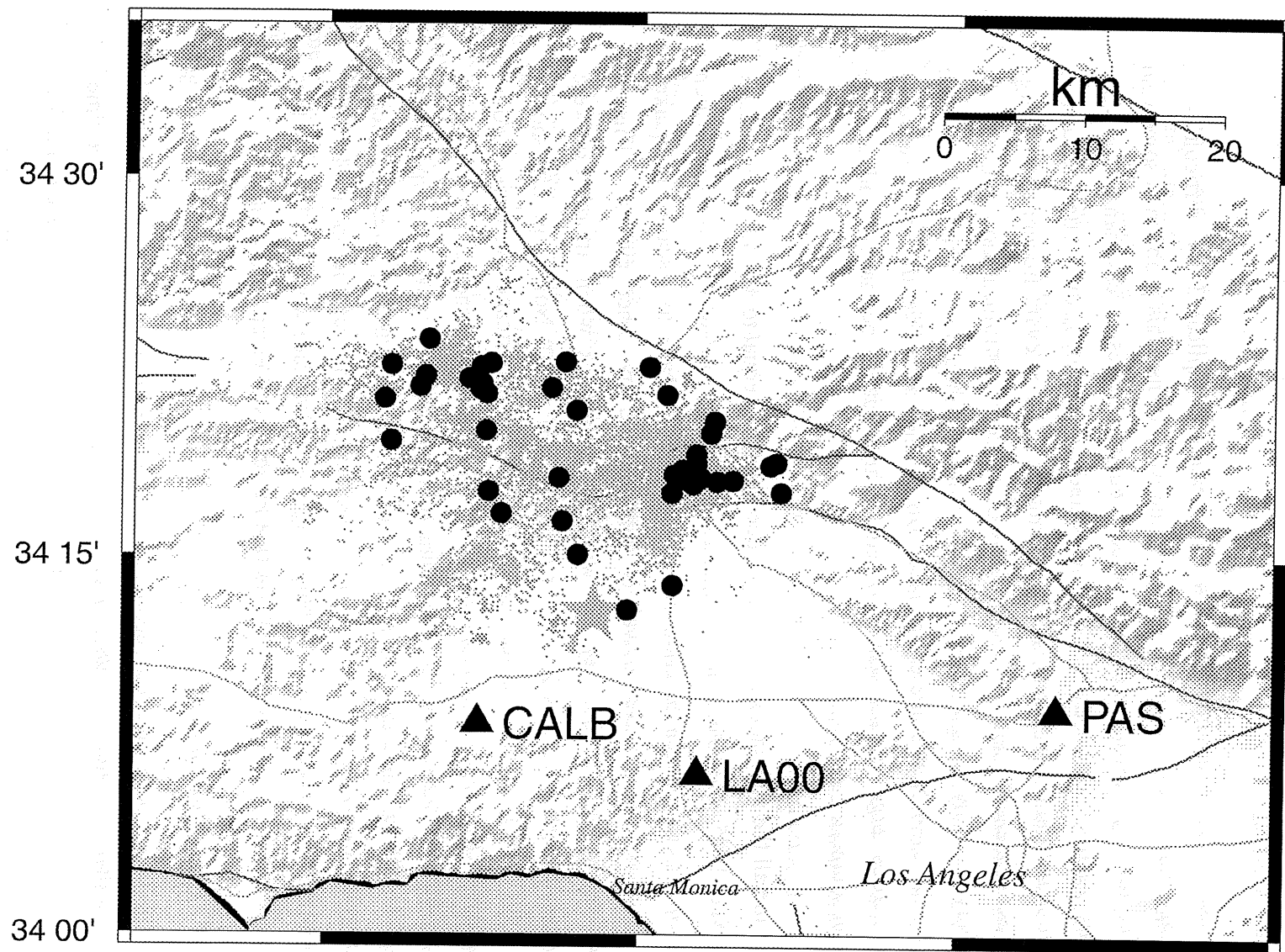


Figure 1. Map showing locations of Northridge aftershocks (solid circles) and stations (triangles) used in this study. Gray star and small dots show locations of Northridge mainshock and distribution of smaller aftershocks, respectively.

large number of small earthquakes to find a good empirical Green function and try deconvolutions using all small events within an epicentral radius of 2 km and with magnitudes larger than $M1.5$ and at least 1.5 units smaller than the target earthquake. We do not limit the depth range because of possible uncertainties in the depth determinations for these small earthquakes. Within the Northridge aftershock zone, this search pattern usually yielded several tens to several hundreds of potential empirical Green function events.

Figure 2 shows a typical range of waveforms that are obtained for the deconvolutions using 37 different small earthquakes. This subset of 37 events includes all the $M2.0$ and greater earthquakes located in 1994 within a epicentral radius of 2.0 km and with depths within 2.0 km of target earthquake (CUSP ID 3143547). The deconvolutions are ordered by inter-event epicentral distance between the Green function and target earthquakes. It is difficult to estimate accurately the resolution of the relative locations, but it is thought to be on the order of several hundred meters. For the smaller inter-event spacings the results are better but there are some deconvolutions at closer distances that do not work well and some deconvolutions at greater distances that produce good waveforms. The variation in the quality of the resultant source time functions in Figure 2 shows only a weak dependence on the inter-event distance, and suggests caution in using waveform similarities to infer relative locations of earthquakes. In addition to the close distances, similar focal mechanisms (which are usually unavailable for these small events) are probably important factors for choosing an appropriate empirical Green function. The choice of the Green function that is used in this study is a subjective judgement made by looking at the deconvolved waveforms. One positive aspect of this technique is that the empirical Green functions that result in clear deconvolved waveforms all give generally consistent results. The waveforms in Fig. 2 that have good signal to noise ratios (traces plotted with darker lines) show fairly similar shapes with comparable source durations. The deconvolution that is used for source parameter estimates has an inter-event spacing of 1.2 km.

All of the source time functions used in this study are shown in Figure 3. The amplitudes of the waveforms are adjusted so that the areas of the displacement pulse are proportional to the long-period moments.

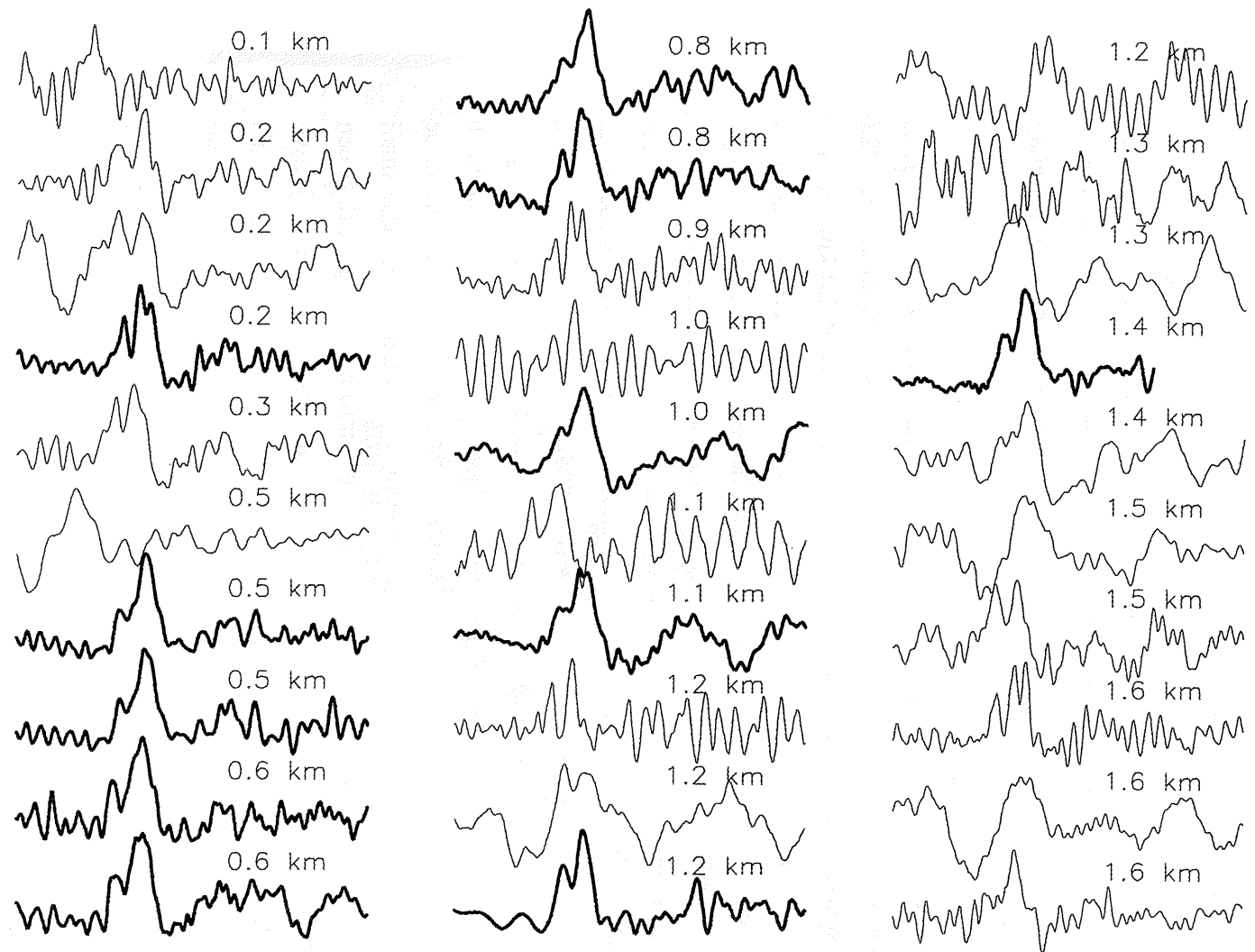


Figure 2. Deconvolutions for a subset of the small events that were tested as empirical Green functions for event 3143547 recorded at LA00. The number above each time series shows the inter-event distance. The traces plotted with heavier lines show deconvolutions with better signal to noise ratio. The asterisk (*) indicates the seismogram used for the source parameter estimate.

Table 1. Northridge aftershocks analyzed in this study.

Yr	Mo	Da	Time	Lat.	Long.	Mag.	Depth	ID
94	1	17	12 39 39.79	34.265	-118.540	4.9	13.2	3144652
94	1	17	12 54 33.74	34.307	-118.459	4.0	2.0	2150608
94	1	17	12 55 46.83	34.277	-118.578	4.1	6.0	3140674
94	1	17	13 6 28.34	34.251	-118.550	4.6	0.1	3140678
94	1	17	13 26 45.00	34.318	-118.456	4.7	6.0	3140684
94	1	17	13 56 2.48	34.293	-118.621	4.4	2.0	3140691
94	1	17	14 14 30.63	34.332	-118.445	4.5	2.8	3140870
94	1	17	15 7 3.17	34.304	-118.474	4.2	1.6	3140728
94	1	17	15 7 35.46	34.307	-118.467	4.1	1.0	2138698
94	1	17	15 54 10.76	34.376	-118.627	4.8	12.7	3140766
94	1	17	17 56 8.21	34.228	-118.573	4.6	19.2	3140853
94	1	17	19 35 34.30	34.311	-118.456	4.0	1.2	3140898
94	1	17	19 43 53.38	34.368	-118.637	4.1	11.4	3141205
94	1	17	20 46 2.40	34.302	-118.565	4.9	6.4	3141219
94	1	17	22 31 53.73	34.339	-118.442	4.1	0.1	3141242
94	1	17	23 33 30.69	34.326	-118.698	5.6	4.9	3141273
94	1	17	23 49 25.36	34.342	-118.665	4.0	8.2	3141062
94	1	18	0 43 8.89	34.376	-118.698	5.2	8.4	3141286
94	1	18	4 1 26.72	34.358	-118.623	4.3	0.5	3141180
94	1	18	7 23 56.02	34.333	-118.623	4.0	12.7	3141341
94	1	18	15 23 46.89	34.379	-118.561	4.8	7.1	3141597
94	1	19	4 40 48.00	34.361	-118.571	4.3	1.6	3142081
94	1	19	9 13 10.90	34.304	-118.737	4.1	13.0	3142087
94	1	19	14 9 14.83	34.215	-118.510	4.5	18.2	3142198
94	1	19	21 9 28.61	34.379	-118.712	5.1	14.4	3142595
94	1	19	21 11 44.90	34.378	-118.619	5.1	9.7	3142597
94	1	21	18 39 15.26	34.301	-118.466	4.5	9.7	3145627
94	1	21	18 39 47.08	34.297	-118.479	4.0	8.6	3159009
94	1	21	18 42 28.77	34.310	-118.475	4.2	8.8	3143541
94	1	21	18 52 44.23	34.302	-118.452	4.3	9.0	3143546
94	1	21	18 53 44.57	34.298	-118.459	4.3	8.8	3143547
94	1	23	8 55 8.66	34.300	-118.427	4.1	8.1	3144303

Yr	Mo	Da	Time	Lat.	Long.	Mag.	Depth	ID
94	1	24	4 15 18.82	34.347	-118.551	4.6	7.1	3145150
94	1	24	5 50 24.34	34.361	-118.628	4.3	9.4	3145168
94	1	24	5 54 21.07	34.364	-118.627	4.2	9.1	3145171
94	1	27	17 19 58.83	34.273	-118.563	4.6	13.4	3146628
94	1	28	20 9 53.43	34.375	-118.494	4.2	2.1	3146983
94	1	29	11 20 35.97	34.306	-118.579	5.1	1.1	3147406
94	1	29	12 16 56.35	34.278	-118.611	4.3	2.7	3147259
94	2	3	16 23 35.37	34.300	-118.440	4.0	8.8	3149105
94	2	6	13 19 27.02	34.292	-118.476	4.1	9.0	3150210
94	2	25	12 59 12.59	34.357	-118.480	4.0	2.3	3155150
94	3	20	21 20 12.26	34.231	-118.475	5.2	12.5	3159411
94	5	25	12 56 57.05	34.312	-118.393	4.4	8.5	3169078
94	6	15	5 59 48.63	34.311	-118.398	4.1	8.9	3172383
94	12	6	3 48 34.49	34.293	-118.389	4.5	9.5	3195727
95	6	26	8 40 28.94	34.394	-118.669	5.0	13.3	3217586

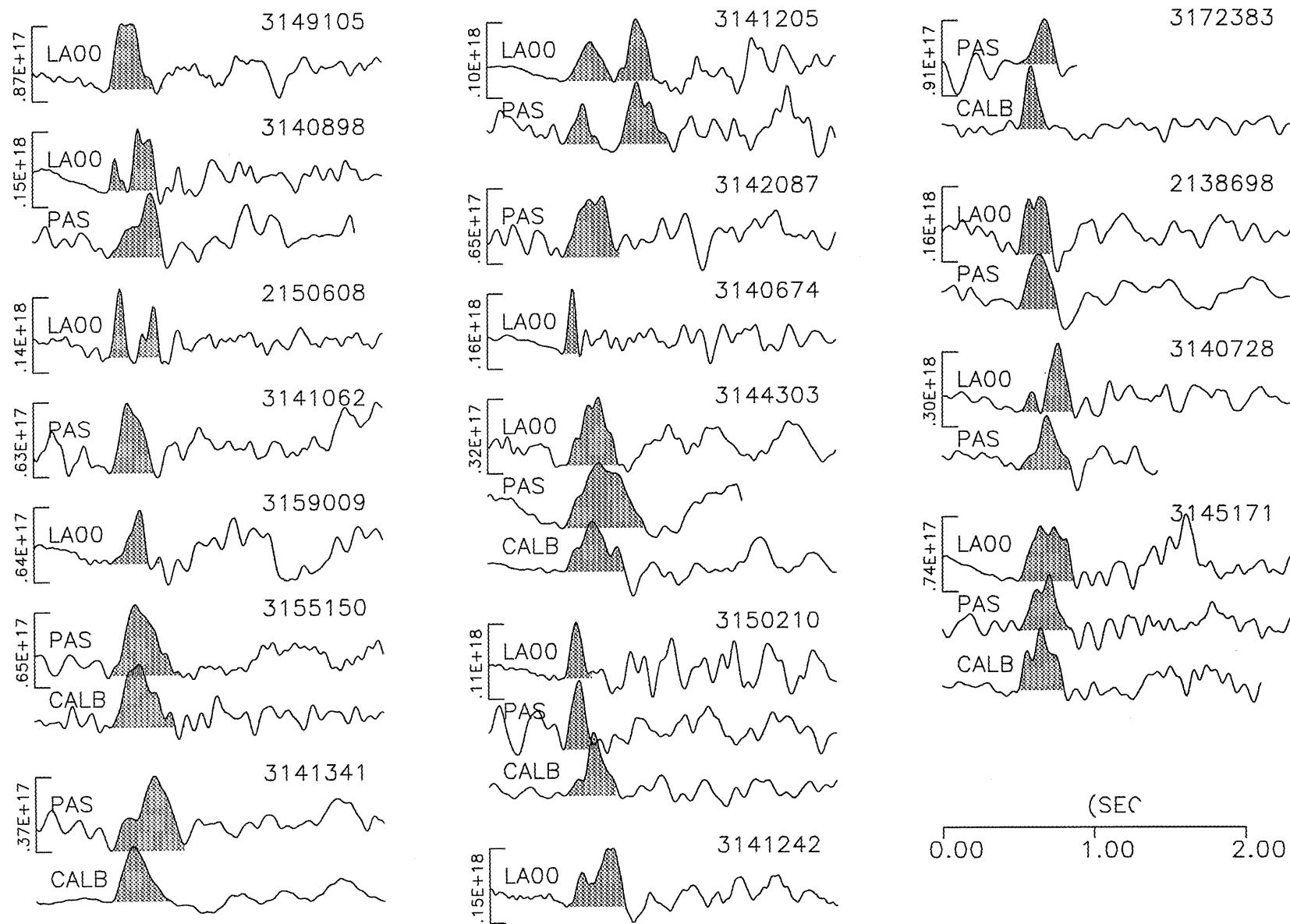
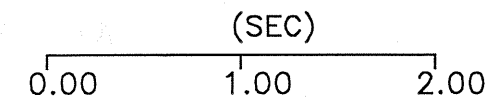
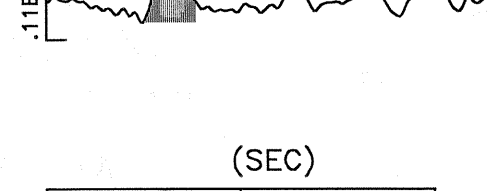
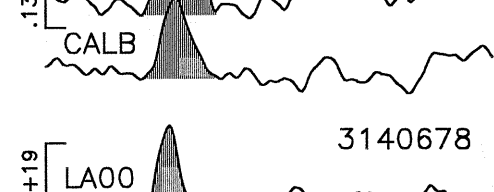
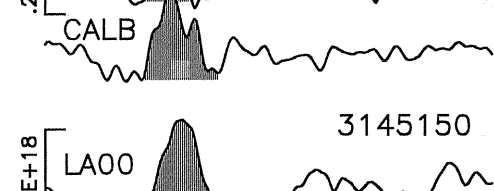
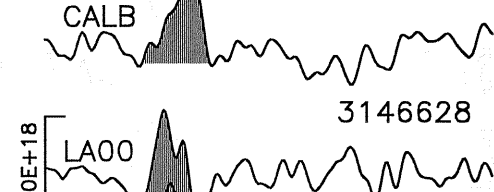
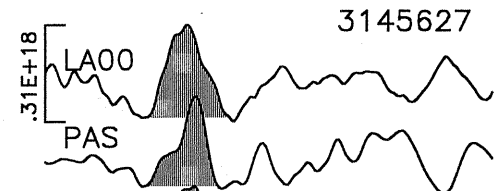
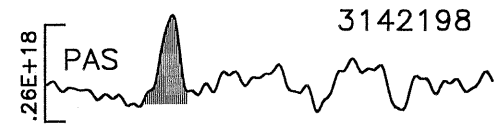
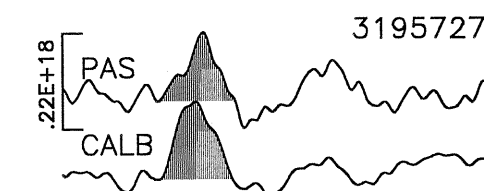
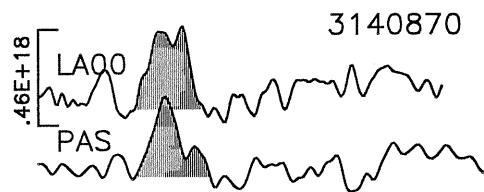
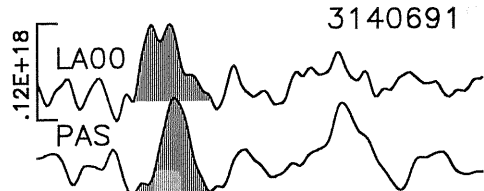
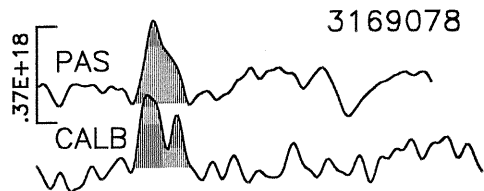
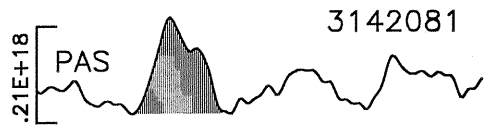
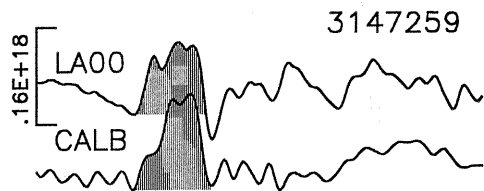
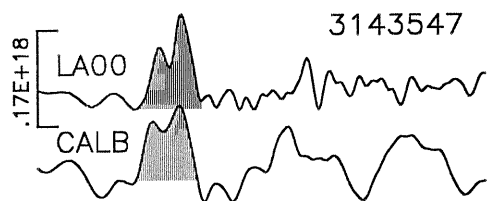
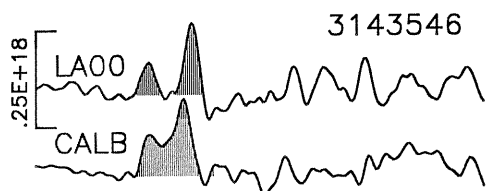
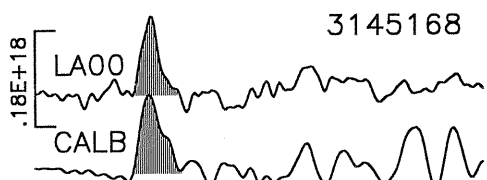
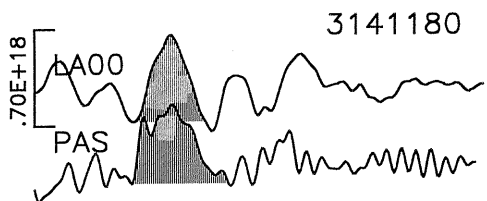
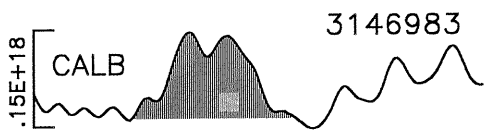
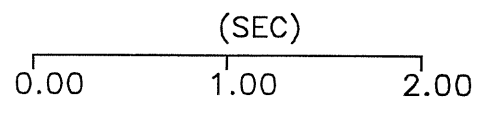
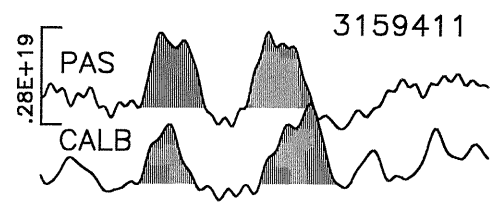
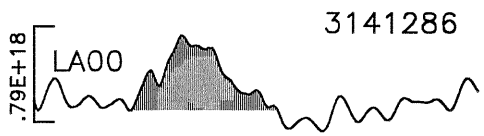
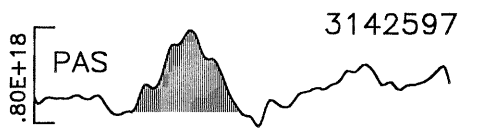
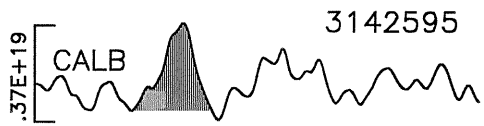
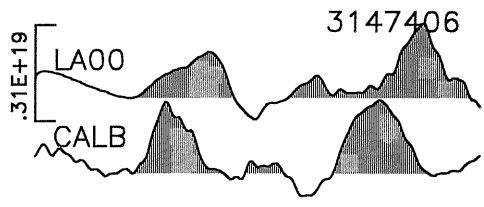
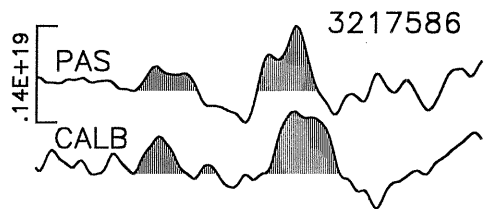
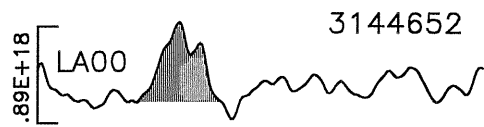
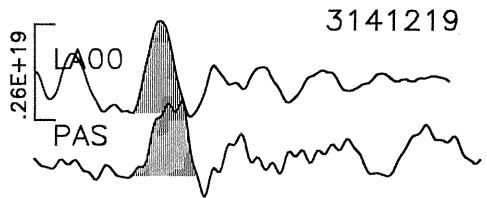
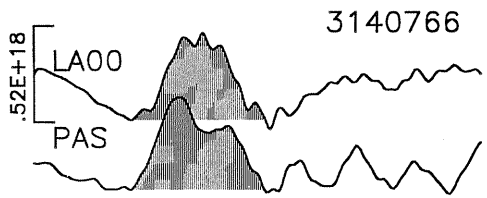
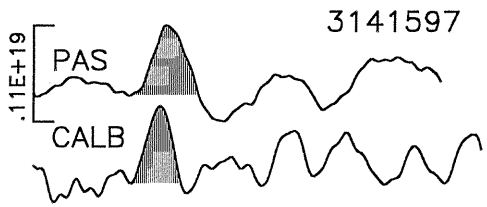
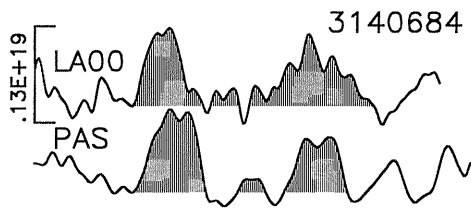


Figure 3. Source time functions of Northridge aftershocks used in this study derived from deconvolution of empirical Green functions. Shaded portion shows duration used for estimates of source dimension and static stress drop. Vertical scale (Nm/s) shows the amplitude such that the area of the shaded portion equals the seismic moment.





Source Parameters

Source Radius

Using the source time functions obtained from the empirical Green function deconvolutions, we estimate the pulse durations as shown in Figure 3 and summarized in Table 2. As a simple classification of pulse shapes, we also qualitatively identify each source time function as either a simple or complex waveform.

Deichmann [1999] discussed the problem of estimating pulse durations because of the ambiguity of picking the onset in the deconvolution. We can largely avoid this problem because the onsets are generally clear in the original data. Knowing the time of the onsets in the original data, we can calculate the start time of the deconvolved pulse. The onsets of the source time functions are not picked from the pulse of the deconvolved waveforms, but instead are calculated from the onsets of the original data.

Converting the pulse duration into an estimate of the source dimension (r) presents some uncertainty since any method is model dependent and also depends on the take-off angle (θ) from the fault plane, which is not always known. We use the relationship of *Boatwright* [1980] which assumes a circular rupture model,

$$r = \tau_{1/2} v / (1 - v/\alpha \sin \theta), \quad (1)$$

where $\tau_{1/2}$ is the rise time (assumed to be 0.5 time the total duration), α is the depth-dependent P-wave velocity (Table 3), and v is the rupture velocity assumed to be 0.75β . An average value for $\sin \theta$ of 0.64 is assumed for the take-off angle.

Static Stress Drop

The static stress drop is the difference between the final and starting stress levels on the fault and it is measured by determining the ratio of the slip to the fault dimension. In this study, the static stress drop ($\Delta\sigma_S$) is calculated using the formula of *Eshelby* [1957],

$$\Delta\sigma_S = 7/16 M_0/r^3 \quad (2)$$

where M_0 is the seismic moment. There is a difference in interpreting the static stress drops for simple and complex earthquakes, which can be seen if we compare two earthquakes that have equal moments and total durations. If one earthquake ruptured in a single event, while the other had several subevents, the actual static drops could be significantly different. For example, if the second earthquake was made up of two equal sized circular subevents, its static stress drop would be a factor of 4 higher than the single event. A good example of a complex earthquake is event 3159411 which has 2 clear subevents of about the same size. We calculate the static stress drops for all the earthquakes using the total duration of the source pulse. For complex earthquakes that have distinguishable subevents, we also estimate the static stress drop for the first subevent.

Dynamic Stress Drop

The dynamic stress drop is defined as the tectonic driving stress minus the dynamic frictional stress and is proportional to the slip velocity of the fault [Dahlen, 1974]. We follow Kanamori and Heaton [2000] and define the average dynamic stress drop ($\langle \Delta\sigma_d \rangle$) as the initial stress (σ_0) minus the average frictional stress ($\langle \sigma_f \rangle$):

$\langle \Delta\sigma_d \rangle = \sigma_0 - \langle \sigma_f \rangle$. The initial dynamic stress drop ($\Delta\sigma_d$) is simply the initial stress (σ_0) minus the initial frictional stress (σ_f): $\Delta\sigma_d = \sigma_0 - \sigma_f$. If the frictional stress is constant during rupture then the two dynamic stress drops are the same ($\Delta\sigma_d = \langle \Delta\sigma_d \rangle$), as shown in Figure 4(a).

Assuming a self-similar crack growth at the beginning of a rupture, Boatwright [1980] derived a formula for determining the dynamic stress drop ($\Delta\sigma_d$) from the initial slope of the far-field velocity pulse. We estimate $\Delta\sigma_d$ from the deconvolved source time functions (Figure 5) after differentiating once. We measure the initial slope (\dot{u}/t) for the first 0.05 to 0.1 sec, which corresponds to 15 to 30% of the duration. We then estimate $\Delta\sigma_d$ using the expression below derived by combining Boatwright's equations 5 and 40.

$$\Delta\sigma_d = M_0 (4\pi)^{-1} (1-\xi^2)^2 \nu^{-3} \bar{u}^{-1} \dot{u}/t \quad (3)$$

$(1-\xi^2)^2$ is a geometrical factor, which was assumed to have the average value of 0.75 and \bar{u} is the area of the source time function. Since the initial slope of the waveform is

measured, this estimate of dynamic stress drop is for the beginning part of the rupture. If the dynamic properties, such as friction, change with time, then the value of dynamic stress drop will also change, and $\Delta\sigma_d \neq \langle\Delta\sigma_d\rangle$.

Kanamori and Heaton [2000] obtained the following relation between radiated energy (E_S), static stress drop ($\Delta\sigma_S$) and $\langle\Delta\sigma_d\rangle$:

$$2 \mu E_S / M_0 = (2 \langle\Delta\sigma_d\rangle - \Delta\sigma_S). \quad (4)$$

where μ is the rigidity. We thus use our measurements of energy, moment and static stress drop to calculate the average dynamic stress drops. We use a depth-dependent rigidity, determined from the shear-wave velocity (Table 3).

Apparent Stress

The apparent stress, σ_e , was introduced by *Wyss and Brune* [1968]

$$\sigma_e = \mu E_S / M_0, \quad (5)$$

In this study, we calculate the apparent stress using the radiated energy and the depth-dependent rigidity. Although it is difficult to interpret the apparent stress as a physical stress level, the apparent stress is a measure of the ratio of the radiated energy to the moment. Replacing the moment by fault slip (D) and fault area (A), the apparent stress can be written as,

$$\sigma_e = (E_S/A) / D \quad (6)$$

In this expression, the apparent stress can be interpreted as the energy density, per unit fault area, per unit fault slip.

Radiated Energy

We estimate radiated energy (E_S) from the integral of the squared velocity records ($\int v^2 dt$) for the duration of the seismograms on three components, following *Kanamori*

et al. [1993]

$$E_S = 2.36 * 10^7 R^2 [R_0 q(R_0)/Rq(R)]^2 \int v^2 dt, \quad (7)$$

where E_S in Joules with hypocentral distance R in m and v in m/s. The distance-attenuation relationship $q(R) = 2.27 \times 10^3 R^{1.22} \exp(-5.3R)$, and $R_0 = 8$ km is the radius of the sphere used for the energy estimated. We use broadband velocity records at distances of 10 to 100 km. Typically 5-10 stations are used for each earthquake providing good azimuthal coverage and giving a fairly stable estimate. An important part of this process that improves the reliability of the radiated energy determination is the use of empirical station corrections that have been developed over the years of data recording. These empirical corrections for the individual station amplitudes considerably reduce the RMS scatter of estimates for a particular event [Kanamori et al., 1993].

Relation between Stress Drops and Energy

The relation between the various types of stress drops can be confusing, especially when considering the time and spatial dependence for rupture on a fault. In a simple fault model (Figure 4a), if the dynamic frictional stress is constant throughout the earthquake rupture (assuming uniform driving stress), the initial dynamic stress drop is equal to the average dynamic stress drop, and to the static stress drop. This is the classic *Orowan* [1960] model of stress release of an earthquake. The dynamic stress drop we calculate in this study from the initial portion of the waveform is closer to the initial dynamic stress drop, than the average dynamic stress drop. In this simple model, the radiated energy is directly proportional to the moment and so the apparent stress is constant for all size earthquakes, assuming constant static stress drop. The apparent stress is thus half of the average dynamic stress drop.

Summarizing the above statements,

$$\Delta\sigma_d \sim \Delta\sigma_s \sim \langle \Delta\sigma_d \rangle \sim 2\sigma_e \quad (8)$$

The physical mechanisms for fault slip in an earthquake are certainly more complicated than the simple *Orowan* model. For understanding the rupture process, the levels of

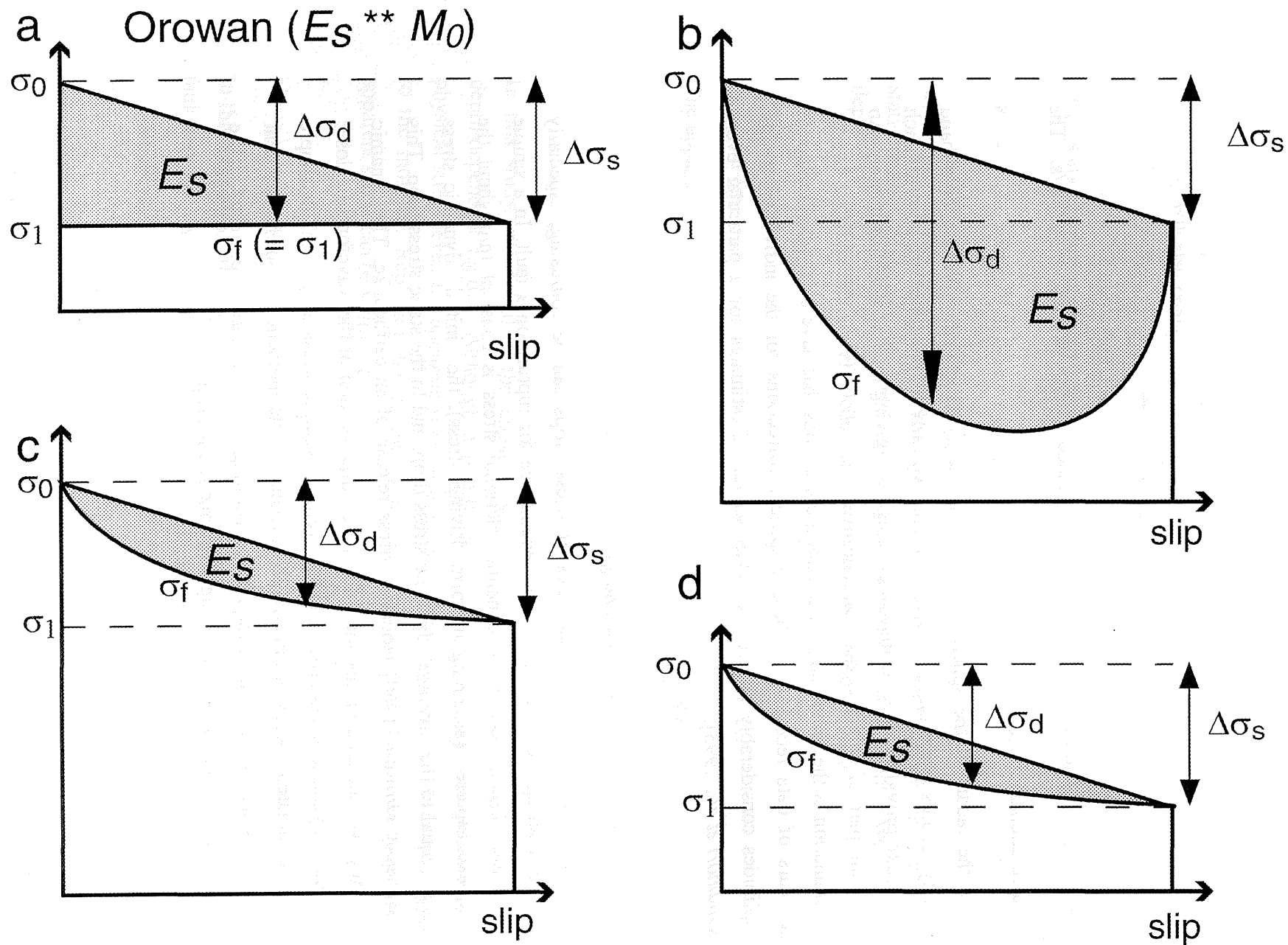


Figure 4. Range of schematic models illustrating the relationship between stress levels for an earthquake. (a) is the Orowan model, (b) is an undershoot or partial stress drop model, and (c) and (d) are overshoot models with the same stress drop, but different average stress level. The measurements of energy in this study are lower than the Orowan case, so suggest model (c) or (d) is most appropriate

frictional stress on the fault during the earthquake are especially important. Comparing these various estimates of stress drop in this study allows us to investigate the scaling of radiated energy as a function of earthquake size and make some inferences about the stress levels for these earthquakes in southern California

Results

The source parameters we obtain for the larger Northridge aftershocks are listed in Table 2 and shown in Figures 5-9. There is a large range in the static stress drops from a few tenths to several tens of MPa, but the values do not show a strong correlation with earthquake size (Figure 5) or event depth. Figure 6 shows the estimates of source radius as a function of moment, including data from other studies of larger southern California earthquakes that had reliable estimates of moment and fault size (Table 4). Similar to the results of *Kanamori and Anderson* [1975] and *Abercrombie and Leary* [1993], Figure 6 indicates that there is no systematic increase in static stress drop as a function of earthquake size.

When we combine our data from Northridge aftershocks with other data from recent southern California earthquakes (Table 4), Figure 7 shows that the ratio of E_S/M_0 gradually increases as a function of earthquake moment. For the smaller events (10^{15} to 10^{16} Nm) the ratio of energy to moment is 10^{-5} to 10^{-6} , while for the larger events ($>10^{16}$ Nm) the ratio increases to 10^{-5} to 10^{-4} . This study shows that there is a relative increase in the amount of radiated energy, as a function of earthquake moment, without a corresponding increase in the static stress drop. This observation is similar to the results for smaller earthquakes from *Abercrombie* [1995]. Overall the values of radiated energy are relatively small and indicate that the static and dynamic stress drops are roughly equivalent.

It is unlikely that the relatively small amounts of energy radiated by the earthquakes in this study (Figure 7), can be explained by attenuation effects. The values are about a factor of 10 smaller than for the larger earthquakes, which means a factor of $\sqrt{10}$ in actual amplitudes since the measurements are made from velocity-squared data. It seems unlikely that we are systematically underestimating the radiated energy of the smaller events by greater than a factor of three in the frequency range of 1 to 5 Hz. This is the frequency range that has been traditionally used for determining local magnitudes

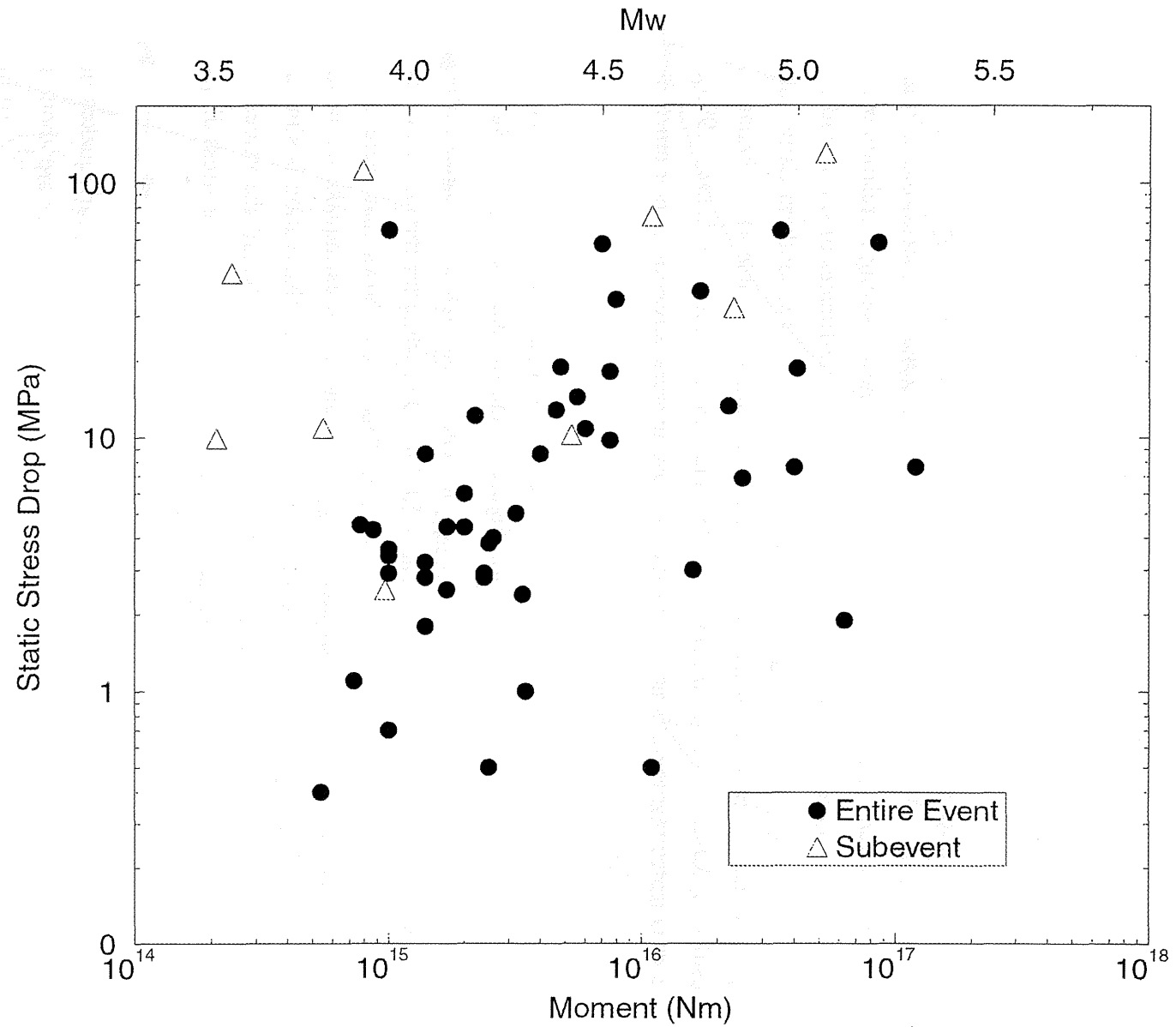


Figure 5. Static stress drops plotted as a function of moment for larger Northridge aftershocks (solid circles). The open circles are estimates of static stress drops and moments of clear subevents from complex source time functions.

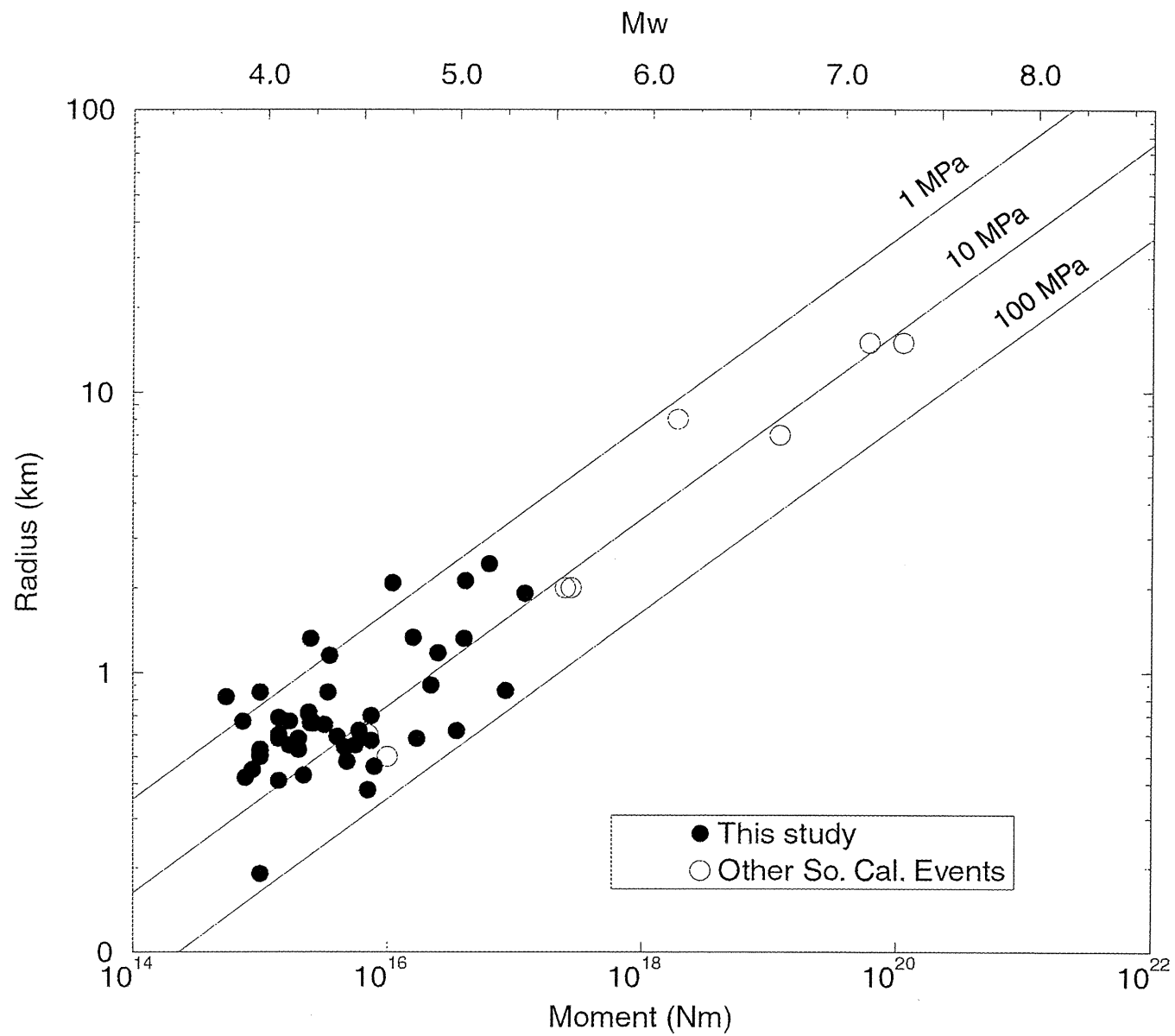


Figure 6. Source radius plotted as a function of moment for larger Northridge aftershocks (solid circles) and several other large Southern California earthquakes (open circles).

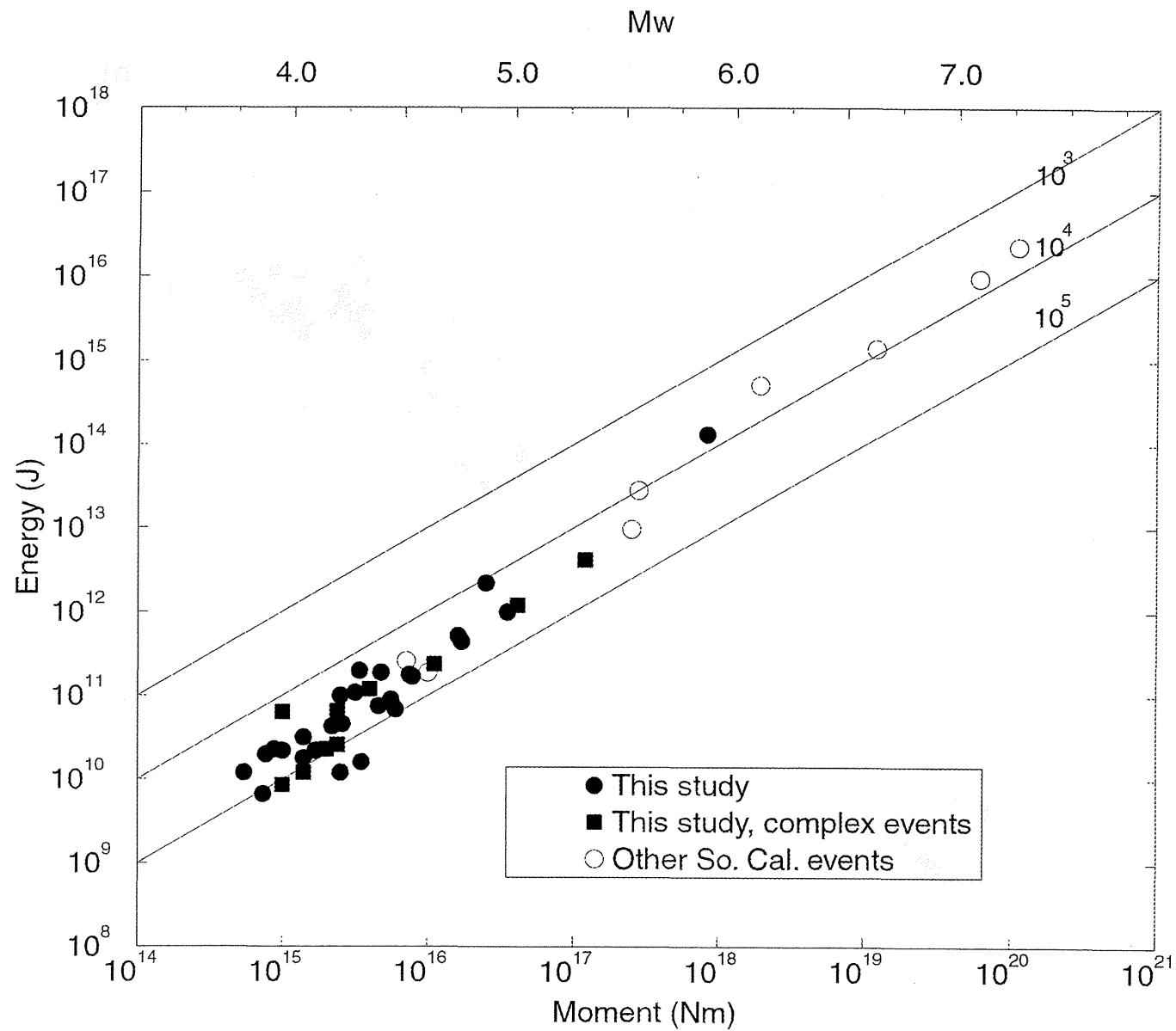


Figure 7. Radiated energy plotted as a function of moment for larger Northridge aftershocks analyzed in this study. Circles and squares represent "simple" and "complex" events, respectively. Data from other studies of Southern California earthquakes are also shown (open circles).

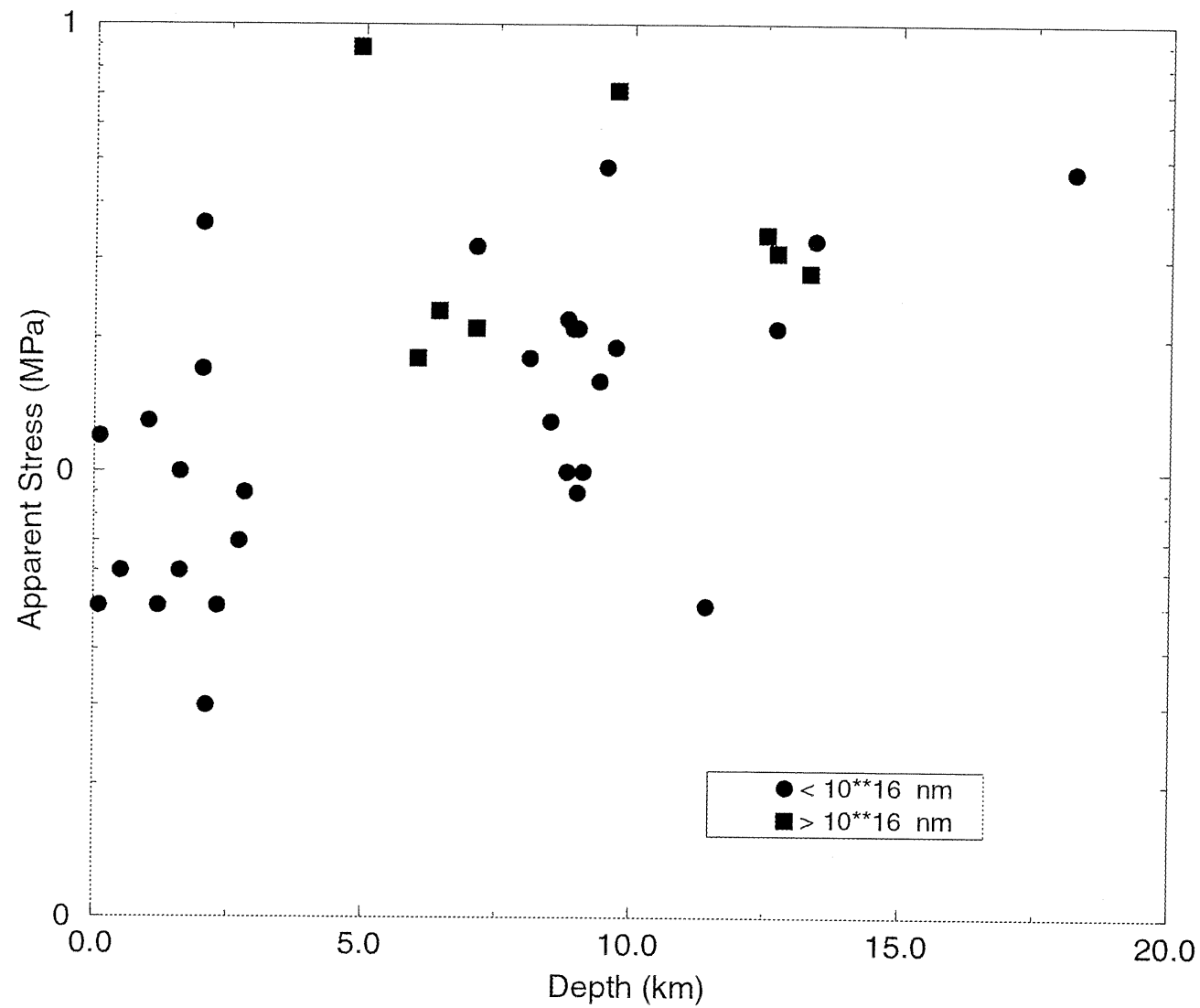


Figure 8. Apparent stress plotted as a function of source depth for larger Northridge aftershocks. The data are divided into two size classifications since there is a moment dependence of the radiated energy.

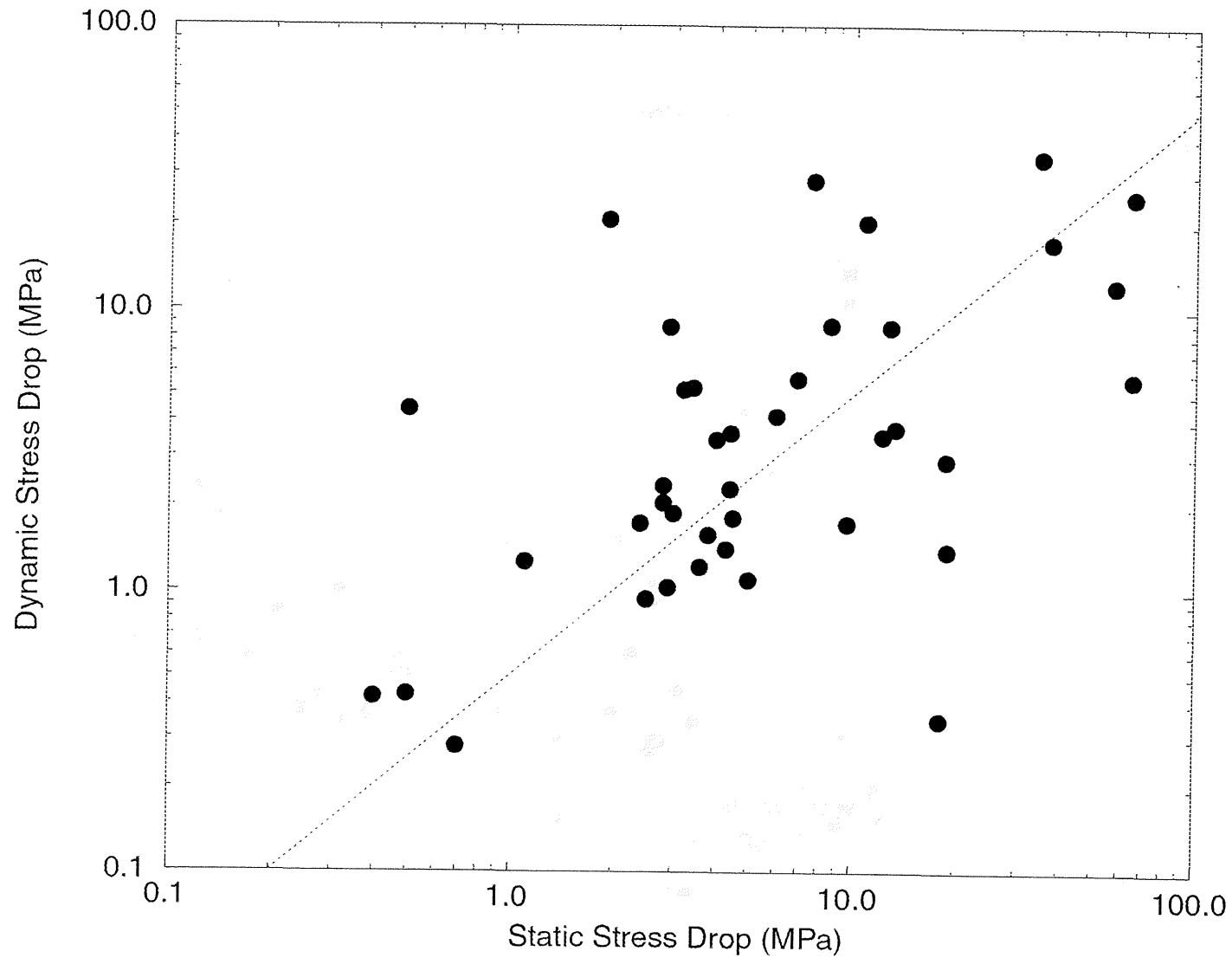


Figure 9. Comparison of dynamic stress drop estimated from measuring the slope of the velocity seismograms with dynamic stress drop derived from the radiated energy and static stress drop. The dotted line shows the relation of Equation 6 for $E_s / M_0 = 10^{-5}$

Table 2. Source parameters determined for Northridge aftershocks. Entries without ID numbers are source parameter estimates for the first subevent of the event listed above. s and c stand for simple and complex events, respectively.

ID	Moment (Nm)	Dur. (s)	E_s (J)		Static Stress (MPa)	App. Stress (MPa)	Dyn. Stress (MPa)	Simple/ Complex
3149105	1.40E+15	0.35	1.80E+10	0.60	2.8	0.10	2.06	s
3140898	1.00E+15	0.36	8.50E+09	0.51	3.4	0.05	5.28	c
	2.10E+14	0.15			9.9			
2150608	1.00E+15	0.38	6.40E+10	0.53	2.9	0.36	8.66	c
	5.50E+14	0.20			10.9			
3141062	1.00E+15	0.29		0.50	3.6		1.22	s
3159009	7.50E+15	0.33		0.57	18.1	0.35	0.91	
3155150	7.30E+14	0.48	6.70E+09	0.67	1.1	0.05	1.27	s
3141341	1.00E+15	0.45	2.20E+10	0.85	0.7	0.21	0.28	s
3141205	2.50E+15	0.71	1.20E+10	1.32	0.5	0.05	0.43	c
	9.70E+14	0.30			2.5			
3142087	1.40E+15	0.37		0.69	1.8			s
3140674	1.00E+15	0.11	0.00E+00	0.19	65.2		5.69	s
3144303	5.40E+14	0.48	1.20E+10	0.82	0.4	0.18	0.42	s
3150210	7.70E+14	0.25	2.00E+10	0.42	4.5	0.21	1.82	s
3141242	1.40E+15	0.41	1.20E+10	0.58	3.2	0.05	5.20	c
3172383	8.70E+14	0.26	2.30E+10	0.45	4.3	0.21	1.40	s
2138698	1.40E+15	0.30	3.20E+10	0.41	8.6	0.13	8.81	s
3140728	2.00E+15	0.38	2.30E+10	0.53	6.0	0.06	4.12	c
	2.40E+14	0.09			44.3			
3145171	1.70E+15	0.39	2.20E+10	0.67	2.5	0.10	0.94	s
3146983	3.50E+15	0.82	1.60E+10	1.15	1.0	0.03		s
3143541	2.00E+15	0.34		0.58	4.4	3.64	0.22	s
3141180	6.00E+15	0.44	6.90E+10	0.62	10.8	0.06	20.36	s
3145168	2.20E+15	0.25	4.30E+10	0.43	12.2	0.16	3.56	s
3143546	2.40E+15	0.42	2.60E+10	0.72	2.8	0.09	2.37	c
	7.90E+14	0.09			111.9			

ID	Moment (Nm)	Dur. (s)	E_s (J)		Static Stress (MPa)	App. Stress (MPa)	Dyn. Stress (MPa)	Simple/ Complex
3143547	2.40E+15	0.41	6.60E+10	0.71	2.9	0.22	1.03	c
3147259	1.70E+15	0.39	2.20E+10	0.55	4.4	0.07	2.31	s
3142081	2.60E+15	0.47	4.60E+10	0.66	4.0	0.10	3.46	s
3169078	4.60E+15	0.31	7.60E+10	0.54	12.8	0.13	8.7	c
3140691	4.00E+15	0.42	1.20E+11	0.59	8.6	0.17		c
3140870	5.60E+15	0.39	9.00E+10	0.55	14.4	0.09		s
3195727	3.40E+15	0.50	2.00E+11	0.85	2.4	0.48	1.74	s
3142198	4.80E+15	0.23	1.90E+11	0.48	18.9	0.47	1.4	s
3145627	7.50E+15	0.41	1.80E+11	0.70	9.7	0.19	1.74	s
3146628	3.20E+15	0.35	1.10E+11	0.65	5.0	0.33	1.10	c
3145150	2.50E+15	0.38	1.00E+11	0.66	3.8	0.32	1.58	s
3140678	7.90E+15	0.33	1.70E+11	0.46	34.8	0.12	34.65	s
3140853	7.00E+15	0.18		0.38	57.6		12.25	s
3140684	1.10E+16	1.21	2.40E+11	2.08	0.5	0.18	4.43	c
	5.30E+15	0.36			10.2			
3141597	1.70E+16	0.34	4.40E+11	0.58	37.5	0.21	17.4	s
3140766	1.60E+16	0.71	5.20E+11	1.33	3.0	0.31	1.89	s
3141219	3.50E+16	0.36	9.90E+11	0.62	65.1	0.23	25.3	s
3144652	2.20E+16	0.48		0.9	13.3		3.78	s
3217586	4.10E+16	1.09	1.20E+12	2.12	18.7	0.28	2.92	c
	1.10E+16	0.30			74.0			
3147406	6.30E+16	1.74		2.44	1.9		20.79	c
	2.30E+16	0.49			32.4			
3142595	8.50E+16	0.46		0.86	58.4		2.92	s
3142597	2.50E+16	0.68	2.20E+12	1.17	6.9	0.71	5.69	s
3141286	4.00E+16	0.77		1.32	7.6			s
3159411	1.20E+17	1.02	4.20E+12	1.91	7.6	0.34	28.63	c
	5.30E+16	0.30			130.7			
3141273	8.20E+17		1.30E+14				0.89	

in southern California, so the distance attenuation has been extensively studied [e.g. Jennings and Kanamori, 1983, Hutton and Boore, 1987].

Figure 7 also distinguishes between the simple and complex earthquakes in the Northridge aftershocks. One possible explanation for the larger ratio of radiated energy to moment for the larger earthquakes, is that the larger events tend to be more complex. Thus the large earthquakes have relatively more high-frequency content and generate more radiated energy. From our simple classification of source complexity, we see no indication of this.

Figure 8 shows the apparent stress (σ_e) as a function of earthquake depth. The data are divided into 2 subsets by moment since we show above that there is a dependence of the radiated energy on earthquake size. In Figure 8 there appears to be a trend of increasing apparent stress with earthquake depth, indicating that the deeper earthquakes are radiating relatively more energy than the shallow ones. One might obtain this apparent trend if the larger aftershocks systematically occurred at greater depth. This is not the case with our data set, which has a fairly even depth distribution for the range of aftershocks.

The values of dynamic stress drop and static stress drop are plotted in Figure 9 showing that there is a rough correspondence between the two stress drops. Also, it is significant that the two types of stress drop span about the same range of values indicating that the dynamic stress drops are not greatly larger than the static stress drops. The reason for the outlying points in Figure 9 can be seen in the waveforms. For example, the data point with the high (15 MPa) static stress drop and low (0.3 MPa) dynamic stress drop is earthquake 3159009. The waveform of this earthquake in Figure 3 is rather atypical and has a gradual onset that gives the relatively low dynamic stress drop for its static stress drop.

Discussion

Our study shows that there is a large range of static stress drops for the Northridge aftershocks (0.5 – 60 MPa). Some of this scatter may be due to problems in correctly estimating the source duration because of uncertainties such as deconvolution errors and rupture directivity. Since we are using only one to three stations for each event, there

is a limited azimuthal distribution, and we cannot taken into account rupture directivity which can significantly effect the observed source duration [e.g. *Mori, 1996, Venkataraman et al., 2000*]. Despite these large uncertainties, we do not think that they can account for the range of static stress drops that spans nearly two orders of magnitude.

The range of static and dynamic stress drops provides an informative comparison with the range of radiated energies. From the combined dataset in Figure 7 and using $\mu = 3 \times 10^3$ MPa. Using Equation (4), we see that $2\mu E_s / M_0$ (twice the apparent stress) has values in the range of 0.05 to 0.5 MPa. In our usage of Equation 4, the dynamic stress drop is the average dynamic stress drop, however, the quantity we measured from the initial slope is the initial dynamic stress drop, so we divide this number by 2.0 as an approximation for the average dynamic stress drop. The range of apparent stress is generally an order of magnitude smaller than our estimates of the dynamic ($\Delta\sigma_d$) and static ($\Delta\sigma_s$) stress drops. This implies that $(2\Delta\sigma_d - \Delta\sigma_s)$ is a relatively small number and the static and dynamic stress drops have values of the same order of magnitude. This is consistent with our independently calculated values of the dynamic and static stress drops, which have roughly similar values. The dotted line in Figure 9 shows the relation of Equation 6 for $E_s / M_0 = 10^{-5}$.

Figure 6 shows several simple models of earthquake stress release that we use for interpreting our results. We show the models as stress-displacement ($\sigma_f - \Delta u$) diagrams, as has been used by *Lachenbruch and Sass [1980]* and *Kikuchi and Fukao [1988]*. For an earthquake rupture, these diagrams show the stress levels on the vertical axis as a function of the fault displacement (slip times the surface area). The shaded region shows the amount of radiated energy. Model A is the classical *Orowan [1960]* model which shows a static stress drop from the initial stress to a final stress that is equal to the frictional stress. This model predicts constant scaling of earthquake moment with radiated energy for a constant stress drop. As mentioned above, recent observations indicate that this scaling does not hold over the large range of earthquake sizes. Also, from Equation 6, the absolute amount of observed radiated energy is not as large as predicted by this model.

Models B (abrupt locking) and C (overshoot) show two possibilities with varying

Table 3. 1-D velocity model derived from Mori et al., 1995.

Depth (km)	P Velocity (km/s)	S Velocity (km/s)
0	4.5	2.6
5	5.5	3.2
10		6.0 3.5
16		6.7 3.9

Table 4. Source parameters for southern California earthquakes determined in other studies.

Moment	Energy (Nm)	Radius (J)	(km)
Upland(1)(2) 2/28/90	2.5×10^{17}	9.7×10^{12}	2
Sierra Madre (2)(3) 6/28/91	2.8×10^{17}	2.8×10^{13}	2
Joshua Tree(2)(4) 4/23/92	1.9×10^{18}	5.1×10^{14}	8
Landers(6)(7) 6/28/92	1.1×10^{20}	2.3×10^{16}	15*
Northridge(5)(6)(7) 1/17/94	1.2×10^{19}	1.4×10^{15}	7
Northridge Aftershocks(8) 4/26/97	1.0×10^{16}	1.9×10^{11}	0.5
4/27/97	7.1×10^{15}	2.6×10^{11}	0.6
Hector Mine(6)(7) 10/16/99	6.0×10^{19}	9.3×10^{15}	15*

*For long strike-slip faults, this value is the fault width

(1) Dreger, 1993; (2) Kanamori et al., 1993; (3) Wald, 1992; (4) Hough and Dreger, 1995; (5) Wald et al., 1996; (6) Kanamori, personal comm.; (7) Harvard moment tensor catalog, Dziewonski et al., 1995.; (8) Venkatarama et al., 2000

dynamic frictional stress that can account for different amounts of radiated energy. Model B has a large drop of dynamic friction and generates large amounts of radiated energy with a large dynamic stress drop while Model C has much smaller radiated energy and smaller dynamic stress drop. The relatively low observations of E_S/M_0 in this study and the comparable estimates of dynamic and static stress drop indicate that Model C is preferable to Model B. If Model B correctly described earthquake ruptures, the ratio of E_S/M_0 should be more than an order of magnitude larger than what is observed and there should be much larger dynamic stress drops. From studies of source time functions of large earthquakes, *Kikuchi and Fukao* [1988] and *Kikuchi* [1992] also favor a model similar to Model C.

All of the seismological observations of stress in earthquakes are stress drops and do not tell us about the absolute level of stress. It is difficult, therefore, to distinguish between Models C and D which are the same except that the initial stress is 100 MPa for Model C and 10 MPa for Model D. Estimates of the heat generation during earthquakes suggest that it is difficult to sustain values of sliding friction that are over 10 MPa. If the sliding friction has such high values, large amounts of heat would be generated that may melt the fault [*Sibson*, 1973] or increase the fluid pressures that would reduce the effective normal stress [*Sibson*, 1973, *Lachenbruch*, 1980]. Either of these mechanisms would significantly reduce the dynamic friction. These arguments suggest that dynamic frictional stress in large earthquakes is low, indicating that the lower absolute stress levels of Model D are more reasonable than the high stress levels of Model C.

If the dynamic friction is low and the dynamic stress drop is comparable in size to the static stress drop, then earthquakes have nearly complete stress drops and the initial tectonic stress has values roughly equivalent to the static stress drops. This means the absolute value of the initial shear stress for these earthquakes ranges from a few to a few tens of MPa, although there is a large range of scatter. These results indicate that earthquakes in southern California are generally driven by crustal stresses in the range of a few MPa to a few tens of MPa (tens to hundreds of bars) and not in the 100 MPa (kilobar) range. This supports the idea that California faults are generally low-strength structures, [e.g., *Brune et al.*, 1969; *Sass and Lachenbruch*, 1980; *Zoback et al.*, 1987] rather than high-strength [e.g. *McGarr and Gay*, 1978, *Hickman*, 1991]. Occasional earthquakes do occur with very high stress drops, such as a few of the events in this study (e.g. 3140674, 3140853) and other earthquakes like the M4.9

Pasadena earthquake which have stress drops in the 100 MPa range [Kanamori, et al., 1990]. This indicates that locally there can be higher levels of stress.

Another significant result of this study is confirming the relative increase of radiated energy as a function of earthquake size, without a corresponding increase in the static stress drop, as suggested by *Abercrombie* [1995]. The dynamic stress drops also appear to be higher for the large earthquakes. The increase of E_S / M_0 and higher average dynamic stress drop for larger earthquakes suggest that there may be a gradual change in the rupture process, as a function of earthquake size. One explanation is that all earthquakes have the same level of dynamic frictional stress and the same static stress drop, but larger earthquakes have higher initial stress. An alternative explanation is that the average frictional stress is lower for larger earthquakes, for example, if it decreases with increasing slip. This could be related to the consequences of heat generation on the fault which can lower dynamic friction, due to fault melting or fluid pressurization [Kanamori and Heaton, 2000]. The size of the earthquake may affect the extent of the thermally controlled dynamic friction. Larger earthquakes would generate more heat per fault area causing lower dynamic friction, resulting in higher levels of radiated energy.

In contrast to our observations which show that larger earthquakes radiate relatively more energy than smaller ones, *McGarr* [1999] proposed a constant upper bound to the apparent stress over a large range of earthquake magnitudes. *McGarr* argues for a constant maximum seismic efficiency for all events from laboratory scales to large earthquakes. The principal difference between the two approaches is probably that we are interpreting the average values of a parameter, while *McGarr* considered the maximum.

The increase of radiated energy with source depth may also be explained in terms of the friction levels on the fault. At greater depths there are higher initial shear stress levels and the amount of heat generation could cause lower dynamic friction than for shallower earthquakes. This would result in the larger radiated energy observed for deeper earthquakes. This model might also explain the observations that *b*-value and foreshock occurrence decrease with depth in the crust [Abercrombie and Mori, 1996, Mori and Abercrombie, 1997]. If the dynamic friction is lower for deeper earthquakes, then they could be harder to stop. A rupture initiation at depth, therefore, would be more

likely to grow into a larger earthquake than a rupture initiation at shallow depth, as suggested by *Abercrombie and Mori* [1996] and *Mori and Abercrombie* [1997].

Conclusions

1. For the large aftershocks of the 1994 Northridge earthquake, there is a large range of static stress drops from a few tenths to several tens of MPa.. The values do not correlate strongly with earthquake size or depth.
2. We observe a relative increase of radiated energy as a function of earthquake size.

The ratio of E_S/M_0 is around 10^{-5} for smaller (10^{15} Nm) earthquakes and around 10^{-4} for larger ($>10^{16}$ Nm) earthquakes. This is not due to an increase in static stress drop and may be related to frictional properties on the fault. The effect of heat generation and consequent melting of the fault or fluid pressurization could cause larger earthquakes radiate more energy.

3. There is a relative increase of radiated energy as a function of source depth which may indicate that deeper earthquakes at higher normal stress experience lower dynamic friction and more complete stress drops.
4. The radiated energies are relative low compared to the static stress drops; the static and dynamic drops have values of the same order of magnitude. If the dynamic frictional stress is low, this indicates that the earthquakes have nearly total stress drops and the absolute level of the initial stress is roughly equivalent to the static stress drop. If this is correct, the crustal shear stresses responsible for the earthquakes are on the order of several to several tens of MPa (10 s to 100 s bars), and not on the order of 100 MPa (kilobar).

Acknowledgments: Data used in this study were provided by the SCEC Data Center.

J. Mori acknowledges support from the USGS during the early part of this study.

References

- Abercrombie, R. E., Earthquake source scaling relationships from 1 to 5 M_L using seismograms recorded at 2.5-km depth, *J. Geophys. Res.*, 100, 24015-24036, 1995.

- Abercrombie, R. E. and J. Mori, Characteristics of foreshock occurrence to large earthquakes in the western USA, *Nature*, 381, 303-307, 1996.
- Abercrombie R. and P. Leary, Source parameters of small earthquakes recorded at 2.5 km depth, Cajon Pass, Southern California: Implications for earthquake scaling, *Geophys. Res. Lett.*, 20, 1511-1514, 1993.
- Aki, K., Scaling Law of seismic spectrum, *J. Geophys. Res.*, 65, 729-740, 1967.
- Barton, C.A. and M.D. Zoback, Stress perturbations associated with active faults penetrated by boreholes: Possible evidence for near-complete stress drop and a new technique for stress magnitude measurement, *J. Geophys. Res.*, 99, 9373-9390.
- Boatwright, J., Seismic estimates of stress release, *J. Geophys. Res.*, 89, 6961-6968, 1984.
- Brune, J. N., Tectonic stress and the spectra of seismic shear waves from earthquakes, *J. Geophys. Res.* 75, 4997-5009, 1970.
- Brune, J.N., T.L. Henyey and R.F. Roy, Heat flow, stress, and rate of slip along the San Andreas fault, California, *J. Geophys. Res.*, 74, 3821-3827, 1969.
- Cohn, S.N., T-L, Hong, D.V. Helmberger, The Oroville earthquakes: a study of source characteristics and site effects, *J. Geophys. Res.*, 87, 4585-4594, 1982.
- CURee, Northridge Research Summary, 1998.
- Dahlen, F.A., On the ratio of P-wave to S-wave corner frequencies for shallow earthquake sources, *Bull. Seismol. Soc. Am.*, 64, 1159-1180., 1974.
- Deichmann, N, Empirical Green's functions: Comparison between pulse width measurements and deconvolution by spectral division, *Bull. Seismol. Soc. Am.*, 89, 178-189, 1999.
- Dreger, D., Modeling earthquakes with local and regional broadband data, California Inst. of Technology thesis, 1993.
- Dreger, D., The large aftershocks of the Northridge Earthquake and their relationship to mainshock slip and fault-zone complexity, *Bull. Seismol. Soc. Am.*, 87, 1259-1266, 1997.
- Dziewonski et al., CMT reference.
- Eshelby, J.D., The determination of the elastic field of an ellipsoidal inclusion and related problems, *Proc. R. Soc. London A*, 241, 376-396, 1957.
- Hickman, S., Stress in the lithosphere and the strength of active faults, U.S. Nat. Rep. Int. Union Geod. Geophys. 1987-1990, *Rev. Geophys.*, 29, 759-775, 1991.
- Hough, S. and D. Dreger, Source parameters of the 23 April 1992 M6.1 Joshua Tree, California earthquake and its aftershocks: Empirical Greens function analysis of

- GEOS and TERRAScope data, *Bull. Seismol. Soc. Am.*, 85, 1576-1590, 1995.
- Hutton, L.K. and D.M. Boore, The M_L scale in Southern California, *Bull. Seismol. Soc. Am.*, 77, 2074-2094, 1987.
- Jennings, P. and H. Kanamori, Effect of distance on local magnitudes found from strong-motion records, including records from the 1979 Imperial Valley, California, earthquake, *Bull. Seismol. Soc. Am.*, 73, 265-280, 1983.
- Kanamori, TERRAScope and CUBE Project at Caltech, EOS Transactions, American Geophysical Union, 72, 564-565, 1991.
- Kanamori H., and D.L. Anderson, Theoretical basis of some empirical relations in seismology, *Bull. Seismol. Soc. Am.*, 65, 1023-1095, 1975.
- Kanamori and Heaton, Microscopic and macroscopic physics of earthquakes, 2000
- Kanamori, H., J. Mori, E. Hauksson, T.H. Heaton, L.K. Hutton, L.M. Jones, Determination of earthquake energy release and M_L using Terrascope, *Bull. Seismol. Soc. Am.*, 83, 330-346, 1993.
- Kanamori, H., J. Mori, T.H. Heaton, The 3 December 1988, Pasadena earthquake ($M_L=4.9$) recorded with the very broadband system in Pasadena, *Bull. Seismol. Soc. Am.*, 80, 483-487, 1990.
- Kikuchi, M., Strain drop and apparent strain for large earthquakes, *Tectonophysics*, 211, 107-113, 1992.
- Kikuchi M. and Y. Fukao, Seismic wave energy inferred from long-period body waves inversion, *Bull. Seismol. Soc. Am.*, 78, 1707-1724, 1988.
- McGarr, A., On relating apparent stress to the stress causing earthquake fault slip, *J. Geophys. Res.*, 104, 3003-3012, 1999.
- Lachenbruch, A.H., Frictional heating, fluid pressure, and the resistance to fault motion, *J. Geophys. Res.*, 85, 6097-6112, 1980.
- Lachenbruch, A.H. and J.H. Sass, Heat flow and energetics of the San Andreas fault zone, *J. Geophys. Res.*, 85, 6185-6222, 1980.
- Mayeda, K. and W.R. Walter, Moment, energy, stress drop, and source spectra of western United States earthquakes from regional coda envelopes, *J. Geophys. Res.*, 101, 11195-11208, 1996.
- McGarr, A., On relating apparent stress to the stress causing earthquake fault slip, *J. Geophys. Res.*, 104, 3003-3012, 1999.
- McGarr, A. and N.C. Gay, State of stress in the earth's crust, *Ann. Rev. Earth Planet. Sci.*, 6, 405-436, 1978.

- Mori, J., Rupture directivity and slip distribution of the M4.3 Foreshock to the 1992 Joshua Tree earthquake, southern California, *Bull. Seismol. Soc. Am.*, 86, 805-810, 1996.
- Mori, J. and R. E. Abercrombie, Depth dependence of earthquake frequency magnitude distributions in California: Implications for rupture initiation, *J. Geophys. Res.*, 102, 15, 081-15,090, 1997.
- Mori, J. and A. Frankel, Source parameters for small events associated with the 1986 North Palm Springs, California, earthquake determined using empirical Green Functions, *Bull. Seismol. Soc. Am.*, 80, 278-295, 1990.
- Mori, J., D.J. Wald, and R.L. Wesson, Overlapping faults planes of the 1971 San Fernando and 1994 Northridge, California earthquakes, *Geophys. Res. Lett.*, 22, 1033-1036, 1995.
- Mueller, C.S., Source pulse enhancement by deconvolution of an empirical Green's function, *Geophys. Res. Lett.*, 22, 33-36, 1985.
- Orowan, E., Mechanism of seismic faulting, *Geol. Soc. Am., Mem.*, 79, 323-345, 1960.
- Sibson, R.H., Interactions between temperature and pore-fluid pressure during earthquake faulting, a mechanism for partial or total stress relief. *Nature Phys. Sci.*, 243, 66-68, 1973.
- Sibson, R. H., Geological evidence for fluid involvement in the rupture process of crustal earthquakes, *Proceedings of Workshop LXIII The mechanical involvement of fluids in faulting*, ed. S. Hickman, R. Sibson, R. Bruhn, U.S. Geol. Surv. Open-File Report 94-228, 31-38, 1994.
- Thio H.K. and H. Kanamori, Source complexity of the 1994 Northridge earthquake and its relation to aftershock mechanisms, *Bull. Seismol. Soc. Am.*, 86, S84-S92, 1996.
- U.S. Geological Survey, Northridge 94: A Damaging Urban Earthquake, U.S. Geol. Surv. Open-File Report, 96-263, 1996.
- Venkatarama, Anupama, J. Mori, H. Kanamori, and L. Zhu, Fine structure of the rupture zone of the April 26 and 27, 1997 Northridge aftershocks, *J. Geophys. Res.*, 19085-19093, 2000.
- Wald, D., Strong motion and broadband teleseismic analysis of the 1991 Sierra Madre, California, earthquake, *J. Geophys. Res.*, 97, 11,033-11,046, 1992.
- Wald, D., T.H. Heaton, and K.W. Hudnut, The slip history of the 1994 Northridge, California earthquake determined from strong-motion, teleseismic, GPS, and leveling data, *Bull. Seismol. Soc. Am.*, 86, 549-570, 1996.

Wyss, M. and J.N. Brune, Seismic moment, stress, and source dimensions for earthquakes in the California-Nevada region, *J. Geophys. Res.*, 73, 4681-4694, 1968.

Zoback, M.D., M.L. Zoback, V.S. Mount, J. Suppe, J.P. Eaton, J.H. Healy, D. Oppenheimer, P. Reasenber, L. Jones, C.B. Raleigh, I.G. Wong, O. Scotti and C. Wentworth, New evidence on the state of stress of the San Andreas fault system, *Science*, 238, 1105-1111, 1987.

List of Paper Presented at Conferences

2000 Western Pacific Geophysics Meeting

Slip Velocity Estimates of the 1999 Chi-Chi, Taiwan, Earthquake: New
Observations of Fault Dynamics

Mori, J, Ma, K-F

2000 American Geophysical Union Fall Meeting

Estimates of Radiated Energy for Moderate Shallow Earthquakes in Japan

Kobayashi, H, Mori, J, Sato, K

2001 Japan Earth and Planetary Sciences Joint Meeting

Scaling of Radiated Energy for moderate earthquakes in Japan.

Kobayashi, H., J. Mori

2001 Japan Seismological Society Meeting

1999年集集台湾地震に見られたアスペリティの破壊過程の調査

Searching for Physical Mechanisms to Explain the Large Asperity of the 1999
Chichi, Taiwan Earthquake

James Mori 伊藤久男, 安藤雅孝 馬國鳳 Mark Zoback

2001 American Geophysical Union Fall Meeting

Difference in Rupture Process Between Shallow and Deep Earthquakes
Estimated From Radiated Energy of Small Events

Kim, A, J. Mori